Distributed Intelligence for Online Situational Awareness and Resilience in Power Grids

by Shiyuan Wang

B.S. in Mechanical Engineering, May 2012, University of Science and Technology Beijing
M.S. in Electrical Engineering, May 2014, The George Washington University

A Dissertation submitted to

The Faculty of
The School of Engineering and Applied Science
of The George Washington University
in partial satisfaction of the requirements
for the degree of Doctor of Philosophy

August 31, 2020

Dissertation directed by

Payman Dehghanian
Assistant Professor of Electrical and Computer Engineering

The School of Engineering and Applied Science of The George Washington University certifies that Shiyuan Wang has passed the Final Examination for the degree of Doctor of Philosophy as of Aug 11, 2020. This is the final and approved form of the dissertation.

Distributed Intelligence for Online Situational Awareness and Resilience in Power Grids

Shiyuan Wang

Dissertation Research Committee:

Payman Dehghanian, Assistant Professor of Electrical and Computer Engineering, Dissertation Director

Robert Harrington, Professor of Electrical and Computer Engineering, Committee Member

Miloš Doroslovački, Associate Professor of Electrical and Computer Engineering, Committee Member

Shahrokh Ahmadi, Teaching Professor of Electrical and Computer Engineering, Committee Member

Mohammed Shamma, Adjunct Professor of Electrical and Computer Engineering, Committee Member

Acknowledgments

First and foremost, I would like to express my sincere gratitude to my advisor Prof. Payman Dehghanian for the tireless support of my Ph.D. study and research in electric power and energy engineering, for his patience, motivation, enthusiasm and immense knowledge. His insight and wisdom have made remarkable contributions to our publications and writing of this dissertation. I could not have imagined having a better advisor and mentor for my Ph.D study.

Besides my advisor, I would like to thank the rest of my thesis committee; Prof. Robert Harrington, Prof. Miloš Doroslovački, Prof. Shahrokh Ahmadi and Prof. Mohammed Shamma for their encouragement, great efforts and valuable feedback on my research for their encouragement, insightful comments, and hard questions.

I would also like to thank Ms. Sandy Harrington at Municipal Electric Power Association of Virginia for the support in my research project. My sincere thanks also go to Prof. Amir Etemadi, who provided me with the precious suggestions on my work. I also want to thank my colleagues and friends in the GW Smart Grid Laboratory. All our discussions about study and life are and will be the most precious memories for me.

Very special thanks to my beloved wife Rong for her support and assistance in every step of my dissertation work, and I would like to thank my daughter Katherine; her presence gave me the unlimited happiness and pleasure when I was writing my dissertation.

Last but not the least, I would like to thank my parents, my brother for supporting me spiritually throughout writing this dissertation and my life in general. I could not have achieved my goal without their love and sacrifices. They are always my strong backing.

Abstract

Distributed Intelligence for Online Situational Awareness and Resilience in Power Grids

Electric power grids constantly confront potential fast- and slow-dynamic disruptions ranging from unpredictable faults, weather-driven disasters, malicious cybersecurity attacks, load variations, among others. With the growing demand to ensure electricity with higher quality to the end-use customers and mission-critical systems and services, enhancing the resilience and operational endurance of the power delivery infrastructure against disruptive events and reducing and mitigating such threatening risks is urgently needed. This calls for fundamental advancements of new, fast, and efficient analytical frameworks for online situational awareness in power grids that can accurately measure and effectively monitor, detect, adapt and respond to a wide range of threats.

We first propose an inclusive next-generation smart sensor technology embedded with novel and sophisticated data-driven analytics for online surveillance and situational awareness in power grids. The proposed analytics take the electrical signals as the input and unlock the full potential in advanced signal processing and machine learning for real-time pattern recognition, event detection and classification. A robust measurement mechanism is housed within the proposed sensor technology that will be triggered following a detected event and guides on the adaptive selection of the best-fit and most accurate synchrophasor estimation algorithms at all times. Embedding such analytics within the sensors and closer to where the data is generated, the proposed distributed intelligence mechanism mitigates the potential risks to communication failures and latencies, as

well as malicious cyber threats, which would otherwise compromise the trustworthiness of the end-use applications in distant control centers. Our experiments demonstrate that the introduced sensor technology achieves a promising event detection and classification accuracy with improved quality of measurements, collectively resulting in enhanced online situational awareness in power grids. Also, the performance of the proposed smart sensor analytic is tested and verified in several event detection applications in the power grid.

Table of Contents

List of Figures

List of Tables

Chapter 1: INTRODUCTION

1.1 Background

New North American Electricity Reliability Corporation (NERC) power system planning performance standard TPL-0014/0040a enforced in 2016 states that "*studies shall be performed to assess the impact of the extreme events* [4]." The electricity grid is constantly exposed to potential hazards ranging from weather-driven natural disasters to malicious cybersecurity attacks [5]. Due to numerous factors such as rapid deployment of intermittent renewable generation, growing demand to ensure higher quality electricity to end customers, and intensified public focus and regulatory oversights, safeguarding the nation's electric power grid and ensuring a continuous, reliable, and affordable supply of energy are among the top priorities for the electric power industry. Hence, resilience of the electricity grid and its capacity to withstand unexpected extreme events has become more and more critical for peoples' well-being and every aspect of our economy [6–8].

To improve the resilience of the electricity grid, situational awareness of the power grid to support decision making under uncertainty and quantify the corresponding impacts become significantly crucial. The fundamental definition of the term "situational awareness" in the context of power grid operation is "*understanding the current environment and being able to accurately anticipate future problems to enable effective actions*" [9]. Due to the increasing size and operational complexity of modern power systems, system operators often have difficulties forming a complete and accurate picture of the state of (the part of) the system for which they are responsible. These difficulties may prevent them from achieving the level of situational

awareness that is needed to make the right decisions and respond effectively to an incident. Inadequate situational awareness has indeed been identified as one contributing factor in several recent large electrical disturbances and black outs worldwide.

With the rapid proliferation of distributed energy resources in the power grid, more observability and control systems will be needed to accurately monitor the more-than–ever sophisticated cyber-physical power grid. In 1988, the invention of the Phasor Measurement Units (PMU) by Dr. Arun G. Phadke and Dr. James S. Thorp at Virginia Tech transformed the situational awareness of the power grid into a new level. With the nowadays widespread deployment of synchrophasor technology in modern power grids, system monitoring and control settings have been revolutionized into a new era with high-resolution measurements [10–15]. Synchrophasor measurements, captured across the network via PMUs, have transformed many applications, e.g., power system model validation, state-estimation, dynamic stability, online monitoring, protection and control functions, and post-event analysis [16, 17]. In Figure. 1.1, a block diagram of a typical PMU is demonstrated; this device measures the electrical waveforms in an electric power grid where a common time source, usually from GPS, is used for synchronization. The measurements from PMUs across the power network are gathered at the control center through communication channels.

With the growing demand to ensure electricity with higher quality to the end-use customers and mission-critical systems and services, enhancing the power delivery infrastructure resilience and operational endurance against disruptive events while reducing and mitigating such threatening risks is urgently needed. This calls for fundamental advancements of new, fast, and efficient analytical frameworks for online situational awareness

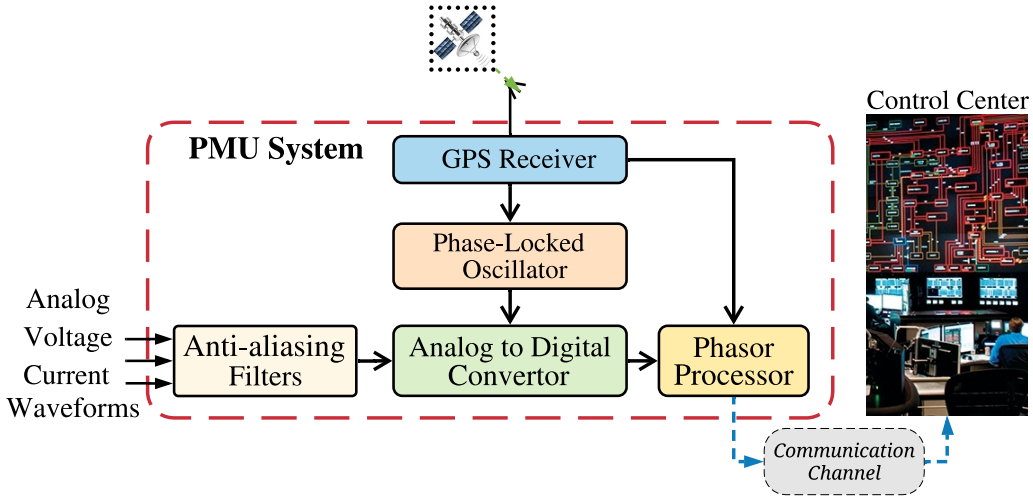

Figure 1.1: Block diagram of a typical phasor measurement unit (PMU).

in power grids that can accurately measure and effectively monitor, detect, adapt and respond to a wide range of threats.

This rest of this chapter is organized as follows. Section 1.2 offers an introduction to PMUs and details of this sensor technology. Problems and challenges with the existing PMUs are presented in Section 1.3. Aiming at effectively dealing with the challenges and issues in the existing technologies and state-of-the-art solutions from the literature, Section 1.4 lists the research objectives of this dissertation. At last, the dissertation outline is presented in Section 1.5.

1.2 An Introduction to Synchrophasor Technology

The PMU network is built to be a data gathering system in power grids and significantly improves the monitoring capabilities of the grid and analyzing power system dynamics. As PMUs are installed throughout the electricity system, the Phasor Data Concentrators (PDCs) are used to collect the information and a Supervisory Control And Data Acquisition (SCADA) system at the central control facility utilizes the data for protection, control, and

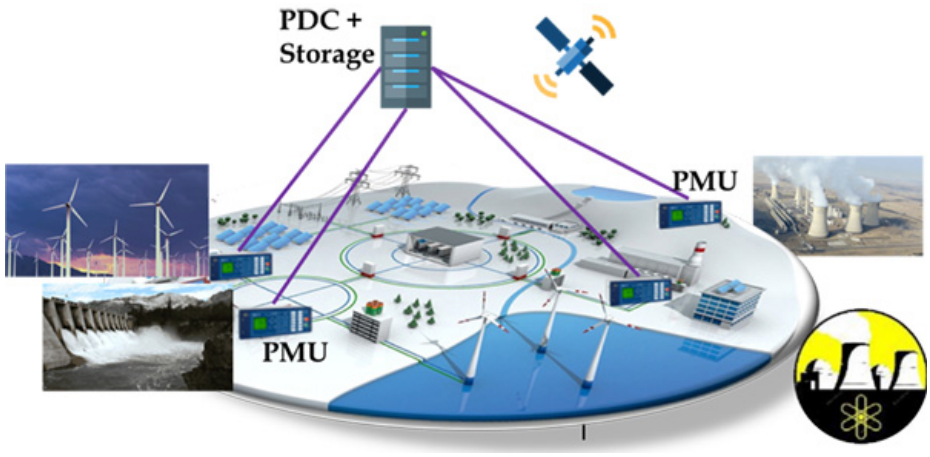

Figure 1.2: PMU System Architecture in Power Systems [1]

operation of the power grid. The existing monitoring and control paradigms in power systems are primarily based on centralized architectures. As it is demonstrated in Figure 1.2, the sensing landscape consists of locally distributed PMU sensors, the measurements from which are collected in distant control centers for monitoring and control decision making [18]. Additionally, the trustworthiness of the control center functions heavily relies on accurate synchrophasor measurements from PMU sensors; these outputs are obtained from synchrophasor estimation algorithms (SEAs) embedded within the PMUs which are primarily driven by mathematical approximations. For instance, Discrete Fourier Transform, Kalman Filtering, Adaptive Filtering, Newton approximations, Phase-Locked Loops, and many other variations exist [19–24]. IEEE standard C37.118.1-2011 [25] has defined the expected outputs—i.e., magnitude, phase angle, frequency, and rate of change of frequency (ROCOF)—and their corresponding desirable accuracy. This current practice relies heavily on reliable and secure communication gateways: if the communication channels are lost (due to failures, natural disasters, or man-made cyber-attacks) or have delays (due to network congestion, poor channel quality, etc.), the control center

analytics' accuracy and application trustworthiness will be compromised or will be attributed a latency [26, 27]. In most cases, and irrespective of the focused end-use application utilizing the measurements, marketplace PMUs are typically furnished with "only one" SEA tool, each unleashing distinctive advantages and limitations, and are solely accurate for one or a few certain applications [28, 29]. This is because the waveforms fed into such sensors have typically variant behaviors (e.g., during faults, unbalanced loads, voltage surge or sag, harmonics, etc) [30, 31]. Also, different applications may enforce different response time and accuracy requirements. Some research efforts proposed a single PMU equipped with only one sophisticated SEA, which is deemed to respond to variant conditions in the grid [32, 33].

From a practical perspective, large deployment of PMU sensors brings about a few concerns: (i) the massive PMU data in wide-area power systems is hard to process and store in real time, (ii) communication availability and reliability is hard to maintain for wide area measurement systems (WAMS), (iii) power system monitoring requires high-resolution data, which could be compromised by communication latencies. Approaches for PMU data dimensionality reduction have been introduced in [34–36] to mitigate the high computational burden of the control center applications in processing large volumes of data. Also, different techniques for PMU data compression are reported in [37–40]. Also, to deal with the data loss or delays in PMU WAMS, researchers explored different methods to evaluate and quantify the sensing and monitoring accuracy performance under scenarios with missing PMU data [41–43].

1.3 Problem Statement

The electricity grid is constantly exposed, and yet vulnerable, to a wide range of threats, some foreseeable and some unpredictable random in nature. PMUs should be able to provide accurate and timely measurements under various grid operating conditions. However, it has been demonstrated in the literature that:

- A pre-installed synchrophasor estimation algorithm (SEA) inside the PMU sensors needs to be chosen carefully or tuned at times to meet the performance requirements of the end-use applications employing the measurements [32, 33].
- While exposed to different operating conditions in the power grid, a particular SEA may best fit one certain type of event and not all.
- PMUs do not have the capability to provide event detection functionalities based on the phasor measurements or input electrical waveforms.
- An SEA can be tuned with distinct parameters, making it extremely difficult to achieve the desired accuracy at all times.

To archive adequate grid monitoring performance, the PMU synchrophasor measurement quality should always meet the standard requirements; however, laboratory tests and field observations have revealed the inefficiency of the existing PMU measurements. Even if "one-size-fits-all" SEA is installed into one PMU to capture both static and dynamic features and peculiarities in power systems, the measurements are very hard to meet the standard requirements when facing different operating states [44, 45]. To meet the growing demand for high-speed, low-latency, and yet absolutely accurate

measurements, a more efficient mechanism which adaptively, and in an automated manner, selects the right SEA at the right time is desired.

In all, to address various multi-dimensional challenges in the power grid, solutions that can help in detecting and monitoring variant types of events or unfolding threats in or near real-time, meanwhile, enhance situational awareness, are of significant importance and in urgent demand.

1.4 Research Objectives

This dissertation focuses on developing a next-generation smart sensor solution in power grids that enables (1) a paradigm shift from sensing-only to sensing-and-actuating mechanisms—i.e., distributed intelligence—that can achieve online event detection and classification, and (2) high-fidelity measurements in power grids under various prevailing conditions at nearly all time. The latter is achieved through an SEA selection scheme embedded within the smart sensor that adaptively selects the most promising algorithms installed within the smart sensor.

The proposed smart sensor solution aims to shift the centralized sensing and monitoring paradigm into a distributed system using an edge computing technology, in which

- Each PMU pre-processes the synchrophasor data, gathers the information at the location where power waveforms are obtained and then reports the detected event to the distant and local control centers.

- Electrical waveforms are directly processed using the computing capability at the point where the waveforms is captured; the raw PMU input signals, e.g., currents and/or voltage, are sampled in real time and contain very important information on the events in the grid. In

such a way, the real time processing requirement of the data could be ensured and the communication burden as well as the risk of potential cyber intrusions can be reduced.

- As the PMU's local computing capability is fully utilized and/or cost-effectively improved, the performance of the entire PMU WAMS can be strengthened.

- The measurement performance of the PMU sensor would be improved as the event type could be detected in real-time and, accordingly, a proper SEA is selected in an automated manner for high-fidelity measurements.

The main contributions of this dissertation is to design, develop, and test the next-generation smart sensors in power grids enabling distributed intelligence [46–52]. Such an edge computing approach could transform the way that PMU data is being handled, processed, and delivered across the grid. This type of smart sensor technology will be embedded with the following analytical modules:

- A pseudo-continuous quadrature wavelet transform (PCQ-WT) will be developed to process the single and/or three-phase (voltage and current) waveforms and effectively performs an online pattern recognition and feature extraction.

- Built on the PCQ-WT-extracted features, a machine learning mechanism, i.e., the convolutional neural network (CNN), is developed to detect and classify different events based on the scalograms obtained from PMU's input waveforms in real-time.

- Founded on the Quadrature Delayed Signal Cancellation (QDSC) and

Gaussian Weighted Taylor series (GWT) principles, two fast and accurate SEAs, that meet the majority of IEEE standard requirements respectively for the Protection (P)-class and Measurement (M)-class applications, will be developed.

- An efficient SEA selection scheme is developed to be housed within the smart sensor that adaptively selects the most promising SEA algorithm which best suites the detected event and ensures high-fidelity measurements at all times.

Additionally, two fast and accurate SEAs are proposed, that meet the IEEE standard requirements respectively for the P-class and M-class applications and can be implemented for improving the synchrophasor measurements under various conditions. In this dissertation research, the performance of the proposed distributed intelligence framework is tested and verified on several event detection applications in power grids.

1.5 Dissertation Outline

The remainder of this dissertation is organized as follows:

- Chapter 2 reviews the existing literature on power grid resilience, as well as the event detection and monitoring services for online situational awareness. These approaches are classified and reviewed in two categories of (i) with assistance of PMU sensors and (ii) with conventional measurements. Meanwhile, the synchrophasor estimation algorithms through time domain and frequency domain approaches are reviewed.

- Chapter 3, first introduces an overview of the proposed smart sensor technology and its configuration. Then, a background on the wavelet

transforms and the CNN machine learning mechanism is given. The proposed analytical advancements that are embedded within the smart sensor technology are elaborated next, which include (i) the suggested PCQ-WT signal processing algorithm for online pattern recognition and feature extraction on electrical waveforms; (ii) proposed CNN machine learning algorithm for real-time event detection and classification in power grids; (iii) the developed adaptive SEA selection scheme and the proposed estimation algorithms for high-fidelity synchrophasor measurements. The performance of each module is extensively analyzed and numerically investigated under variant conditions.

- Chapter 4 presents the existing High Impedance Fault (HIF) event modeling techniques, and accordingly, the proposed HIF event detection schemes are introduced. Detailed information on the proposed HIF model and a modified detection engine based on the proposed smart sensor solution for HIF detection are presented next. At last, case studies and numerical results are conducted and the performance of the suggested HIF detection technology is analyzed and validated.

- Chapter 5 introduces the modeling of Geomagnetically Induced Current (GIC) and its impacts on the power grid. Then, a GIC event detection scheme, which is based on a modified smart sensor event detection engine and a hybrid feature extraction tool by using WT and Short Time Fourier Transform (STFT), is proposed. The performance of this hybrid GIC detection mechanism is tested and verified under various grid operation conditions.

- Chapter 6 presents an innovative approach of using one single smart sensor solution to detect, identify, and differentiate the power grid

topology changes that might happen due to faults or manual operator interventions. Numerical case studies are performed to verify this proposed solution and experiments show that the suggested sensor technology can provide promising outcome in detecting the network topology changes under different triggering conditions.

- Chapter 7 summarizes this dissertation research and highlights the the contributions of this research work. Recommendations for the future work on the use and applications of the proposed smart sensor technology are also provided. At last, publications during this dissertation effort are listed,

Chapter 2: LITERATURE SURVEY

2.1 Electric Power Grid Resilience

Well-known reliability principles have been widely adopted in practice to have the power grid operate securely and reliably under normal conditions and safely withstand credible contingencies (e.g., N-1 criterion). Nevertheless, traditional reliability metrics do not focus on the High Impact Low Probability (HILP) incidents in the power grid [8]. While not-frequently experienced, one single HILP event can cause widespread power outages that affect a large number of customers, or even result in a total blackout [53–56]. Once the electricity outages occur, billions of dollars economic loss can be caused and human lives can be threatened or even lost. Therefore, enhancing the resilience of the electric power grid is of critical importance. Consequently, less frequent major outages would be ensured and the negative impacts on our society are reduced. On the other side, the concept of *Resilience* to a wide variety of HILP events has been quite discussed in the literature in recent years and solutions have been proposed [5, 46–48, 55–68]. However, its definition is unclear and not standardized so far. Meanwhile, the concept, definitions, and quantification measures of the “power grid resilience” has remained less clarified and unfocused. The word “resilience” is derived from the Latin word "*resilire*" highlighting “the ability to rebound” [69] and can be defined from many different perspectives.

For instance, the National Infrastructure Advisory Council (NIAC) proposed a universal definition of infrastructure resilience in 2010: “*the ability to reduce the magnitude and/or duration of disruptive events. The effectiveness of a resilient infrastructure depends on its ability to anticipate, absorb,*

adopt to and/or rapidly recover from a potentially disruptive event." [70]. In the context of the power grid, the Electric Power Research Institute (EPRI) [71] describes the resiliency including the ability to harden the system against—and quickly recover from HILP events such as extreme weather events—hurricanes, earthquakes and tsunamis. National Academies of Sciences, Engineering, and Medicine provided a similar and more specific definition of power grid resilience as follows:" *Resilience is not just about lessening the likelihood that these outages will occur; it is also about limiting the scope and impact of outages when they do occur, restoring power rapidly afterwards, and learning from these experiences to better deal with events in the future."* [72].

A typical power system performance evaluation framework following a disturbance is illustrated in Figure 2.1, where the vertical axis represents the power grid performance over a period of time captured in the horizontal axis. A transitional power system operation (red dash line) with resilience-assured performance should possess the following features and principles [46, 73, 74]

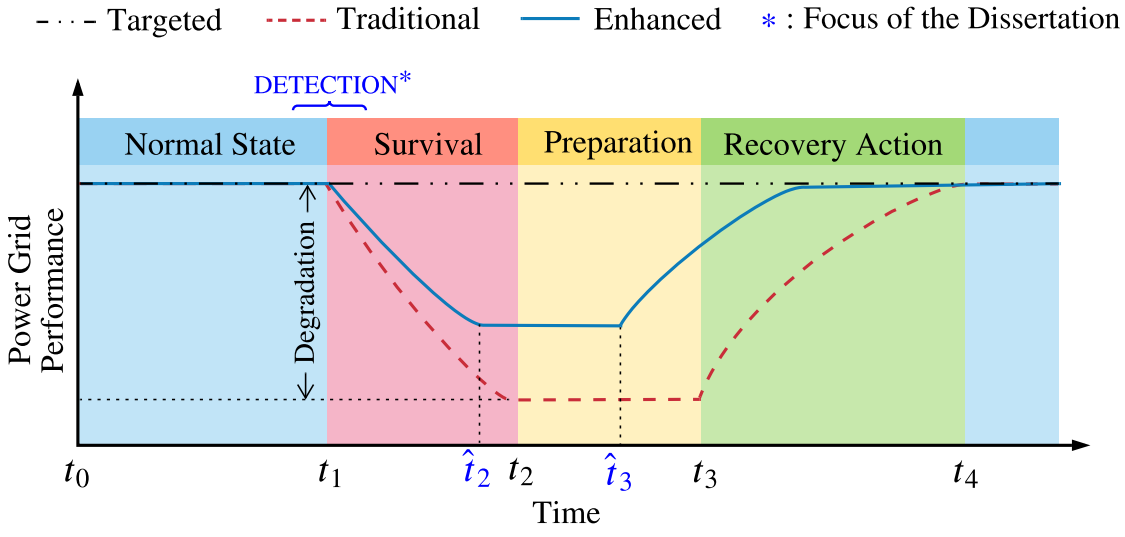

Figure 2.1: General representation of power system resilience to an extreme event over time

1. *Normal Operation Stage*: Between the starting point t_0 and the point when a disturbance occurs at t_1, advanced forecasting systems and decision-making strategies are deployed to anticipate and effectively deal with the upcoming disruption (e.g., an approaching hurricane). Meanwhile, at this stage, power system always operates in the desired and optimal state facilitated by timely maintenance and asset management of the grid and its components [75–83].

2. *Surviving Stage*: As the system is equipped with adequate survivability, the initial impacts of the disruptive event is a a degradation of the system performance to some extent starting from t_1, until it reaches to a minimum at t_2.

3. *Reparation Stage*: With the help of robust and resistant configurations, settings, and technologies as well as the available emergency management resources, the preparation and recovery process begins at t_2, at which the collapsed infrastructures start restoring, and damaged equipment and devices get repaired and replaced [84–89]. Segments with outages are ready to be re-energized in the next stage at t_3.

4. *Recovery Stage*: Following the previous stage, the impacts of the disruptive event are mitigated and the system performance elevates at t_3 until it reaches its full functionality at t_4.

This dissertation focuses on enhancing the resilience of the power grid by providing fast event detection and classification functions, which can accurately and timely assist the power grid to better resist the disturbances by taking corresponding hardening and adaptive responsive strategies before or quickly following their occurrence. As a result, with the enhanced resilience in the power grid (blue line), the performance degradation is reduced and

the preparation, as well as the recovery process can take place earlier than the traditional settings.

2.2 Event Detection in Power Grids

2.2.1 Event Detection without Synchrophasor Measurements

Event detection has been one of the long-lasting research topics among researchers as it is one of the extremely crucial elements for reliable online surveillance and secure operation of the power system. Before the widely-installed PMU networks appear, many research and methods have been proposed for enhancing the situational awareness in power grids. The authors in [90] proposed a power quality disturbance feature extraction approach. This approach calculates and analyzes offline using synthetic waveforms/signals and is subsequently validated using field measurements. This research proves that the feature extraction step is necessary to classify disturbances effectively and with low computational effort. In [91], a method for detection and classification of power disturbances using a sparse signal decomposition approach on over-complete hybrid dictionary matrix is presented. This method first decomposes the power signal into detail and approximation signals that contain impulse and sinusoidal elementary waveforms. The detail signal captures transient features (impulsive and oscillatory) and waveform distortions (harmonics and notching); meanwhile, the approximation signal contains fundamental power features of short- and long-duration variations (e.g., sags, swells, and interruptions). Finally, a hierarchical decision-tree algorithm is used for classification of disturbances. In [92], an intelligent protection scheme for microgrids using combined wavelet transform and decision tree is introduced. This scheme

retrieves current signals at the relaying point and uses wavelet transform to derive effective features such as the change in energy, entropy, and standard deviation through wavelet coefficients. The decision tree is developed for the fault classification task by processing the wavelet based features derived from sequence components and the features derived from the current signals. Using the extracted features based on tunable-Q wavelet transform, Reference [93] proposed an automated recognition approach through a dual multi-class support vector machine (SVM) for detection of power quality disturbances. The wavelet is tuned for decomposition of signal into fundamental and harmonic components, where the presence of low-frequency inter-harmonics is also analysed. Then, the power quality disturbances are categorized into two groups, and for each group, disturbances are recognized by employing a dual multi-class SVM. To mitigate the adverse effects of power swing on the conventional distance relays and avoid relays' maloperations (mistaken relay tripping), authors in [94] presented a frequency domain approach which can distinguish faults and the power swing phenomena; a wavelet-neuro-fuzzy combined approach is also proposed for fault location applications. The wavelet transform captures the dynamic characteristics of the fault signals, where a fuzzy inference system and the adaptive-neuro-fuzzy inference system are both used to extract important features and thereby to provide detection and classification for a consequent fault location. A conceptual framework for power grid multi-event detection and unmixing is presented in [95], where events are treated as mixtures of more than one constituent root event. This framework aims to analyze events that go beyond what are immediately detectable in a system and provides high-resolution data for an improved situational awareness. In this framework, the event formation process is considered as a linear mixing;

also a non-negative sparse event unmixing algorithm for multiple event separation and temporal localization using data collected from frequency monitoring network is proposed.

2.2.2 Event Detection with Synchrophasor Measurements

With the synchrophasor measurements available from PMUs installed in electric substation across the power grid, the situational awareness and the resiliency of the grid can be further enhanced. Many research has been done on power system real-time event detection using synchrophasor measurements, which improves the operators' ability to predict, prevent and mitigate the undesired impacts on the power grid and to timely avoid cascading outages. Utilizing the information extracted from the PMU datasets, [96] introduced a backup protection technique for wide area power transmission grid. This protection scheme compares positive sequence voltage magnitudes at each bus during fault conditions and locates the nearest bus to the fault. Then, the differences in the positive sequence current angles are used to detect the faulted line. [97] proposed a PMU based protection scheme for transposed and un-transposed parallel transmission lines. This scheme is based on the distributed line model and the synchronized phasor measurements at both ends of the transmission lines. By using eigenvalue/eigenvector theory to decouple the mutual coupling effects between parallel lines, the fault detection and location indices are derived for the protection applications. In [98, 99], different line outage detection techniques using phasor measurements from PMUs are presented. Reference [98] developed an algorithm which uses known system topology information, together with PMU phasor angle measurements, to detect system line outages. Additionally, an estimation method for the pre-outage flow on the outage line is

proposed. In [99], a combination of pre-outage topology information and real-time phase angle measurements from PMUs is used for double line outage detection. A real-time event detection method and data archival reduction based on synchrophasor measurements from PMUs are proposed in [100] to identify the voltage magnitude events and real power events for a small-scale microgrid application. This method is based on principal component analysis (PCA) and a second order difference method with a hierarchical framework. [101] presented a data-driven algorithm based on local outlier factor to detect and locate events in power systems using reduced PMU data. In [101], the unequal-interval reduction method is presented to reduce the scale of PMU data. Then, a PCA-based similarity search method is applied to compare the differences of the operation state between any two buses. At last, local outlier factor is used to detect the abnormal events in power systems and to determine the region where the event is originally triggered from.

Synchrophasor measurements from PMUs can also be used for power grid fault detection: [102] employs PMU measurements recorded during the fault for determination of the fault currents flowing on the faulted line and locating the fault through a weighted least squares estimator. This method reduces the required number of measurements for the solution of the fault location problem by making use of the fast refresh rates of the PMUs. [97] developed an algorithm to identify high impedance fault using statistical analysis of the utility PMU measurements at substations. Fault thresholds used in rules are determined based on theoretical values and real-world recorded PMU data during fault events. A rule-based data-driven approach to detect fault location and perform fault classification is proposed in [103]; this approach relies on rules created using PMU measurement

data without the knowledge on the power system's topology and its physical characteristics. Synchrophasor data from PMUs can also be used to cluster the most coherent generating units [11] and then applied for detecting and predicting the critical generating units in the grid [104].

2.3 Synchrophasor Estimation Algorithms (SEAs)

There are many different types of algorithms for phasor measurements. Typically, the existing phasor estimation methods can be mainly categorized into time-domain and frequency-domain methods.

2.3.1 Time Domain SEAs

Reference [105] proposed a hybrid adaptive filter based on a modified Gauss-Newton adaptive linear element to estimate the fundamental and harmonic phasors along with the frequency change of non-stationary power system signals. An objective function based on the weighted square error is minimized where the computational load and time are reduced.In [106], an estimator based on the combination of harmonic components is introduced to provide accurate phasor as well as harmonic measurements in off-nominal power frequency conditions.The authors in [107] estimate the phasor under the grid dynamic conditions using a Double Suboptimal-scaling-factor Strong Tracking Kalman Filter (DSTKF)-based algorithm and a linearized complex exponential of the signal using a K^{th} Taylor polynomial.An approach for estimation of alternating current signal fundamental phasor under dynamic conditions is introduced in [108]. A model-order estimation method is used to separate the signal space and the noise space in the signal correlation matrix. Then, the Vandermonde matrix obtained from the signal parameters' total least square estimation through rotational

invariance techniques is extended to second-order Taylor's series approximation and used to estimate the dynamic phasor of the current signal. Reference [109] proposed a dynamic phasor estimation method for protective relays, which captures the fundamental frequency component with time-variant amplitude. The fault current is treated as a combination of a decaying dc offset, a decaying fundamental frequency component and harmonics with constant amplitudes. Least square technique is used to estimate the magnitudes and the time constants of each decaying component. Authors in [32] proposed adaptive cascaded filter algorithms for both P- and M-class PMUs.

2.3.2 Frequency Domain SEAs

The frequency-domain methods have been widely used, which are commonly featured with the calculation simplicity and stable performance. The frequency approaches develop filters centered at the fundamental frequency to extract the phasor of interest. For example, [110] uses a classic Kalman filter on Taylor series polynomial to form flat magnitude and phase responses. This approach provides phasor estimates without magnitude or phase distortion.Reference [111] presented a dynamic phasor estimation approach through a second-order Taylor polynomial. This estimation approach approximates the phasor by a state vector, which contains the estimate of the dynamic phasor and the estimates of its derivatives as well. The authors in [112] proposed a phasor measurement solution by a weighted least squares of Taylor approximation. This approach provides a filter with frequency response around the fundamental frequency and low sidelobe level over the stopband. Also, a linear phase response is obtained, and their estimates are free of amplitude and phase distortion.The

phasor parameter estimates in [113] are achieved through the Taylor-based weighted least-squares (TWLS) approach. This presented phasor estimator and its derivatives are expressed as weighted sums of the discrete-time Fourier transform (DTFT) of the analyzed waveform and its derivatives. The phasor estimation approach from [114] consists of the interpolated discrete Fourier transform (DFT) and the Taylor-Fourier transform. The authors further reduced the computational complexity and improved the efficiency of this combined approach; moreover, a promising accuracy in the main testing conditions is ensured.In [33], an enhanced Interpolated DFT for synchrophasor estimation in FPGAs is proposed and validated.A symmetric TWLS (STWLS) filter to iteratively estimate the parameters of the positive image of the fundamental component is also proposed in [115].In [116], an instantaneous oscillating phasor estimation algorithm using Taylor^K-Kalman filters is proposed, where a state-transition matrix with a sinusoidal signal model obtained by Taylor polynomial is used to capture the amplitude and phase fluctuations between one signal sample and the next with the Kalman procedure. This method allows the Kalman filter to estimate both phasor and its derivatives. Reference [117] proposed a compressive sensing Taylor-Fourier multi-frequency joint approach for synchrophasor measurements. In this approach, the most relevant components of the signal are identified and the impacts of dynamic conditions, harmonic and inter-harmonic interferences are suppressed.

Chapter 3: Proposed Smart Sensor Technology

3.1 Abstract

An innovative smart sensor technology with distributed event detection functionality and adaptive SEA selection mechanism for online surveillance is presented in this chapter. In the proposed smart sensor technology, the waveform patterns and signatures are extracted via a time-frequency domain analytic—wavelet transform (WT) [48, 51]. Built on the WT-extracted features, i,e. scalograms, a machine learning mechanism based on convolutional neural networks (CNNs) [49, 118] is employed to detect and classify the events through a pattern recognition process. This proposed solution could eliminate the potential risks to communication failures, delays/latencies, and cyber-attacks, system monitoring and control paradigms should enable fusing the online measurements in a distributed manner; that is building in distributed intelligence and translating the data to valuable information closer to where the data is generated (i.e., in substations).

3.2 Big picture of the Proposed Sensor Technology

Voltage and current waveforms in power grids reveal a certain pattern with unique features and peculiarities driven by the system operating conditions. For instance, waveform magnitudes and angles can go through step changes during faults; measurements can be noisy; unbalanced load, voltage surge or sag, harmonics, and frequency drift are also common phenomena. The event classification problem in power grids could be then decomposed into two steps. First, the signatures and dominant patterns

from the electrical waveforms, which convey valuable information on the underlying events, are extracted. Second, a classifier is employed for event detection and classification based on the extracted features. Motivated by these concepts, the proposed smart sensor is developed. Figure 3.1 illustrates the algorithmic process proposed to be embedded within the smart sensors, which is achieved through the following four steps: (i) Signal Acquisition; (ii) Feature Extraction; (iii) Event Detection; and (iv) SEA Selection.

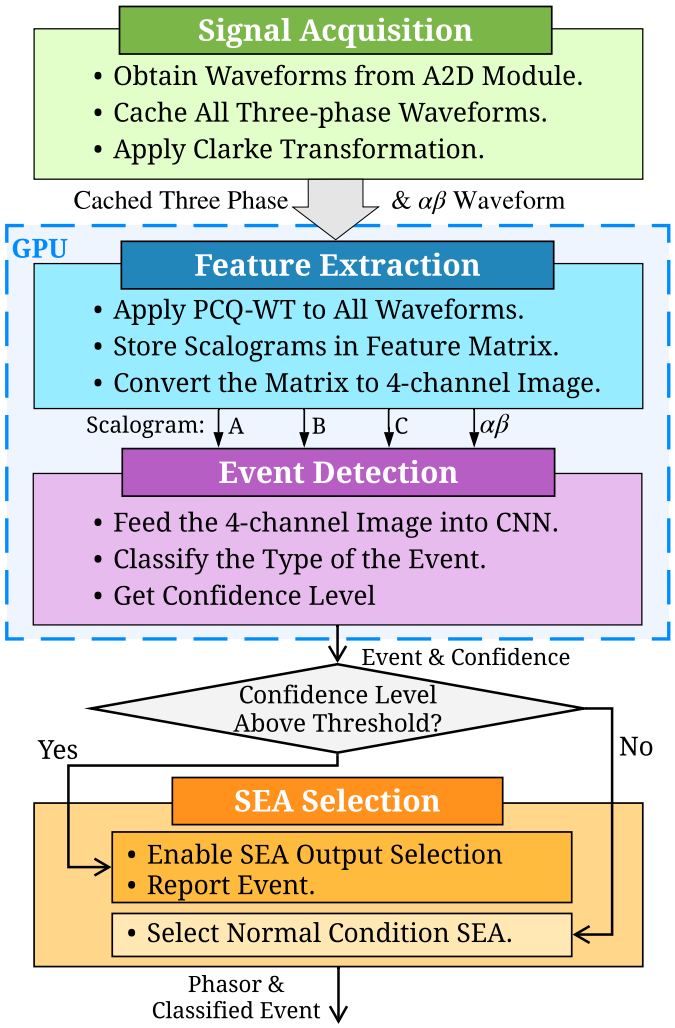

Figure 3.1: Big picture of the algorithmic process within a smart sensor.

The proposed technology shares exact same input signals (voltage and

current) as the existing PMUs in power grids, with no additional device nor investment for data acquisition. ***First***, the sampled three-phase waveforms captured by the Analog to Digital (A2D) converter within the proposed sensor are loaded into the buffer. ***Second***, the original and the Clarke-transformed waveforms are individually processed and features (scalograms) are extracted using the proposed PCQ-WT signal processing algorithm. To accelerate the consequent event classification, the scalograms are converted into images. The event classification in the ***Third*** step is, therefore, recast as an image classification process, where the scalograms are fed into several parallel CNN machine learning modules embedded within the Graphical Processing Unit (GPU) for event detection and classification. Since the processing time must be sufficiently low for online applications, a simple CNN architecture is proposed that also meets a designated accuracy requirement under a wide range of fast- and slow-dynamic events in power grids. The machine learning mechanism will finally detect and classify the event, attributed with a confidence level. Under certain circumstances, the patterns/features in the scalograms could be extremely similar for different types of events, and the predicted event (with the highest confidence level) could interchange between several types in a short period of time. Hence, a threshold criterion for the output confidences is established to make a solid decision on event detection and classification. Following the detected event (with the confidence level above a threshold), an adaptive SEA selection mechanism is devised in the ***fourth*** step that will adopt the most promising SEA outputs among a suite of embedded SEAs (high-speed and high-accuracy algorithms) for online measurements. If the confidence level is reported lower than the designated threshold, the system is concluded to be in its normal operating condition and the default SEA output will be used for accurate measurements.

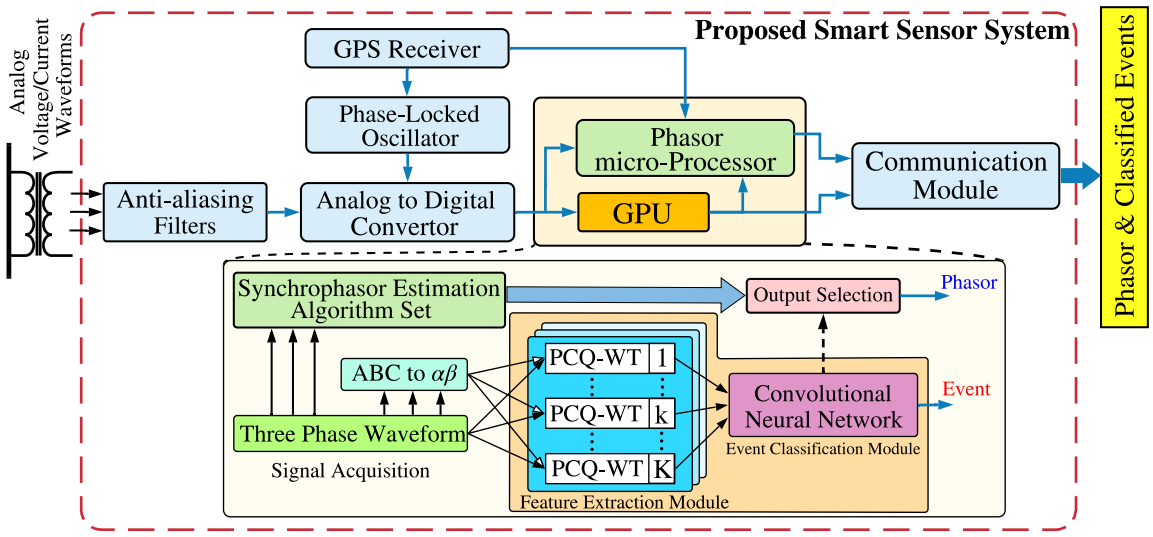

Figure 3.2: Architectural design of the proposed smart sensor technology.

The overall hardware architecture of the proposed smart sensor technology is illustrated in Fig. 3.2. One GPU is the only additional hardware required in the proposed system configuration compared to the conventional PMUs, where the GPU shares the same inputs of the phasor processor. All core operations described in Fig. 3.1—which are in fact the high-speed matrix operations—are performed in the GPU. This minimal hardware modification makes it viable for the proposed functionalities to be deployed in stand-alone smart sensor units or embedded within the existing PMUs.

3.3 Technical Background

3.3.1 Electrical Waveforms

The three-phase time-domain sinusoidal waveforms fed into the PMUs can be mathematically represented as follows:

$$x_{ph}(t) = A_{ph}(t)cos\left(2\pi F_h(t) + \phi_{ph}(t)\right), \tag{3.1}$$

where $x_{ph}(t)$ is a one-dimension (1-D) waveform measured at each phase; $A_{ph}(t)$, $F_h(t)$, and $\phi_{ph}(t)$ are the instantaneous magnitude, fundamental frequency, and phase angle in each phase, respectively. The waveform in each phase can be expressed by a summation of different orders of harmonic components, as presented in (3.2):

$$x_{ph}(t) = \sum_{h=1}^{H} A_{ph,h}(t) cos\left(2\pi F_h(t) + \phi_{ph,h}(t)\right), \tag{3.2}$$

where h is the order of harmonics, and H is the maximum order of harmonic of interest. In different grid operating conditions, different values of $A_{ph,h}(t)$, $F_h(t)$, $\phi_{ph,h}(t)$ will appear in the three-phase power signal, resulting in different patterns and peculiarities. To simplify the time-domain sinusoidal signal analysis and relaxing the need to acquire the rotating reference frame in the Park transformation [119], Clarke transformation is applied to convert the three-phase signal from ABC- to $\alpha\beta$-frame, as presented in the following:

$$x_{\alpha\beta}(t) = x_\alpha(t) + j x_\beta(t), \tag{3.3}$$

$$\begin{bmatrix} x_\alpha(t) \\ x_\beta(t) \end{bmatrix} = \begin{bmatrix} \frac{2}{3} & -\frac{1}{3} & -\frac{1}{3} \\ 0 & \frac{\sqrt{3}}{3} & -\frac{\sqrt{3}}{3} \end{bmatrix} \begin{bmatrix} x_A(t) \\ x_B(t) \\ x_C(t) \end{bmatrix} \tag{3.4}$$

3.3.2 CWT and Pseudo-CWT

Since power waveforms contain various frequency components, multi-resolution waveform analytics are suitable to extract the signal signatures and dominant features, i.e., amplitude, frequency, and phase angle. The most commonly-used technique is the short-time Fourier transform (STFT) [110, 120] and the wavelet analysis [48, 121]. Studies show that STFT

is attributed a higher computational burden and time, which leads to a lower time resolution than the wavelet analysis in time-frequency domain [122, 123]. Meanwhile, when comparing the STFT spectrogram in Fig. 3.3(a)(b) and the scalogram of the continuous wavelet transform (CWT) in Fig. 3.3(c)(d)(e) and (f), one can notice that even though STFT provides higher frequency accuracy, CWT offers more conspicuous performance for feature extraction. Furthermore, the event detection module would benefit from the waveform features rather than an accurate frequency measurement. In this dissertation, therefore, wavelet analysis is selected as the main mathematical tool for online feature extraction and waveform monitoring.

The wavelet transformation is achieved via the cross-correlation between the signal of interest $x(t)$ and designated wavelets, as follows:

$$X(\omega|a,b) = \frac{1}{\sqrt{|a|}} \int_{-\infty}^{\infty} x(t) \Psi^{*}(\frac{t-b}{a}) dt \tag{3.5}$$

where $\Psi(t)$ is a mother wavelet; * denotes the complex conjugate; a and b are scaling factors and time shift, respectively; and $\Psi(\frac{t-b}{a})$ is one of the "daughter wavelets" of $\Psi(t)$ [124, 125]. With different selections of a and b, a wavelet bank is then determined. By selecting proper intervals for the *continuous* scaling factor along with the time shift, a CWT is achieved [126].

In a smart sensor, the real-time signals are sampled and discrete signal processing is applied. The continuous-time to discrete-time (C2D) conversion will, however, sabotage the continuity of the signal. Mathematically, the daughter wavelets' length, so called the "wavelet window size", is limited and the scaling factor is finite due to the processing capacity limitations of the computing hardware. For all these reasons, the actual behavior of the conventional CWT within the processor is discrete WT with a set of discrete

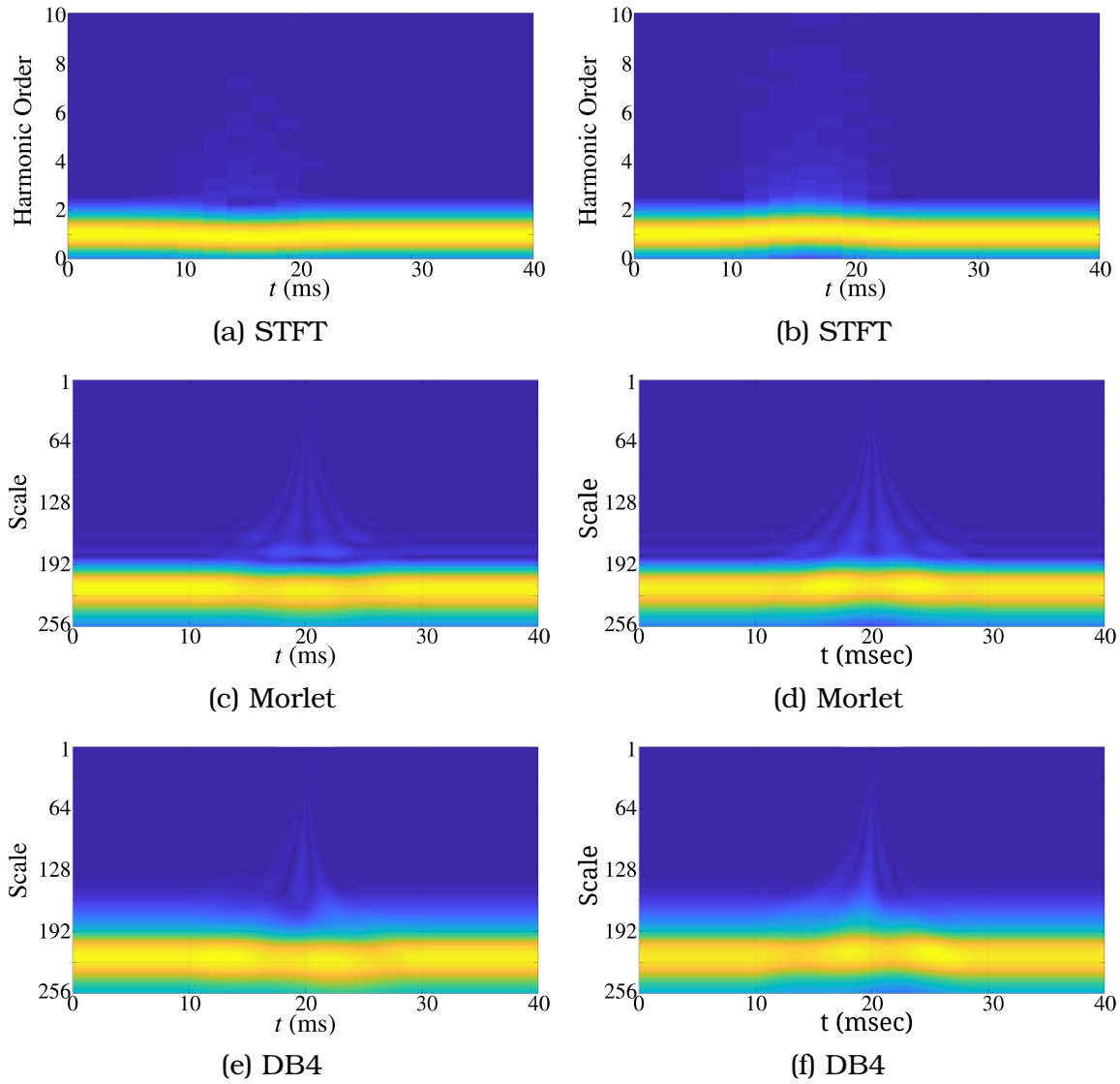

Figure 3.3: Comparison of the STFT vs. Morlet CWT & DB4 CWT on quadrature signals during: (a),(c),(e) -2Hz frequency jump; (b),(d),(f) 40° phase jump.

scaling factors a^i, wherein, i is an integer. In the proposed *Pseudo*-CWT, i is chosen from a set of linearly-increasing real numbers instead of integers. Similar to the discrete WT, the PCWT with one discrete scaling factor is defined as follows:

$$X[\omega|a_k,b_k] = \frac{1}{\sqrt{|a_k|}} \sum_{n=0}^{W-1} x[n]\Psi^*[\frac{nT_s - b_k}{a_k}] \tag{3.6}$$

where, T_s denotes the sampling interval, and W stands for the window (buffer) length. In a CWT, each daughter wavelet needs to cover a designated frequency range that reflects the features in time-frequency domain. The central frequency of the daughter wavelets can be approximated by the following relationship with the scaling factor:

$$f = F_c/a_k \tag{3.7}$$

where, F_c is the central frequency of the mother wavelet [127]. When a vector of scaling factors with length K is chosen, the wavelet bank Ψ and the extracted features at time instant n are expressed by the following equation:

$$\begin{aligned} \mathbf{\Psi}^{K\times W} &= \left[\Psi\left[\tfrac{nT_s-b_1}{a_1}\right],\cdots,\Psi\left[\tfrac{nT_s-b_k}{a_k}\right],\cdots,\Psi\left[\tfrac{nT_s-b_K}{a_K}\right]\right]^{\mathscr{T}}, \\ \mathbf{X}_{\underline{\omega}}^{K\times 1}[n] &= \left[X_{\omega 1}(a_1,b_1),\cdots,X_{\omega k}(a_k,b_k),\cdots,X_{\omega K}(a_K,b_K)\right]^{\mathscr{T}}. \end{aligned} \tag{3.8}$$

Where, $\mathscr{T}$ is the conventional transpose. To cover a sufficiently wide range of frequency and provide adequate pattern information for time-frequency analysis in any given operating condition, the central frequency of mother wavelets F_c and the largest scaling factor a_K must satisfy the following condition:

$$\frac{F_c}{a_K} < f_0 < F_c, \tag{3.9}$$

where, f_0 is the frequency of the signal of interest. F_c needs to be chosen from a higher frequency range than the maximum frequency of interest and scaled down by a_k. Hence, as a_k increases, the corresponding frequency of the PCWT output decreases in the frequency domain. Once the scaling factors are chosen, then (3.8) is able to generate the wavelet bank and a series time bin of $\mathbf{X}_{\underline{\omega}}^{K\times 1}$ along the time instants, i.e. the PCWT scalograms are achieved.

During the feature extraction process, both transforms require a window (buffer) of samples and, thus, a latency effect indeed exists. Selection of a proper window size could minimize the latency effect, but at the cost of trading off the frequency resolution.

3.3.3 Convolutional Neural Networks (CNNs)

At this stage, we consider the obtained scalograms as 2-D images, and the event classification problem turns into a supervised image classification process. The conventional paradigm for image classification is to manually design the feature extractor and then reduce the dimensionality of the data, where the second phase is to employ a classifier to classify the lower dimensional features. This paradigm highly depends on the efficient design of the feature extractor; manually designing features for a complex task requires a great deal of human time and effort; it can take decades for an entire community of researchers [128]. In contrast, Convolutional Neural Networks (CNNs) are able to learn the extracted features automatically and have been proven very successful in the broad range of image-related tasks [129–131]. By definition, CNNs are simply neural networks that use convolution in place of general matrix multiplication in that least one of their layers [128]. In general, the implementation of the convolution is through cross-correlations as defined by

$$\boldsymbol{s}^p(m,n) = \sum_u \sum_v \sum_w \boldsymbol{I}^u(m+v, n+w)\boldsymbol{K}^p(v,w), \tag{3.10}$$

where $\boldsymbol{s}^p(m,n)$ is the output of the convolutional layer at position (m,n) and p–th channel; $\boldsymbol{I}^u$ is the u–th channel of the image/data volume, and $\boldsymbol{K}^p$ is the p–th convolutional kernel. A complex convolutional layer is composed

of a small number of simple layers [128] expressed by the following:

$$\boldsymbol{I}_l = pool\left(\sigma(\boldsymbol{s})\right), \tag{3.11}$$

where, $\boldsymbol{I}_l$ represents the output volume of the l–th layer, $\sigma(\cdot)$ is the non-linearity of the neurons, and $pool(\cdot)$ is a down sampling procedure. By stacking the convolutional layers, the abstraction capacity of the network generally increases [132].

The representations of the last convolutional layer are expanded to vectors and processed by the general fully-connected layers; this transform the representations with more nonlinearities into spaces with different (higher or lower) dimensions. The final layer of a CNN reduces the dimensionality of the representations to the number of classes; cross-entropy is then employed to measure the "goodness" of the classification (Kullback-Leibler divergence between the predicted distribution and the target distribution) [133]. Finally, gradients of the cross-entropy loss function with respect to the parameters would help train the CNN by back-propagation.

3.4 Proposed Analytics within the Smart Sensor

3.4.1 The Proposed PCQ-WT for Online Feature Extraction

To identify an event in each phase, the corresponding features need to be observed over time. As the positive-sequence frequency and phase angles are of interest for both $x_{\alpha\beta}(t)$ and $x_{ph}(t)$ during synchrophasor measurements, we propose a quadrature PCWT to extract the waveform features and signal signatures. Meanwhile, the waveform captured in each phase is real, and the 1-D waveform (3.2) can be expanded by the Euler's formula to adopt

the quadrature wavelet transform:

$$\begin{aligned} x_{ph}(t) = & \frac{1}{2}\sum_{h=1}^{H} A_{ph,h}(t)e^{j\phi_{ph,h}(t)} \cdot e^{j2\pi F_h(t)} \\ & + \frac{1}{2}\sum_{h=1}^{H} A_{ph,h}(t)e^{-j\phi_{ph,h}(t)} \cdot e^{-j2\pi F_h(t)}. \end{aligned} \tag{3.12}$$

The next step is to select an appropriate wavelet and investigate its feasibility for waveform feature extraction. Gabor wavelets have been widely used in two-dimension (2-D) pattern recognition [134–136]. In order to simplify the design and enhance the computational efficiency, a modified complex Gabor wavelet is adopted in this research work as written below

$$\Psi(t) = \underbrace{exp\left(j\omega_c(t-b)\right)}_{\substack{\text{Periodic} \\ \text{Component}}} \cdot \underbrace{exp\left(-\frac{(t-b)^2}{\alpha_0^2}\right)}_{\substack{\text{Gaussian} \\ \text{Envelope}}}, \tag{3.13}$$

where, w_c is the central frequency. The Fourier transform of this Gabor wavelet is

$$\mathbf{F}_\Psi(\omega) = \alpha_0\sqrt{\pi} \cdot exp(-j\omega b) \cdot exp(-\frac{\alpha_0^2}{4}(\omega-\omega_c)^2). \tag{3.14}$$

One can see that the Fourier transform of the Gabor wavelet is also a function on the theme of the Gabor wavelet, although the Gabor wavelet transforms do not follow the orthogonal property since

$$|\mathbf{F}_\Psi(\omega_c \pm \varepsilon)| \neq 0, \tag{3.15}$$

where, ε is a small value. According to (3.14), this Gabor wavelet possesses a characteristic of predictable narrow bandwidth. By properly selecting α_0, one of the Gabor WT can cover a desired range of frequencies and the time shift b plays no magnitude impact on (3.14) and (3.15). To ease the

derivation, let $b=0$; then the CWT using the Gabor wavelet for a unit-length phasor with frequency $\omega_0 > 0$ turns into

$$\begin{aligned} X^{+}(\omega_0|a,b=0) &= \int_{-\infty}^{\infty} x(t)\Psi^{*}(\frac{t}{a})\mathrm{d}t \\ &= \int_{-\infty}^{\infty} exp\left(j(\omega_o - \frac{\omega_c}{a})t - \frac{t^2}{a^2\alpha_0^2}\right)\mathrm{d}t. \end{aligned} \tag{3.16}$$

According to the Hubbard–Stratonovich transformation [137],

$$exp(-\frac{\alpha}{2}x^2) = \sqrt{\frac{1}{2\pi\alpha}}\int_{-\infty}^{\infty} exp\left(-\frac{y^2}{2\alpha} - jxy\right)\mathrm{d}y, \tag{3.17}$$

the CWT using the Gabor wavelet in (3.16) becomes

$$X^{+}(\omega_0|a,b=0) = a\alpha_0\sqrt{\pi}exp\left(-\frac{\alpha_0^2}{4}(a\omega_0 - \omega_c)^2\right). \tag{3.18}$$

It can be seen that when $\omega_0 = \omega_c/a$, (3.18) reaches its maximum and the dominant feature of the expected frequency is revealed. In order to make each frequency of interest share an equivalent maximal magnitude, we make

$$\alpha_0 = \omega_c/(\gamma a), \tag{3.19}$$

where, γ is a constant. Hence, in (3.13), the Gaussian envelope in the Gabor wavelet is adaptive to different frequencies. While applied to the 1-D waveform, the feature corresponding to a unit phasor with negative frequency ($-\omega_0$) is always suppressed, because the CWT of the negative frequency in (3.20) decreases as ω_0 increases.

$$X^{-}(\text{-}\omega_0|a,b=0) = a\alpha_0\sqrt{\pi}exp\left(-\frac{\alpha_0^2}{4}(a\omega_0 + \omega_c)^2\right). \tag{3.20}$$

The discrete form of the Gabor wavelet that is used in a smart sensor is

presented as

$$\Psi[n|a_k,b_k] = \; exp\left(j\frac{\omega_c T_s(n-b_k)}{a_k}\right) exp\left(-\frac{T_s^2(n-b_k)^2}{a_k^2\alpha_0^2}\right). \tag{3.21}$$

When applying the complex Gabor wavelet with a set of discrete scaling factors, the proposed PCQ-WT is achieved as follows:

$$\begin{aligned} X(\omega_k|a_k,b_k=0) &= \sum_{n=0}^{W-1} x[n]\Psi^*\left[-\frac{T_s n}{a_k}\right] \\ &= \sum_{n=0}^{W-1} x[n] exp\left(-j\frac{\omega_c}{a_k}T_s n - \frac{T_s^2 n^2}{a_k^2\alpha_0^2}\right). \end{aligned} \tag{3.22}$$

If one determines the frequencies of interest and designs the Gabor wavelet bank properly, a vector $\mathbf{X}_{\underline{\omega}}$ consisting a set of PCQ-WTs is achieved, and the PCQ-WT is able to extract the waveform signatures in frequencies of interest via time-frequency analysis, i.e., scalograms are generated.

3.4.2 The Proposed CNN for Event Detection & Classification

Pursuing development of an online event detection and classification mechanism, and built on the PCQ-WT extracted features corresponding to various types of events, a machine learning algorithm, i.e., the CNN, is designed. As discussed earlier, the process of event detection is converted to a supervised classification process on the scalograms. However, the classification on the 2-D scalograms is challenging due to the high dimensionality. Specifically, every frame of the obtained scalogram has $scales \times time\ bins$ dimension (usually hundreds by hundreds); such high-dimensional data is prohibitive in most conventional pattern classification approaches. We treat the PCQ-WT scalograms as 2-D images and propose a CNN-based architecture to classify the events concealed in the scalograms (images).

As the scalogram classification is not with very high abstraction level, the proposed CNN has a simple architecture that meets the requirements of a synchrophasor, yet with very fast test speed. Our proposed CNN contains five layers: three convolutional (Conv.) layers and two fully-connected (FC) layers. This framework can be either a standalone tool for event detection and classification or can be functionally embedded within PMUs to assist the phasor processor in selecting a proper SEA in real-time.

3.4.3 The Proposed Mechanism for Adaptive Phasor Estimation

The event detection and classification module introduced in Section 3.4.2 provides valuable information on the grid operating conditions. We aim to demonstrate that the one-size-fits-all algorithm within the existing PMUs may neither be sufficient nor accurate in effectively dealing with all types of signals corresponding to different events and operating conditions in power grids. There are several solutions that can be thought in response to this challenge: (i) one very costly solution would be to install several different sensors (each with one different SEA) in each substation for different end-use applications that use the measurements; (ii) the other approach can be to design one very accurate SEA that can work very effectively under all system operating conditions meeting all measurement accuracy and speed requirements, which is extremely hard to achieve considering the hardware limitations as well as the ever-existing trade-off between the speed-accuracy performance requirements for different applications; (iii) one promising and viable approach in line with today's and tomorrow's infrastructure and computing technologies—which we focus on within the proposed smart sensor—, is to host a suite of SEAs that work in parallel within the sensor and are selectively and adaptively activated in an automated manner depending

on the unfolded system operating condition.

The detailed architecture of the proposed SEA selection module is shown in Fig. 3.4. For every detected event and identified operating condition, the best-fit measurements—phasor, frequency and ROCOF—are selected in real-time; therefore, the output selector should be equipped with an optimized strategy that dynamically switches between one or multiple SEAs. Among SEAs within the smart sensor, we propose two novel SEAs, one P-Class with promising estimation speed and one M-Class with high-accuracy measurements.

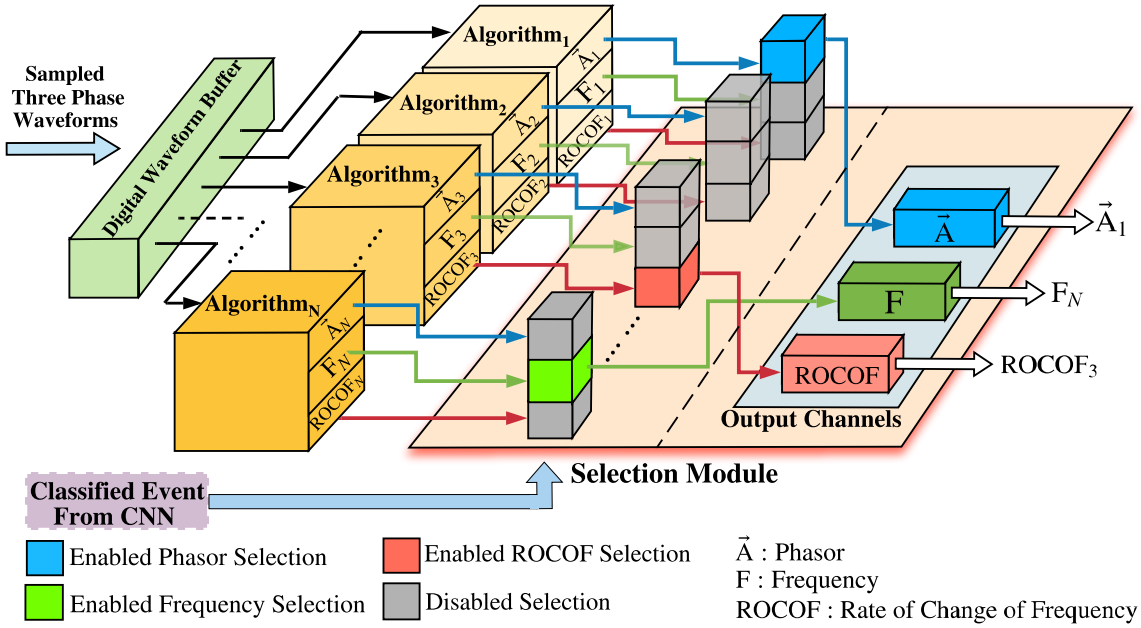

Figure 3.4: Architecture diagram of the developed SEA selection module.

3.4.4 The Proposed P-Class and M-Class SEAs

The overall architecture for the proposed P-Class and M-Class SEAs within a smart sensor is presented in Fig. 3.5. The sampled waveform is sent into the Quadrature Delay Signal Cancellation (QDSC) module to estimate the P-Class phasor magnitude (A_p). A functionally-programmed

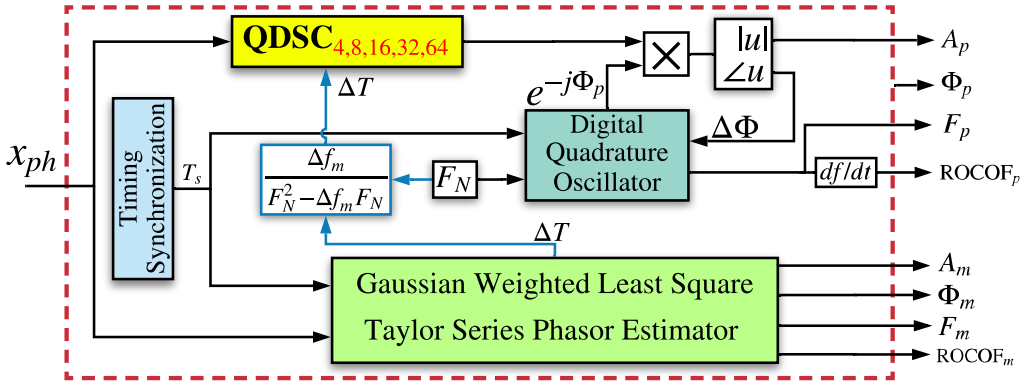

Figure 3.5: The proposed P-Class and M-Class SEAs within a smart sensor.

digital quadrature oscillator is used to assess the P-Class phase angle (Φ_p) and frequency (F_p) through eliminating the phase difference ($\Delta\Phi$) between the fundamental waveform and the quadrature oscillator. At last, the ROCOF$_p$ is estimated through the derivative of the measured frequency F_p. The M-Class phasor magnitude (A_m), phase angle (Φ_m), frequency (F_m), and ROCOF$_m$ are estimated from the Gaussian-Weighted Least Square Taylor Series SEA. Here, we abbreviate the proposed M-Class SEA as "GWT-M"; meanwhile, the GWT-M provides the deviation of the waveform's nominal period (ΔT) to the QDSC module. This, in turn, makes the proposed P-Class measurement adaptive to designated operating conditions. In our proposed framework, the timing synchronization is employed to drive the digital oscillator and to ensure an accurate measurement. The nominal fundamental frequency (F_N) and the period (T_N) is determined by the system frequency, i.e., 50Hz or 60Hz.

3.4.4.1 The Proposed P-Class SEA: Dynamic QDSC Filter Algorithm

The structure of the proposed QDSC algorithm is presented in Fig. 3.6. The discrete sampled waveform x_{in} is first cached in the buffer; a data selector selects the cached data by the index obtained through calculating

the closest integer value of $F_s(T_N+\Delta T)/n$, wherein F_s is the sampling rate and k is the delay factor. The selected data is then outputted from the buffer and multiplied by a unit static vector ($e^{j2\pi/k}$). Finally, the multiplication result and the original sampled input waveform at the current timestamp are summed and the output (x_{out}) of the QDSC module is reported.

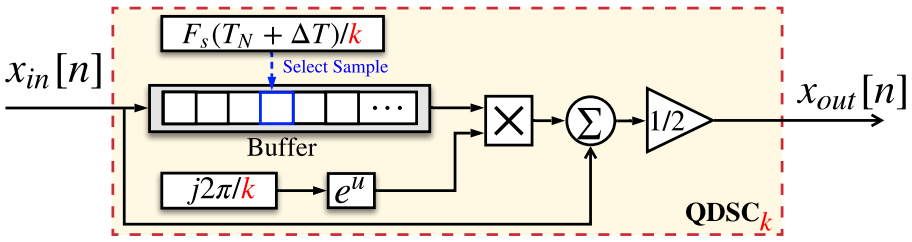

Figure 3.6: Functional diagram of the proposed QDSC$_n$ algorithm.

The transfer function of a QDSC filter is defined by

$$H(f)=\frac{1}{2}\left[1+exp\left(j\frac{2\pi}{k}\left(1-(T_N+\Delta T)f\right)\right)\right], \tag{3.23}$$

The value of k directly affects not only the buffer length and consequently the speed of the algorithm's dynamic response, but also the phasor measurement accuracy. We choose QDSC$_k$ in octave with $k=[4,4,4,8,16,32,64]$ connect all QDSC modules in cascade; as shown in the frequency response diagram presented in Fig. 3.7, all odd harmonics except the positive fundamental frequency ($h=1$) would be eliminated, the gain for $h=1$ is one, and no phase shift exists. Hence, this configuration could extract the positive-sequence fundamental phasor of one single-phase waveform in (3.12).

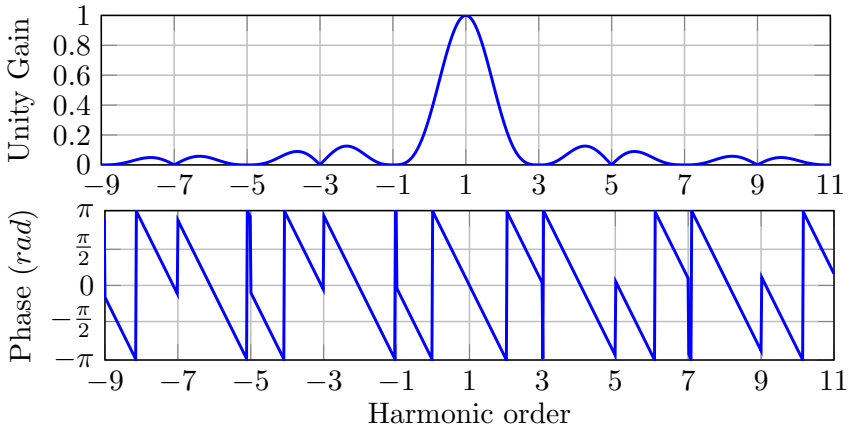

Figure 3.7: Frequency response of the cascaded QDSC$_k$ with k=[4, 4, 4, 8, 16, 32, 64].

3.4.4.2 The Proposed M-Class SEA: Dynamic Gaussian-Weighted Least Square Taylor Series (GWT-M)

Inaccurate estimation of ΔT in QDSC could potentially hinder a stable frequency response and desired performance in (3.23). Therefore, we introduce a simplified Gaussian-weighted least square Taylor Series SEA. We here express the cached fundamental waveform by (3.12) as follows:

$$x_{ph,1}[n] \triangleq x_{ph,1}(nT_s) = \frac{1}{2}\vec{A}_{ph,1}[n]e^{j2\pi F_N nT_s} + \frac{1}{2}\vec{A}^*_{ph,1}[n]e^{-j2\pi F_N nT_s}, \tag{3.24}$$

where "$*$" denotes the conjugate operation, and $\vec{A}_{ph,1}[n]$ is the static vector of the fundamental positive sequence at time slot n in the buffer, and $n=0$ indicates the current time slot. With $n=0,1,2,\cdots,N_{d\text{-}1},N_d$, a queue of sampled x_{ph} with length N_d+1 is obtained in the buffer at the current time slot. N_d needs to be an even number that guarantees an odd number of time slots in the buffer to estimate the phasors through Taylor series. Meanwhile, the peak of the Gaussian window is located in the middle of the cached waveform. Therefore, the phasor estimation physically has a constant delay with $N_d/2$ time slots. To compensate the phase shift caused by this delay,

the evaluation in (3.24) turns to be

$$\begin{aligned} x_{ph,1}[n] &= P[n] + P^*[n] \\ P[n] &= e^{j2\pi F_N \frac{N_d}{2} T_s} \cdot \frac{1}{2} \vec{A}_{ph,1}[n] e^{j2\pi F_N n T_s} \end{aligned} \tag{3.25}$$

The second-order Taylor polynomial of $\vec{A}_{ph,1}[n]$ is

$$\vec{A}_{ph,1}[n] = \vec{A}^{(0)}_{ph,1} + \vec{A}^{(1)}_{ph,1} \cdot (n - \tfrac{N_d}{2}) T_s + \vec{A}^{(2)}_{ph,1} \cdot \frac{(n - \frac{N_d}{2})^2 T_s^2}{2} \tag{3.26}$$

$\vec{A}^{(0)}_{ph,1}$, $\vec{A}^{(1)}_{ph,1}$, and $\vec{A}^{(2)}_{ph,1}$ are the static vectors of the fundamental positive sequence, the first, and the second derivative of the static vector, evaluated at point $\frac{N_d}{2}$, respectively. The derivative of (3.26) gives out

$$\vec{A}'_{ph,1}[n] = \vec{A}^{(1)}_{ph,1} + \vec{A}^{(2)}_{ph,1} (n - \tfrac{N_d}{2}) T_s. \tag{3.27}$$

Applying the Gaussian window, the three phasors and their conjugates are evaluated via the weighted least square as

$$\vec{\mathbf{A}} = (\mathbf{B}^{\mathscr{H}} \mathbf{G} \mathbf{B})^{-1} \mathbf{B}^{\mathscr{H}} (\mathbf{G} \cdot \mathscr{C}), \tag{3.28}$$

$$\vec{\mathbf{A}} = [\vec{A}^{(2)}_{ph,1}, \vec{A}^{(1)}_{ph,1}, \vec{A}^{(0)}_{ph,1}, \vec{A}^{*(0)}_{ph,1}, \vec{A}^{*(1)}_{ph,1}, \vec{A}^{*(2)}_{ph,1}]^{\mathscr{T}}, \tag{3.29}$$

$$\mathscr{C} = \left[x_{ph}[0],\ x_{ph}[1],\ x_{ph}[2],\ \cdots,\ x_{ph}[N_d] \right]^{\mathscr{T}}, \tag{3.30}$$

where $\mathbf{B}$ is a constant matrix of size $(N_d + 1) \times 6$ [138], and $\mathscr{C}$ is the cached original waveform samples in the proposed M-Class SEA buffer. $\mathbf{G}$ is the Gaussian weight of length $N_d + 1$. $\mathscr{H}$ is the Hermitian transpose. The operation of Gaussian weighted window and the actual observed data in the buffer is demonstrated in Fig. 3.8.

With $\vec{\mathbf{A}}$ achieved in (3.29), the output of the suggested GWT-M algorithm

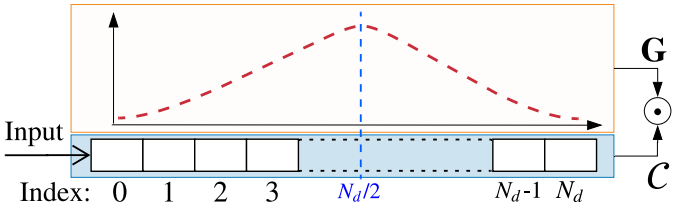

Figure 3.8: The Gaussian window operation and actual observation in the buffer.

can be assessed via (3.31)–(3.34):

$$A_m = |\vec{A}^{(0)}_{ph,1}|, \tag{3.31}$$

$$\Phi_m = \angle\vec{A}^{(0)}_{ph,1}, \tag{3.32}$$

$$F_m = F_N - \Delta f_m, \tag{3.33}$$

$$\text{ROCOF}_m = \frac{-\Delta f_m[n] + \Delta f_m[n-1]}{T_s}, \tag{3.34}$$

$$\Delta f_m = \frac{Im\{\vec{A}^{(1)}_{ph,1} \cdot e^{-j\angle\vec{A}^{(0)}_{ph,1}}\}}{2\pi A_m T_s}. \tag{3.35}$$

At this stage, ΔT can be evaluated in (3.36) and can be directly sent to the QDSC module.

$$\Delta T = \frac{\Delta f_m}{F_N^2 - \Delta f_m F_N} \tag{3.36}$$

As ROCOF from the proposed P-Class and M-Class SEAs is achieved through assessing the frequency derivatives, a low-pass filter (LPF) is needed to smoothen both the ROCOF_m and ROCOF_p estimation during disturbances.

3.5 Numerical Study

This innovative framework for distributed intelligence can be divided into three stages illustrated in Fig. 3.9: (i) online feature extraction and pattern recognition, (ii)real-time event detection and classification, and (iii) adaptive

selection of synchrophasor estimation algorithms (SEAs). The performance of each module is extensively analyzed and numerically investigated under variant conditions in this section.

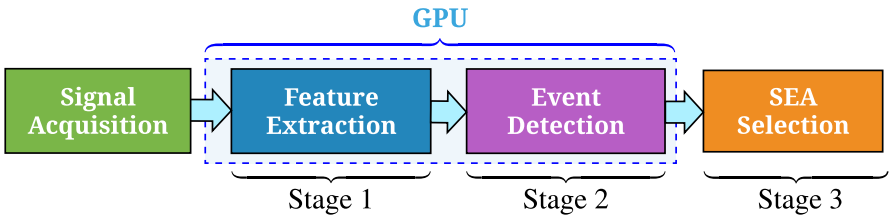

Figure 3.9: Architecture of the proposed analytics within a smart sensor.

3.5.1 Waveform Specifications, Configurations, and Assumptions

All the proposed modules share a sampling rate of 9.6 kHz at power grid nominal frequency of 60 Hz, where up to 50^{th} order (3 kHz) of harmonics is considered in the simulations [25]. According to the Nyquist sampling theorem, the sampling rate used here has a maximum 4.8 kHz coverage as desired. We assumed no congestion during data transfer or Analog to Digital (A2D) conversion. Mathematically, the wavelet transform (WT) should be able to cover the frequency range from 1Hz to 3 kHz; the computing complexity of extracting such a frequency range could be reduced while sufficient feature extraction performance is ensured. In the proposed pseudo-continuous quadrature WT (PCQ-WT) design, we chose the scaling factor a_k ranging from 1 to 256 and in a dyadic dilation manner, i.e., $a_k = 2^i$, wherein the exponent i is equally sampled within $[0, 8]$, i.e., pseudo-continuous. Through this design, the frequency resolution is reduced at the high-frequency range since the harmonics are usually sparse along the spectrum that requires less resolution. Meanwhile, at the low-frequency range including the fundamental frequency, the frequency resolution is enhanced since the 60 Hz waveform is of most interest. When considering the feature exaction

performance (accuracy and speed), we chose the wavelet transform window size of 0.02 second in real-time, and time bins W=192 in (3.6) Section 3.3.2. For simplicity, we use a fixed time shift factor b_k=96.

Table 3.1: Specifications of the Input Test Waveform Parameters

Test Name	Input Range
Signal to Noise Ratio (SNR)*	40dB
Frequency Step	-5Hz to 5Hz
Magnitude Step	0.1–2pu
Phase Step	$\pm\pi/18$ radian
Harmonic Distortion	0.5%–10%THD; order up to 50^{th}
Out-of-Band Interference	10Hz to 120Hz; level 0.01–0.1pu
Amplitude Modulation	0.1Hz to 5Hz; level 0.005–0.1pu
Phase Modulation	0.1Hz to 5Hz; level 0.005–0.1pu
Frequency Ramp	$\pm$0.01Hz/s to $\pm$1Hz/s, within $\pm$5Hz
Single-Line-to-Ground (SLG) Fault***	Magnitude Drop 0.2–1pu
Line-to-Line (LL) Fault***	Magnitude Drop 0.2–1pu**
Line-to-Line-to-Ground (LLG) Fault***	Magnitude Drop 0.1–1pu

*Applied to all test signals.
*Phase shift occurs at faulted lines.
**For $\alpha\beta$ -frame signal only

The specifications of the test power waveforms are selected according to [25, 44] as detailed in Table 3.1. In total, twelve types of waveforms are simulated corresponding to various grid operating conditions: (i) frequency step change, (ii) magnitude step change, (iii) phase step change, (iv) harmonic distortion, (v) out-of-band interference, (vi) amplitude modulation (AM), (vii) phase modulation (PM), (viii) frequency ramp, (ix) single-line-to-ground (SLG) fault, (x) line-to-line (LL) fault, (xi) line-to-line-to-ground (LLG) fault, and normal operating condition. All test waveforms have a Gaussian background noise with 40dB signal to noise ratio (SNR).

3.5.2 Stage One: Feature Extraction

3.5.2.1 Waveform Feature Extraction under Transient Events

Several transient events are simulated and analyzed as follows: the magnitude step (Figs. 3.10a and 3.11a), the frequency step (Figs. 3.10b and 3.11b), and phase step (Figs. 3.10c and 3.11c).

During the magnitude step change event, the intensity/height of the main tune decreases in the scalogram of $\alpha\beta$-frame in Fig. 3.10a and similar behavior can be seen in Fig. 3.11a. However, the low frequency portion (160 to 256) is still discontinuous. Comparing features of the frequency step which are shown in Fig. 3.10b and the phase step in Fig. 3.10c, the patterns emerging during 10ms to 30ms in the $\alpha\beta$-Frame are quite similar, i.e., both of them show a valley in the main tune (highest portion) after 10ms of the events, but the pattern in Fig. 3.10b representing a frequency step change is more intermittent than that in phase step shown in Fig. 3.10c, especially between the scale values from 64 to 128. In contrast, when observing patterns during 15ms to 25ms from the features extracted from the single phase waveform, the differences are obvious; in Fig. 3.11b, the pattern from frequency step change event is symmetric around 20ms, which is 10ms after the time when the event happens; In Fig. 3.11c, the pattern corresponding to the phase step change is disorganized. However, unlike the magnitude step change event, both main tunes (dark red) dim at time $t = 20$ms, which is 10ms after the events occur. One can see that the proposed PCQ-WT pattern recognition algorithm has successfully recognized the unique peculiarities in the signals originated from fast-transient events. Also, the signal signatures have appeared almost immediately as the events happen, making them suitable for online monitoring applications.

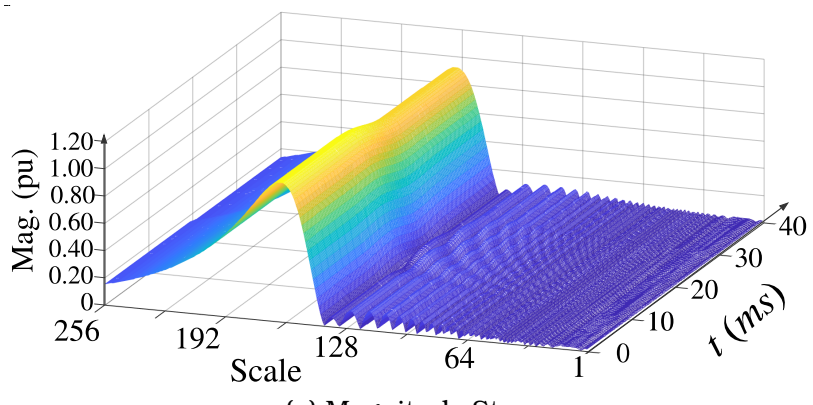

(a) Magnitude Step

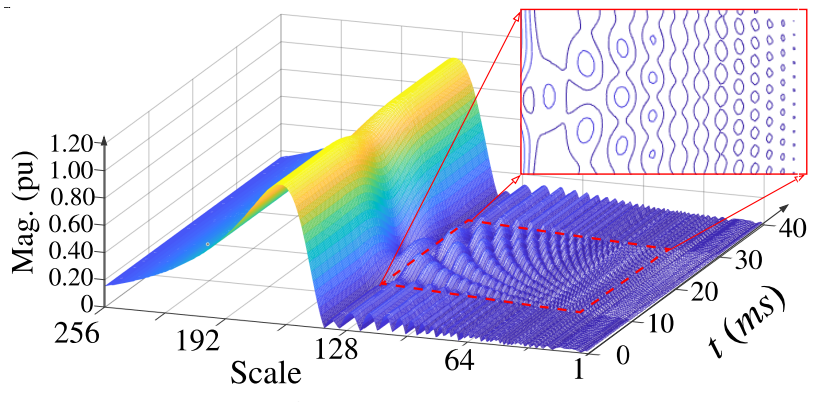

(b) Frequency Step

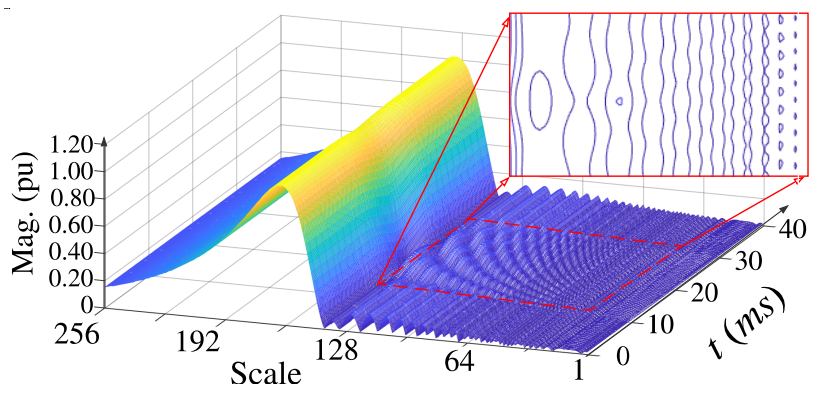

(c) Phase step

Figure 3.10: Extracted features from $\alpha\beta$-frame waveform during fast-dynamic transient events: (a) magnitude step change of 0.2pu at $t = 10ms$; (b) frequency step change of -2Hz at $t = 10ms$; (c) phase step change of -10° at $t = 10ms$.

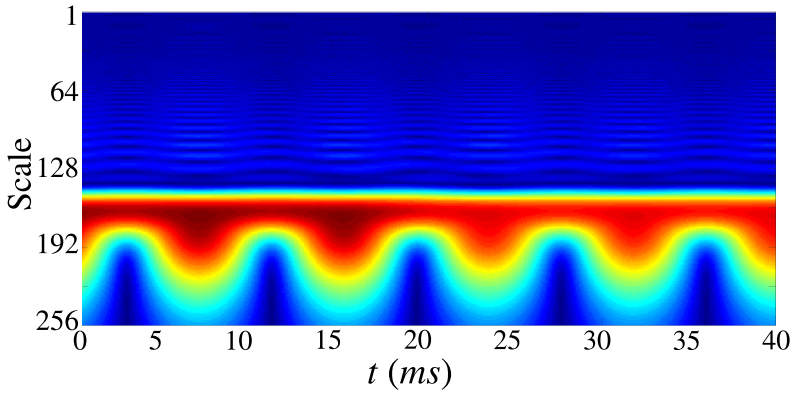

(a) Magnitude Step

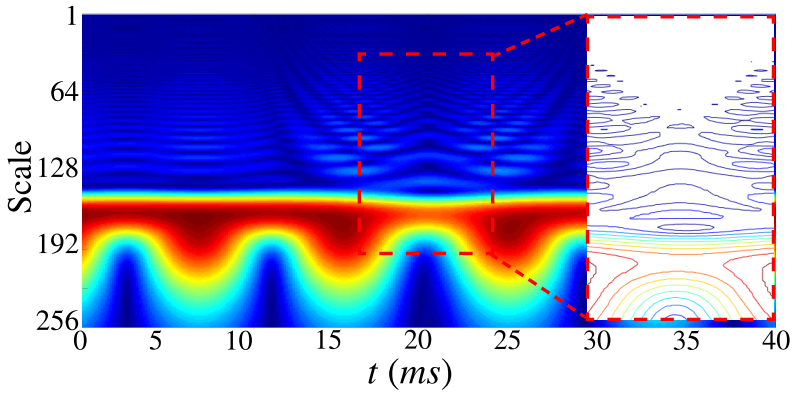

(b) Frequency Step

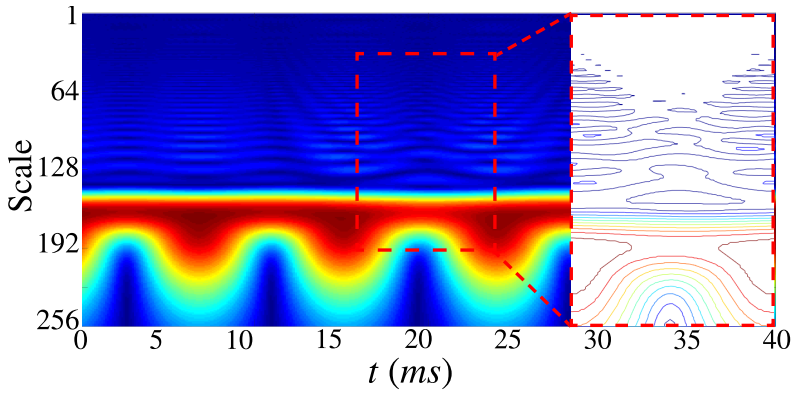

(c) Phase Step

Figure 3.11: Extracted features from simulated single-phase waveforms during fast-dynamic transient events: (a) magnitude step change of 0.2pu at $t = 10ms$; (b) frequency step change of -2Hz at $t = 10ms$; (c) phase step change of -10° at $t = 10ms$.

3.5.2.2 Waveform Feature Extraction under Periodic Events

The following comparisons focus on the emergence of the slow-transient events with periodic impacts on power waveforms. The simulated events include out-of-band interference (Figs. 3.12a and 3.13a), amplitude modulations (Figs. 3.12b and 3.13b), and phase modulations (Figs. 3.12c and 3.13c).

First, during the Out-of-Band inferences—Fig. 3.12a and 3.13a—periodical patterns appeared in the main tune; also the edges (dark gray) of the main tune vary periodically. It should be noticed that the patterns do not have the same frequency as the inference signal's frequency. This behavior is distinguishable from the features extracted from the Amplitude Modulation (Fig. 3.12b) and Angle Modulation (Fig. 3.12c) tests. Focusing on the features obtained from the single phase waveform in Fig. 3.13a, the main tune as well as its edge have gone through some deformations, and this peculiarity has the same frequency as that in Fig. 3.12a.

When comparing the Amplitude Modulation and Angle Modulation tests, the edge of the main tune is flat, but the pattern differences are obvious. In the $\alpha\beta$-Frame, the center of the main tunes (cyan area) of Amplitude Modulation in Fig. 3.12b shows periodical variation over time, and this variation is intermittent with clean edges in the zoomed plot; in contrast, the center of the main tunes Fig. 3.12c corresponding to the Angle Modulation is always continuous. However, both features extracted from Fig. 3.12b and Fig. 3.12c show 5Hz patterns which match the modulation frequency. A similar phenomena can be found when comparing the features extracted from single-phase waveforms. Figure 3.13b shows a discontinuity at the center of the main tune, but in Fig. 3.12c, the main tune is still continuous.

Here, one can see that the proposed PCQ-WT algorithm could suc-

cessfully extract unique features in the waveforms; such patterns convey important information on the underlying slow-dynamic events and provide a foundation based on which machine learning analytics and decision making platforms can operate in real-time.

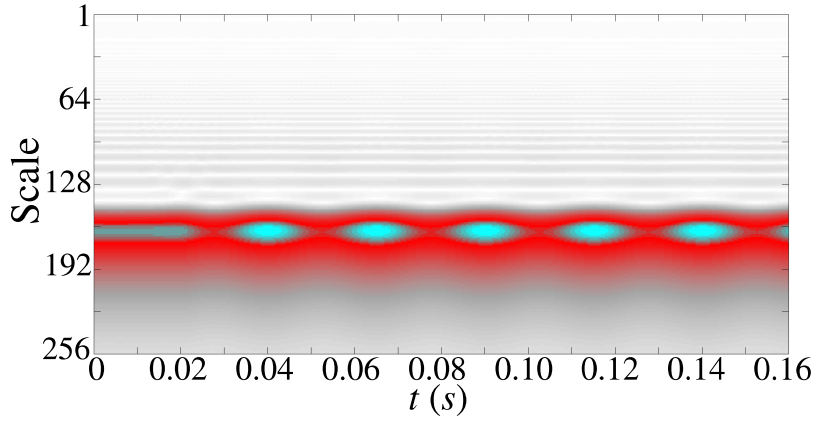

(a) Out-of-Band Interference

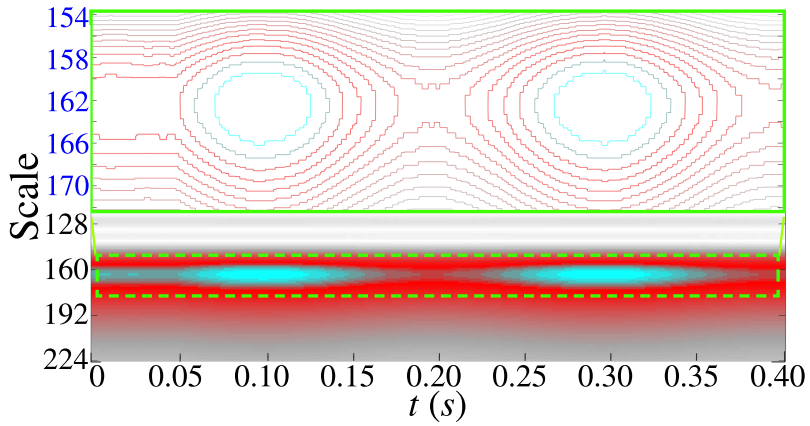

(b) Amplitude Modulation

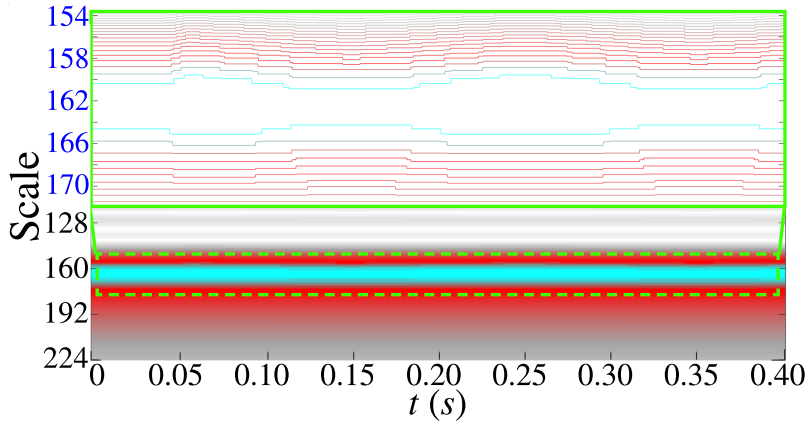

(c) Phase Modulation

Figure 3.12: Extracted features from simulated $\alpha\beta$-frame waveform during slow-dynamic steady-state events: (a) out-of-band interference of 100Hz at $t = 0.01$s; (b) amplitude modulation with magnitude of 0.05pu and frequency of 5Hz at $t = 0.04$s; (c) phase modulation with magnitude of 0.1pu and frequency of 5Hz at $t = 0.04$s.

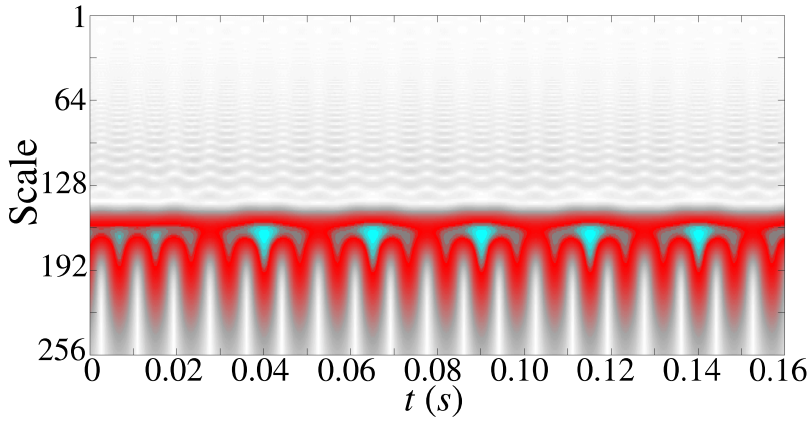

(a) Out-of-Band Interference

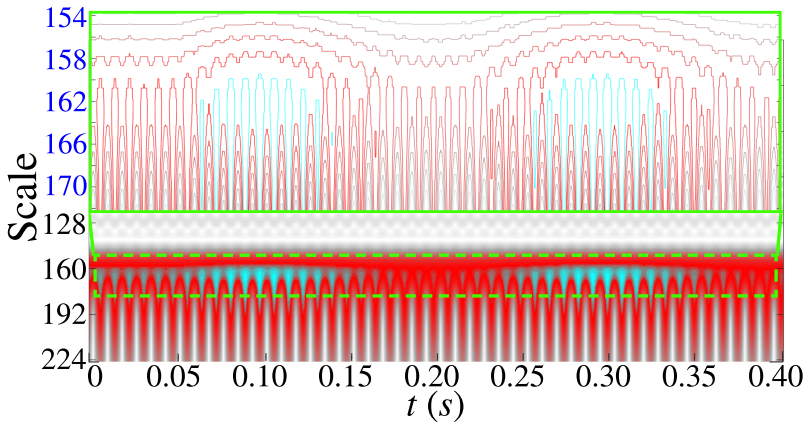

(b) Amplitude Modulation

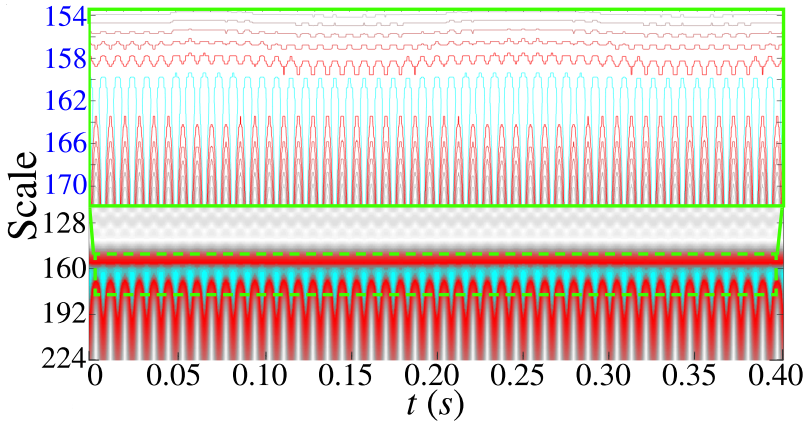

(c) Phase Modulation

Figure 3.13: Extracted features from simulated single-phase waveform during slow-dynamic steady-state events: (a) out-of-band interference of 100Hz at $t = 0.01$s; (b) amplitude modulation with magnitude of 0.05pu and frequency of 5Hz at $t = 0.04$s; (c) phase modulation with magnitude of 0.1pu and frequency of 5Hz at $t = 0.04$s.

3.5.3 Stage Two: Event Detection and Classification

3.5.3.1 Model Configuration

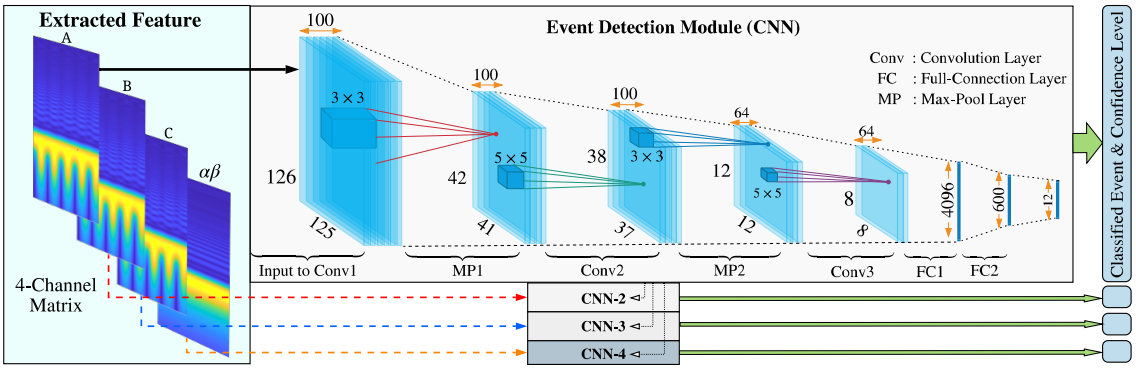

Figure 3.14: Architectural diagram of the proposed CNN configuration with indicated parameters.

The overall framework proposed for online event detection via smart sensors is demonstrated in Fig. 3.14. Our proposed convolutional neural network (CNN) analytics contain three convolutional layers (Conv1, Conv2 and Conv3), two max-pooling layers (MP1 and PM2) and two fully-connected layers (FC1 and FC2) with the following specifications: Input(256×385)–Conv1(100, 5×11)–MP1(3×3)–Conv2(100, 5×5)–MP2(3×3)–Conv3(64, 5×5)–FC1(600×1)–FC2(12×1). Both $\alpha\beta$-frame and single-phase scalograms are fed into the proposed analytics for a duration of 40ms (385 data samples), which is treated as the observation window. Conventional images have homogeneous units on the horizontal and vertical axes, while the scalogram axes carry different information on either time or frequency. A wide kernel (5×11) in Conv1 that can extract more information from the transitions along the time axis is applied. The stride of Conv1 is (2,3), and Conv2 and Conv3 use strides with a size of (1,1). Except for FC1 layer, batch normalization is used in each convolutional and fully connected layers. In Conv3 and FC1, Dropout [139] is used to prevent over-fitting. Rectified

Linear Units (ReLUs) are chosen as the activation function in the neural network. Cross-entropy is used as the loss function. Additional details of the proposed CNN architecture (e.g., the number of convolutional kernels) can be seen in Fig. 3.14; note that there are four CNNs sharing exact same architectures. They, however, need to be trained twice since Phase A, B, and C are symmetric and share one CNN using the same parameters, while the other CNN with different parameters corresponds to the $\alpha\beta$-Frame.

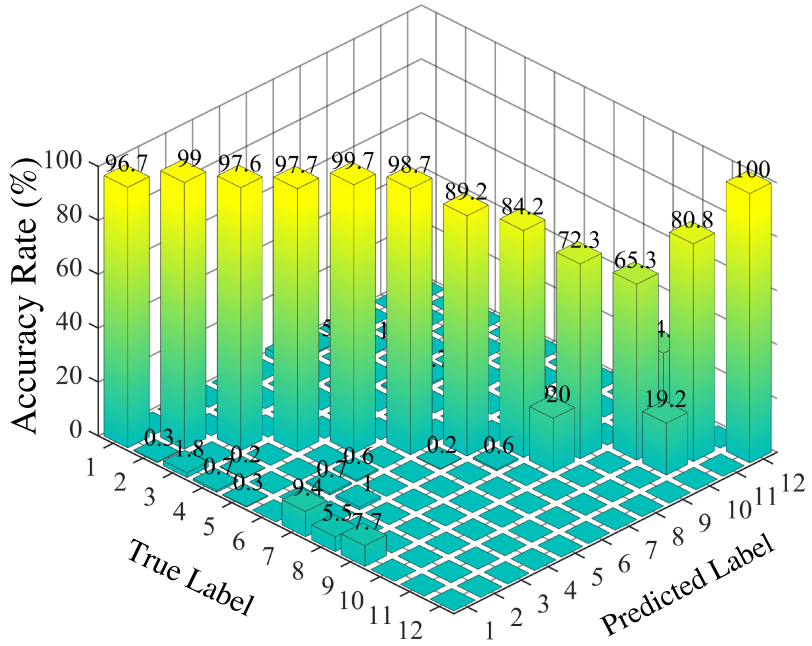

(a) $\alpha\beta$-Frame

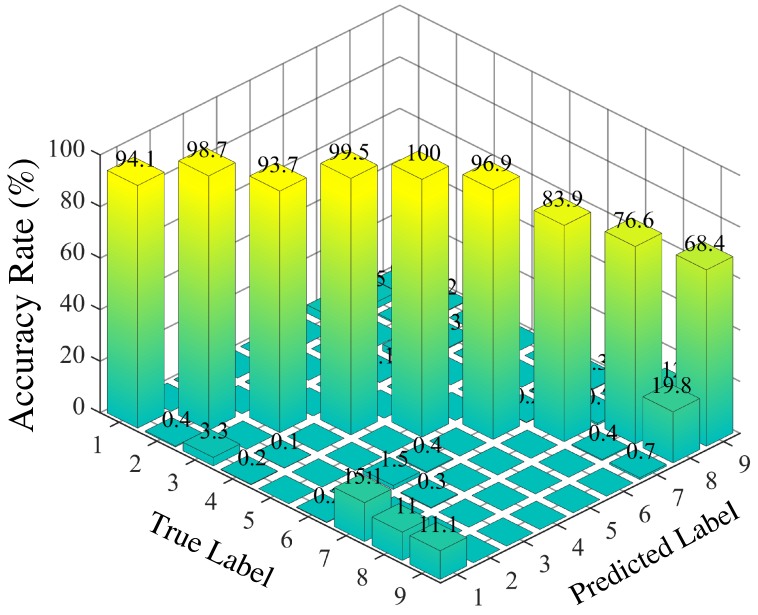

(b) Single Phase

1: Normal	2: Frequency Step	3: Magnitude Step	4: Phase Step	5: Harmonic Distortion	6: Out-of-Band
7: Amplitude Modulation	8: Angle Modulation	9: Frequency Ramp	10: SLG	11: LL	12: LLG

(c) Event Indexing

Figure 3.15: Test results of the proposed CNN engine; detection accuracy is presented in two confusion matrices for the $\alpha\beta$-frame and single-phase waveforms.

In this dissertation, we generated 8,000 samples for each type of event for training the CNNs and another 1,000 samples of each type for validations. In each data sample, only one event occurs at a random time within the 20ms run-time window. The initial phase angle of the waveforms was also randomly selected. During the training process, CNN1, CNN2, and CNN3 are trained using the single-phase scalograms. In order to ensure the maximum information discovery from the scalograms (e.g., during multi-phase events), the proposed event detection engine also utilizes the correlations between three-phase waveforms, which is through processing the $\alpha\beta$-frame scalograms by CNN4. Finally, another 1,000 samples of each event type are generated for blind testing and verifying the event detection accuracy.

3.5.3.2 Offline Event Detection Accuracy

The event detection test results on a variety of events simulated offline are summarized in two confusion matrices presented in Fig. 3.15. The overall detection accuracy of the proposed mechanism using the $\alpha\beta$-frame and single-phase scalograms are found 90.10% and 90.20%, respectively. The “true" label stands for the actual (simulated) test events, and the “predicted" label corresponds to the classification outcome of the proposed CNN modules. For example, one can see in Fig. 3.15(a) $\alpha\beta$-frame detection result, that for a “Frequency Step” event, the *predicted label* matches the *true label* with 99.1% accuracy. This reflects that 99.1% of the 1000 frequency step samples are correctly classified as “Frequency Step".

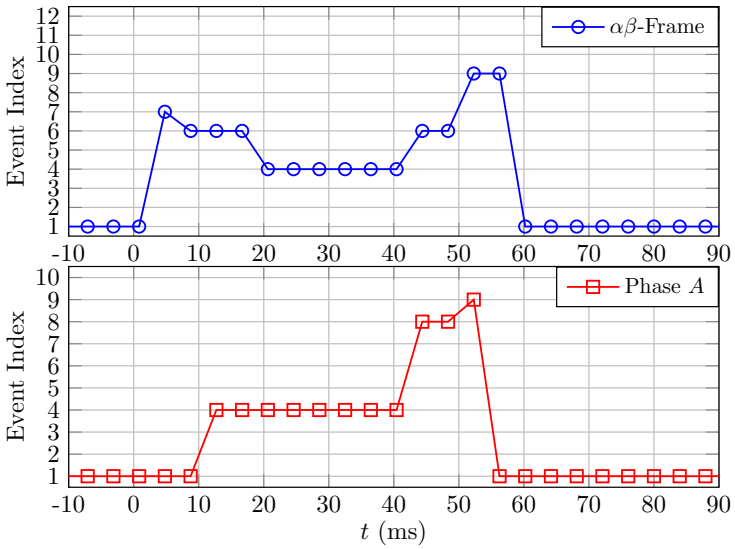

Figure 3.16: Online event classification test results: phase step event occurs at $t = 0$ms; the Event Index is listed in Fig. 3.15(c).

3.5.3.3 Online Event Classification Application

The previous analyses verified the promising accuracy of the proposed event detection scheme. We here conduct an online experiment on the combined feature extraction and event detection mechanisms. Note that the feature extraction module takes approximately 1.20±0.23ms to operate and the event classification engine through CNN takes approximately 1.04±0.31ms to generate the outcome. As the total operation time of the proposed event detection mechanism is 2.24 ± 0.39ms, which is much less than one fundamental cycle of the power grid (16.67ms), the proposed mechanism suites well the real-time event detection applications. We here use synthetic waveforms to test the online classification performance of the proposed analytics. In order to avoid possible congestions, the observation window of the features (40ms duration) is generated every 4ms, which is larger than the combined processing time.

An example classification result on a Phase Step event experiment is demonstrated in Fig. 3.16. The numbers along the Y-axis stand for the

event indexing in Fig. 3.15; the X-axis represents the time in milliseconds. One can see that it took approximately 20ms for the proposed scheme to correctly detect the simulated event using the $\alpha\beta$-channel scalograms, while it only took approximately 12ms to detect the correct event using the Phase A waveforms. It can be also noticed in Fig. 3.16 that an event classification delay and residual do exist. The reason lies in the fact that the event is hard to be classified before the corresponding patterns and signal signatures fully move into the observation window. Similarly, when the patterns start phasing out of the observation window but before they fully vanish, the classification outcome is found unstable. However, such inaccuracies in the output only last for 20ms, i.e., 1.2 fundamental cycles; this delay is still within the desirable limits and acceptable. Meanwhile, it can be seen in all figures in Section 3.5.2 that the center of signal signatures resulted from the fast-dynamic transient events can be observed after 10ms of the occurrence. With a conservative estimation, the fingerprint of the event can be generally revealed and classified after one fundamental cycle (16.67 ms) plus 2.24 ± 0.39ms, which is approximately 20ms. Therefore, the proposed event classification scheme can meet the standard granularity limits [25] and achieves the desired performance requirements for real-time applications.

We also test the proposed framework on a record waveform of duration 0.7s, the result of which is shown in Fig. 3.17. The top heat-map is the event detection results over time, where the confidence rate of the classification is marked with different colors. One should notice that, during *Normal* operating condition, the confidence rate is not very high, but the classification is still correct. Detection errors always exist during the transients between two different events. The *Phase Step* is detected

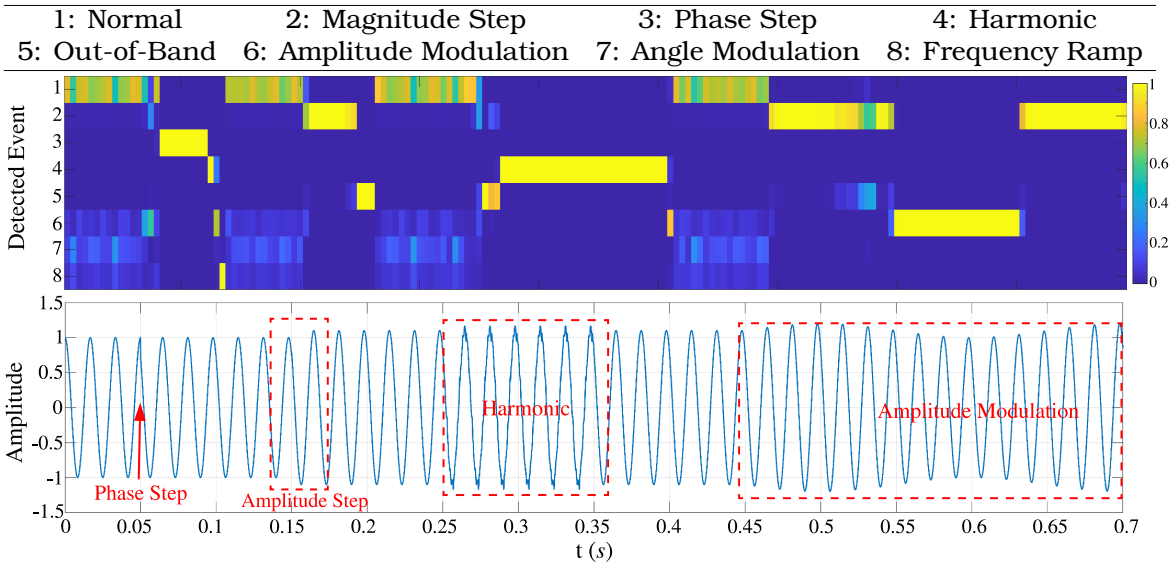

Figure 3.17: Online event detection simulated on a single-phase voltage waveform: detected result (top) and original waveform (bottom).

correctly within 10ms and it takes another 40ms to return back to normal; similar result can be observed for the *Amplitude Step* event. Since *Amplitude Modulation* reveals similar Patterns when compared to the *Amplitude Step* event (bottom plot), the CNN module classified it as the *Amplitude Step*, but when the magnitude starts decreasing, the CNN module shows a low confidence rate in classifying the event as *Amplitude Step* and then selects the event correctly. In order to avoid this miss-classification particularly for slow-dynamic and long-impact events, a wider observation window is recommended, which will compromise the time efficiency in detecting the transient events.

3.5.4 Sensitivity Analysis

3.5.4.1 Pseudo-WT Scaling Factor Redundancy Test

To examine the PCQ-WT's advantages over the conventional WTs, we implement different sets of discrete scaling factors into the modified Gabor

wavelet. All the scaling factors' bases are set to be two, i.e., $a = 2^i$, where i are linearly-increasing real numbers with different step sizes. The conventional WTs use a step size of one in i, i.e., $i = 0, 1, 2, 3....$ In the proposed PCQ-WT, the equivalent step size is 1/32, and the value of i is linearly increasing from 0 to 8. Therefore, in the redundancy test, the values of exponent i are selected in the range of [0, 8] for all WTs to ensure the identical coverage ranges of the maximum and minimum frequencies. Meanwhile, the step sizes of i are 1, 1/2, 1/4, 1/8, 1/16, and 1/32, respectively in each scaling factor redundancy test; thus, the exponents' step sizes of the scaling factors between conventional WT and the proposed PCQ-WT are covered and different feature extraction resolutions are achieved. In order to utilize the same CNN structure in the training process and make the scaling factor's exponents the only variable in the redundancy test, all the generated 2-D scalogram images are reconstructed with 256 pixels along the scale axis by zero-order hold; this is because the lower scaling factors will lead to smaller sizes of scalograms along the scale axis which makes the sizes of the input images for CNN no longer consistent. Similar to Section 3.5.3, and based on Table 3.1, we generated 8,000 samples for each type of event for training the CNN and another 1,000 samples of each event type for validation. Finally, another 1,000 samples of each event type are generated for the blind testing validations.

The redundancy test results using different step sizes in the scaling factor exponents are shown in Figure 3.18 through bar plots. One can see that, by using the conventional WT scaling factors (i with step size one), the event detection accuracy is the lowest in processing both single-phase waveform and $\alpha\beta$-frame waveform scalograms. When using smaller step sizes in i, the accuracy starts increasing. For the single-phase waveform, the accuracy

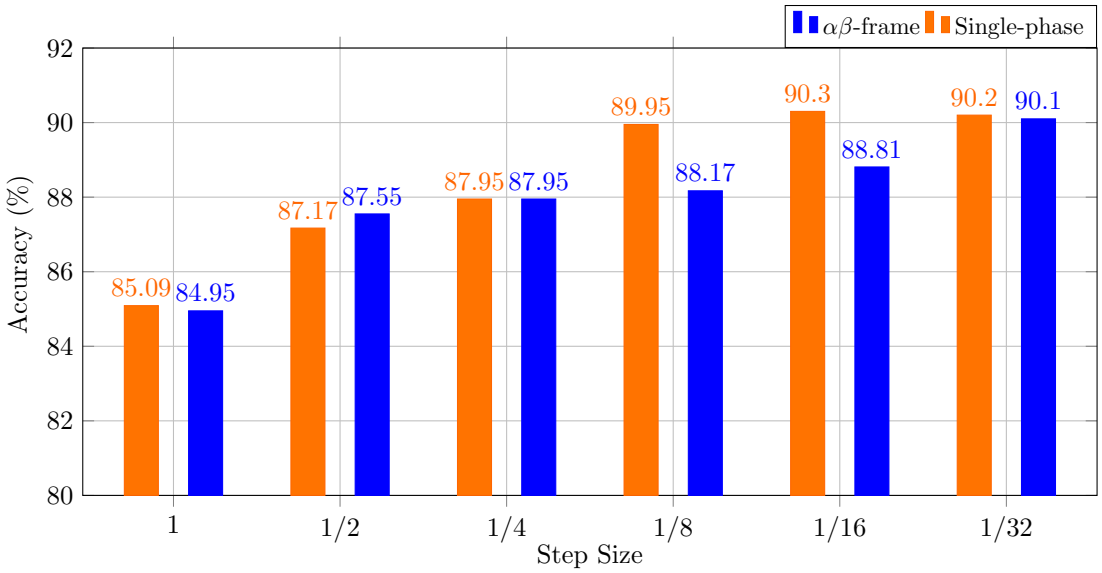

Figure 3.18: Wavelet scaling factor redundancy vs event detection accuracy.

rate becomes stable when the step size is 1/8 or smaller, and decreasing the step size will not improve the accuracy rate significantly. Nevertheless, for $\alpha\beta$-frame, the event detection accuracy from the one using step size of 1/32 (same as the proposed approach) is the highest. Also, one can notice that when using the step size of 1/2, the accuracy improvements are the highest for both single-phase and $\alpha\beta$-frame waveform. Therefore, and according to the above analysis, one can conclude that properly adding redundancy in the scaling factors will increase the feature extraction performance; however, decreasing the step size of the scaling factors would not always benefit the feature extraction performance since the computational complexity will increase as well, due to the additional pixels generated in the scalograms.

3.5.4.2 Background Noise Sensitivity Test

To test the sensitivity of the proposed feature extraction and event detection mechanism to background noise in the sampled waveform, a sensitivity test with white Gaussian noise is performed. The SNR used in the noise

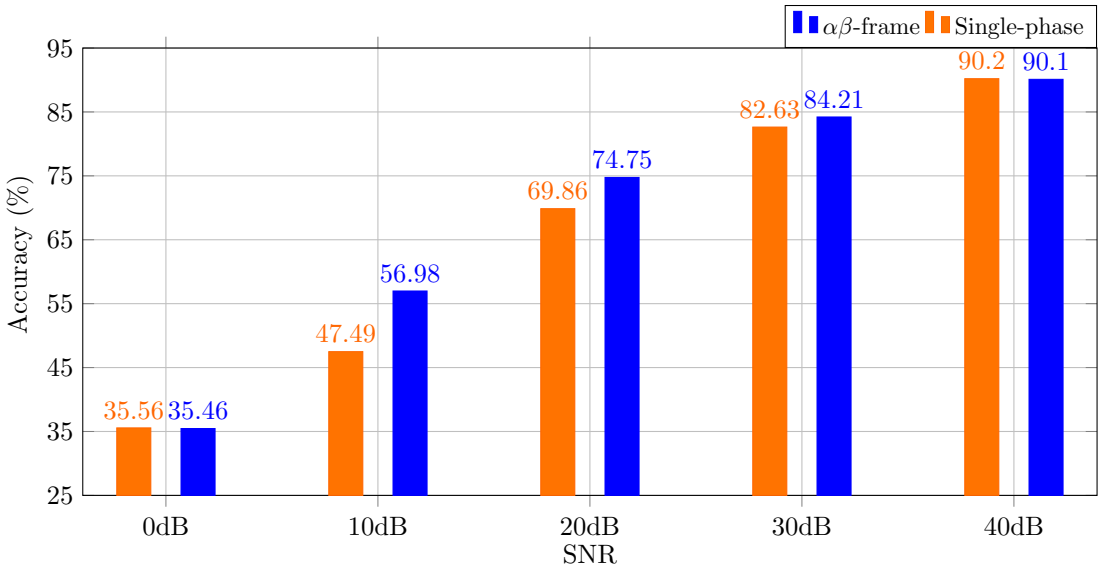

Figure 3.19: Background noise intensity vs event detection accuracy.

sensitivity test are 0dB, 10dB, 20dB, 30dB and 40dB. In this test, the waveform samples of each event type in the training, validation and testing dataset are 8,000, 1,000 and 1,000. All the waveform samples' parameters and settings are selected according to Table 3.1.

The noise sensitivity test results are demonstrated in Figure 3.19. As expected, when the SNR decreases, the event detection accuracy drops for both single-phase and $\alpha\beta$-frame waveform applications. The SNR values for transmission systems are as high as 80 dB to 90 dB, whereas for distribution systems, the values typically range between 40 dB to 80 dB [140]. However, the proposed event detection approach can still provide an accuracy rate above 80% even if the SNR in the waveform is 30dB. This proves that the proposed approach has promising noise resistance capability for monitoring both transmission and distribution systems during dynamic and static operating conditions.

3.5.5 Stage Three: Adaptive SEA Selection

In order to achieve high-fidelity synchrophasor measurements at all times, knowledge on which SEA best suits a certain type of event and a resulting grid operating condition is needed. The proposed framework for adaptive SEA selection could house multiple installed SEAs, the outputs of which could be adaptively selected as needed; we, therefore, integrate several different SEAs in the analyses of this Section as follows. A dynamic Quadrature Delayed Signal Cancellation SEA for high-speed P-Class applications (QDSC-P) and a Gaussian Weighted Taylor Series least square SEA for high-accuracy M-Class applications (GWT-M) are proposed in Section 3.4.4. We also included an "enIpDFT" SEA [33] and a P- and M-Class SEA from [141] which we call the "P&M". We categorized the enIpDFT as a P-Class SEA due to its high response speed verified and reported in [33]. When using the P&M SEA, we denote P&M-P and P&M-M to represent the functionalities corresponding to P-Class and M-Class applications, respectively. The two SEAs are primarily used for performance comparison with our proposed QDSC-P and GWT-M SEAs. The PMU reporting rate of 60 frames/second is here applied with all SEAs sharing the same sampling rate of 9.6kHz.

3.5.5.1 Model Configurations and Parameter Settings

The proposed configuration of the QDSC-P SEA has been introduced in Section 3.4.4.1. The GWT-M SEA possesses a Gaussian window with a length of 4.8 fundamental cycles and the shape factor $\alpha = 3.6$; the enIpDFT SEA is characterized via a Hann window with a length of 3 fundamental cycle—the same as that utilized in [33]. The P&M-P and P&M-M SEAs use a Kaiser window of length 3.8 and 5.8 fundamental cycles, respectively [141].

Since the evaluation of the Rate of Change of Frequency (ROCOF) is performed through the derivative of frequency by time, filtering the noise and the distortion by higher-order low-pass filters (LPF) can significantly reduce the ROCOF error (RFE). This, in turn, results in a slower ROCOF measurement. In order to ensure a fair performance comparison of different SEAs when assessing ROCOF, an LPF with the following transfer function is applied when needed:

$$h(z) = \frac{0.0968z + 0.0968}{z - 0.8063}, \tag{3.37}$$

This applied setting ensures an acceptable dynamic response speed within the maximum RFE limits as enforced in [25].

3.5.5.2 Steady-State Compliance Tests

Frequency Sweeping Test Results: We conduct a frequency sweeping test for the signal frequency to change ranging from 55Hz to 65Hz as required by the IEEE standard [25] for both P-Class and M-Class SEAs. The maximum Total Vector Errors (TVEs) for all SEAs within the proposed sensor technology are assessed and demonstrated in Fig. 3.20a, from which one can see that the outputs from all SEAs result in TVE measures less than 1%, except for the enIpDFT (solid green line): when the frequency is less than 57.5Hz, the TVE exceeds the 1% threshold.

For the P-Class SEAs, the Frequency Error (FE) limit is set to 10mHz according to [25]. The proposed QDSC-P (dashed blue line) in Fig. 3.20b is observed to reach its maximum FE ($\pm$5mHz) at f=55Hz. For the enIpDFT SEA, the FE stays within the limit only when f is around the nominal frequency and it quickly exceeds the 5mHz limit when $f \leq$ 59.7Hz and $f \geq$

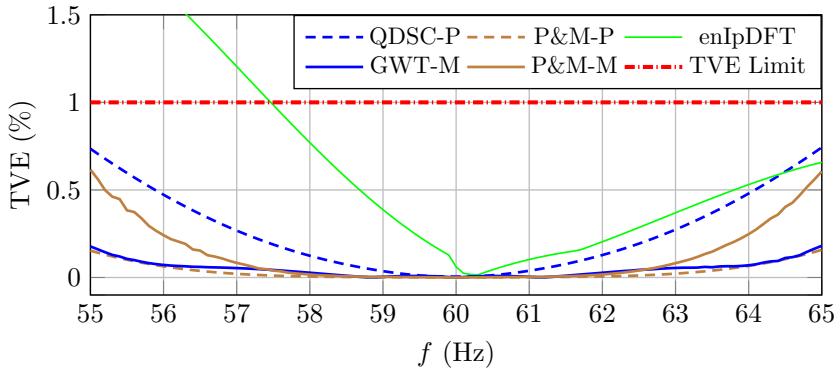

(a) TVE

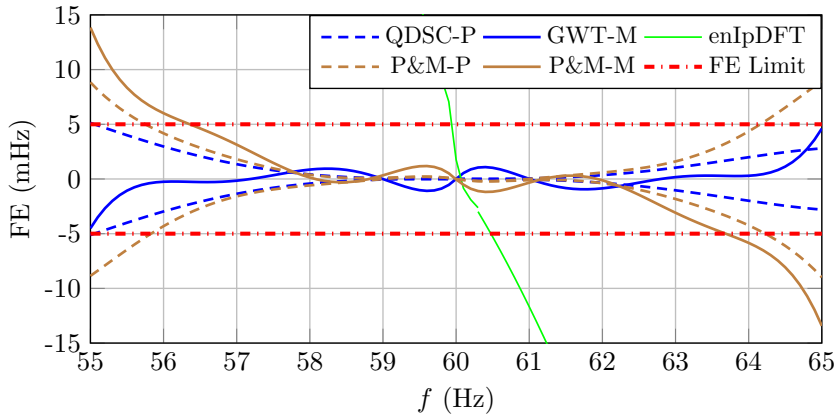

(b) FE

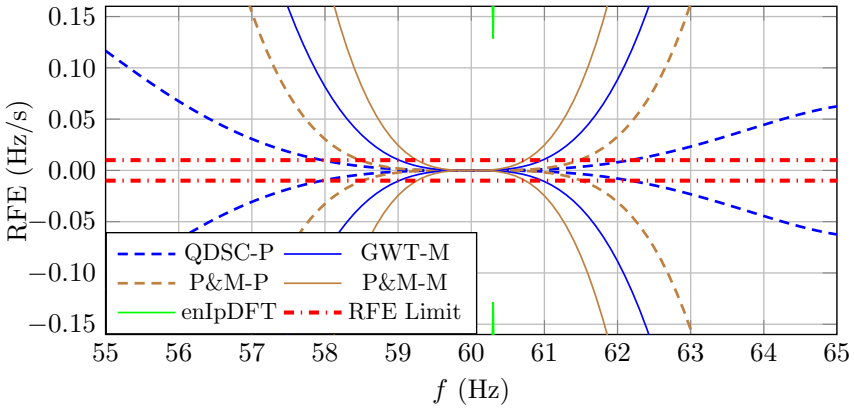

(c) RFE

Figure 3.20: Performance evaluation of different SEAs under Frequency Sweeping tests.

60.9Hz; therefore, the FE results in Fig. 3.20b reveal that the P-Class enIpDFT SEA fails the conducted tests in the required frequency range from 58Hz to 62Hz. When focused on FE, the results demonstrate that the proposed QDSC-P outperforms the other two SEAs. The P&M-P SEA (dashed brown line) stays within the limits when the off-nominal frequency is beyond $\pm$4.15Hz, which satisfies the standard requirement. In the M-Class FE plot of Fig. 3.20b, our proposed GWT-M SEA (solid blue line) stays within the M-Class FE limit (5mHz) when f is in the designated range, but the P&M-M fails when $f >$ 63.6Hz or $f <$ 56.3Hz.

Figure 3.20c illustrates the RFE performance comparison of the integrated SEAs within the smart sensor. One can see from the test numerical results that only the proposed QDSC-P SEA satisfies the P-Class standard requirement (RFE $\leq$ 0.01Hz/s) at the frequency range from 58Hz to 62Hz. The RFE corresponding to the P&M-P SEA exceeds the desired limit when $f >$ 61.5Hz or $f <$ 58.5Hz; additionally, the reported RFE for the enIpDFT SEA fails the compliance thresholds in the entire frequency range tested, where its minimum RFE is found 0.13Hz/s at f=60.2 Hz. For the other two M-Class SEAs, both the proposed GWT-M and P&M-M fail to meet the standard requirements, as the corresponding RFEs quickly exceed the limit when the off-nominal frequency is 0.7Hz and 1.0Hz, respectively. However, the proposed GWT-M SEA performs better than the P&M-M SEA, as the former can tolerate a wider off-nominal frequency range.

Modulation Test Results The modulation tests need to be considered in two scenarios: Amplitude Modulation (AM) and Phase modulation (PM).

- ***Amplitude Modulation Tests:*** Through the AM test results presented in Table 3.2, one can see that all the integrated SEAs within the

developed smart sensor solution meet the standard requirements, except the enIpDFT; the P&M-P SEA and the proposed GWT-M SEA reveal the best performance for the P-Class and M-Class measurements, respectively, under AM conditions.

- ***Phase Modulation Tests:*** The performance of all integrated SEAs during the PM tests is listed in Table 3.3. Among the P-Class SEAs, the P&M-P provides the lowest TVE, while our proposed QDSC-P reveals the best performance when targeting FE and RFE measures. The enIpDFT SEA fails the PM tests as the corresponding FE (marked in yellow) exceeds the standard limit of 60mHz [44]. Among the M-Class SEAs, both GWT-M and P&M-M meet the standard requirements, but the proposed GWT-M SEA shows a better performance during the PM tests; it could, hence, be a promising candidate for synchrophasor measurement during such incidents.

Table 3.2: Amplitude Modulation (AM) Test Results

P-Class Maximum Error			
	TVE (%)	FE (mHz)	RFE (Hz/s)
Max Limit	3%	60	3
QDSC-P	1.950%	8	0.193
P&M-P	0.017%	1	0.031
enIpDFT	7.850%	69	8.090
M-Class Maximum Error			
Max Limit	3%	300	15
GWT-M	0.019 %	0.17	0.120
P&M-M	0.068 %	0.40	0.264

Harmonic Distortion and Out-of-band Interference Tests: The performance of different SEAs under slow-dynamic steady-state tests of harmonic

Table 3.3: Phase Modulation (PM) Test Results

P-Class Maximum Error			
	TVE (%)	FE (mHz)	RFE (Hz/s)
Max Limit	3%	60	3
QDSC-P	1.915%	0.6	0.019
P&M-P	0.017%	0.7	0.031
enIpDFT	7.850%	68	8.093
M-Class Maximum Error			
Max Limit	3%	300	30
GWT- M	0.018 %	0.2	0.119
P&M-M	0.068 %	0.4	0.264

distortion and out-of-band interference are illustrated in Table 3.4 and Table 3.5, respectively. During a harmonic distortion event, the proposed QDSC-P SEA results in the lowest TVE, FE and RFE indicators when compared to other SEAs. It is worth noting that although the RFE results (marked in yellow) corresponding to the P&M-P and enIpDFT SEAs exceed the designated standard limit, the problem could be solved by using a higher-order LPF but at the cost of a slower dynamic-response speed. A similar observation can be made from the results presented in Table 3.5. As one can see, the maximum RFE indicator (marked in yellow) corresponding to the GWT-M and P&M-M SEAs are in the same order of magnitude, and they are larger than the prescribed limits; such violating RFEs can be also mitigated by applying an LPF.

3.5.5.3 Dynamic Compliance Tests

We here test and evaluate the dynamic response performance of various SEAs in order to verify their compliance with the standard requirements [25].

Frequency Ramp Test Results: In this test, a frequency ramp rate of $\pm$ 1Hz/s is applied to the waveforms fed into the smart sensor solution. The

Table 3.4: Harmonic Distortion Test Results

P-Class Maximum Error			
	TVE (%)	FE (mHz)	RFE (Hz/s)
Max Limit	1%	5	0.01
QDSC-P	0.005%	0.31	0.004
P&M-P	0.014%	1.75	0.398
enIpDFT	0.061%	-3.75	4.184
M-Class Maximum Error			
Max Limit	1%	25	6
GWT-M	0.003 %	0.19	0.333
P&M-M	0.003 %	0.32	0.468

Table 3.5: Out-of-band Interference Test Results

M-Class Maximum Error*			
	TVE (%)	FE (mHz)	RFE (Hz/s)
Max Limit	1.3%	10	0.1
GWT-M	0.011 %	0.02	0.562
P&M-M	0.005 %	0.04	0.875

*: No requirement for P Class

TVE results indicating the performance of different SEAs in response to the ramp test are presented in Fig. 3.21a. One can see that the enIpDFT SEA fails to meet the standard requirements, while the remaining SEAs are observed in full compliance. Figure 3.21b and 3.21c compare the FE indicators when evaluating the performance of different SEAs under the frequency ramp test. The proposed QDSC-P and GWT-M SEAs along with the P&M-P all continuously meet the standard requirements, while the P&M-M SEA is in compliance only when $56.5\text{Hz} \leq f \leq 63.5\text{Hz}$. The enIpDFT SEA constantly fails the frequency ramp test; as illustrated in Fig. 3.21d, the RFE results for the enIpDFT SEA remains always beyond the standard limits. Both QDSC-P and P&M-P SEAs meet the standard RFE threshold in the range of $56.5\text{Hz} \leq f \leq 63.5\text{Hz}$. Evaluating the RFE indicator, one can

see in Fig. 3.21e that both M-Class SEAs fail the frequency ramp test. The GWT-M SEA can only comply with the standard requirements within the 58Hz $\leq f \leq$ 62Hz, while this is valid for the P&M-M SEA in a narrower range of 58.5 Hz $\leq f \leq$ 61.5 Hz. It is worth noting that the proposed QDSC-P SEA can tolerate larger off-nominal frequencies (i.e., lower RFE when f is close to 55Hz) and is able to function as an M-Class SEA to evaluate ROCOF. This can be achieved by tuning its LPF at the very minimal cost of the algorithm's response speed.

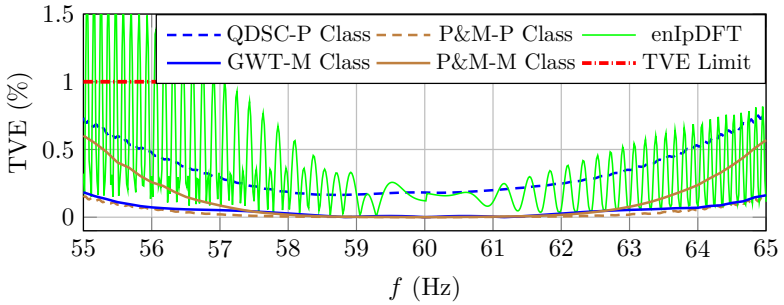

(a) TVE

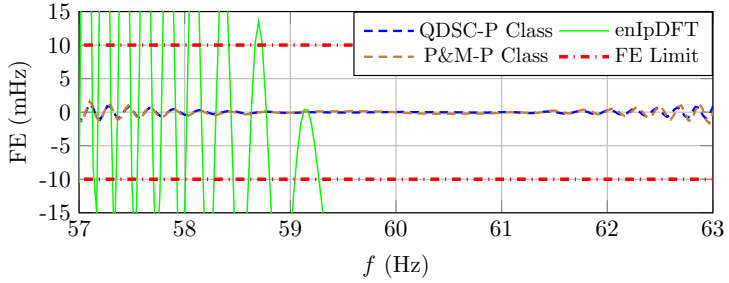

(b) P-Class FE

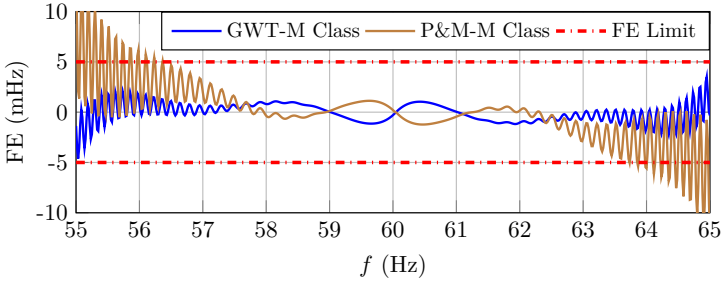

(c) M-Class FE

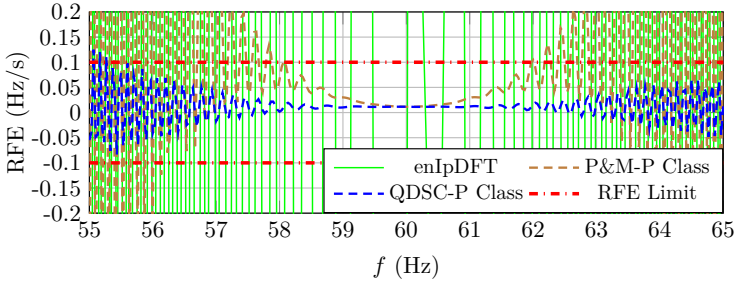

(d) P-Class RFE

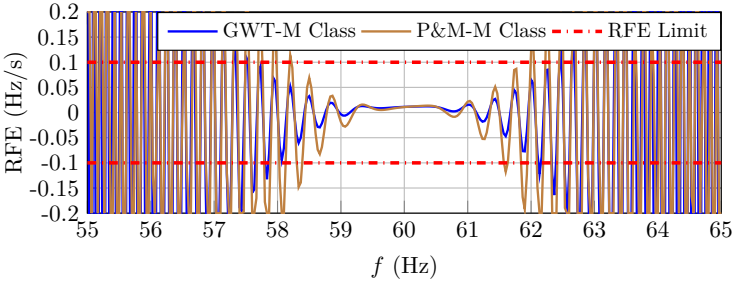

(e) M-Class RFE

Figure 3.21: Performance evaluation of different SEAs under Frequency Ramp tests.

Step Change Test Results We here evaluate the dynamic response of different SEAs in response to the input magnitude and phase step change events.

- ***Magnitude Step Tests:*** One can see in Fig. 3.22a that the TVE indicator corresponding to the QDSC-P SEA offers the fastest convergence speed (13ms) when the magnitude step of 0.1pu occurs. The P&M-P SEA takes 40ms to return below the limit (which is more than two times of that for the QDSC-P SEA) and fails to meet the standard requirement of $1.7/f_0$=28.3ms. Both M-Class SEAs achieve the standard compliance requirement of the TVE response time limit (79ms). Figure 3.22b illustrates the FE comparisons of different SEAs. The enIpDFT SEA is found the fastest (taking only 46ms) to return below the desired FE limit, while this time is 60ms and 82ms for the P&M-P and QDSC-P SEAs, respectively. Unfortunately, both QDSC-P and P&M-P SEAs take longer than the desired $3.5/f_0$=58.3ms response time limit. The GWT-M SEA takes 70ms and the P&M-M SEA takes 85ms to converge, which are within the 120ms prescribed response time limit in [25]. With a focus on the RFE indicator, the enIpDFT SEA fails to meet the standard requirement and, hence, is not included in the results presented in Fig. 3.22c. The QDSC-P SEA fails the magnitude step test as it violates the P-Class RFE response time limit ($4/f_0$=66.6ms). Since removing the LPF would not improve the ROCOF response speed of the QDSC-P SEA, it is concluded not suitable for ROCOF measurements particularly during dynamic test conditions. The P&M-P SEA takes 63ms to return back to the RFE limit which satisfies the standard response time requirement. Compared to the GWT-M SEA, the P&M-M SEA shows the slowest RFE convergence speed, but is still within the

129ms M-Class response time limit under dynamic test conditions. Hence, the proposed GWT-M SEA is concluded as the most promising candidate for M-Class ROCOF measurements.

- ***Phase Step Tests:*** According to the results presented in Fig. 3.23a, none of the integrated P-Class SEAs meet the standard TVE response time limit of 28.3ms under phase step test events. Amongst, the P&M-P SEA takes the shortest time (42ms), followed by the enIpDFT (43ms) and QDSC-P (52ms) SEAs. In contrast, both M-Class SEAs meet the TVE response time requirement of 79ms. The proposed M-Class GWT-M takes the shortest time (50ms) to return below the desired limit when a phase step change occurs, while P&M-M SEA takes the longest time (63ms) to converge. It is found, in Fig. 3.23b, that the enIpDFT SEA is the fastest (46ms) to converge and satisfy the P-Class FE response time limit (58.3ms). While the proposed QDSC-P and P&M-P SEAs take, respectively, 120ms and 60ms, they both fail to meet the standard FE response time requirement. The FE indicators reported for the two M-Class SEAs comply with the standard requirements. The RFE results for different SEAs in responding to a phase step event are compared in Fig. 3.23c. The P&M-P SEA still complies with the RFE response time requirement for P-Class ROCOF measurements, while the QDSC-P SEA fails to achieve so. The RFE results for the M-Class SEAs reveal that the proposed GWT-M outperforms P&M-M when comparing the converging speed.

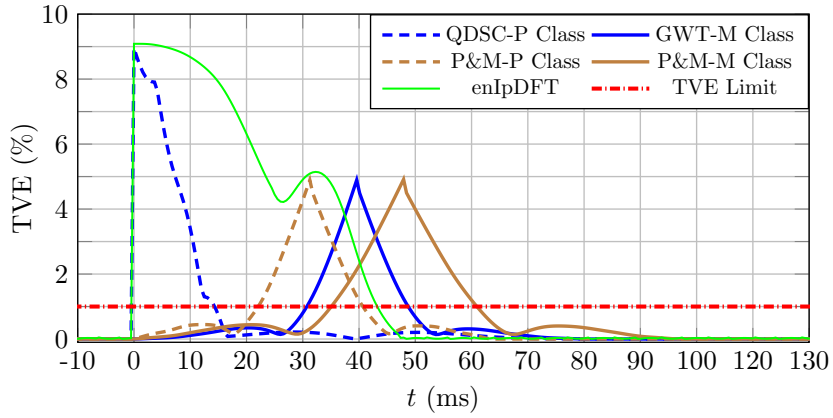

(a) TVE

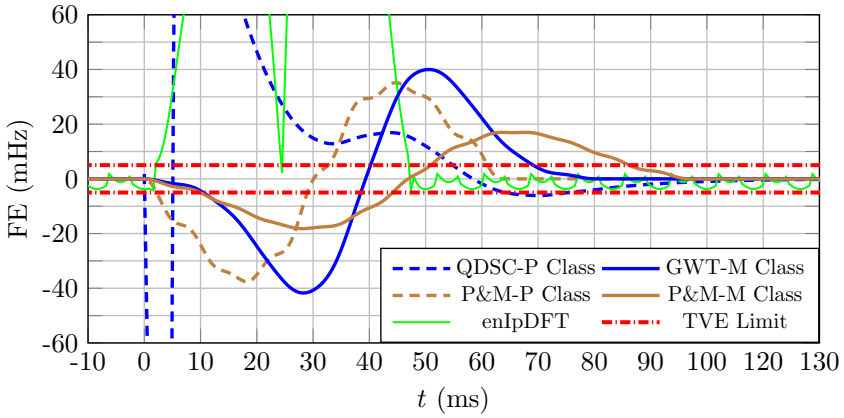

(b) FE

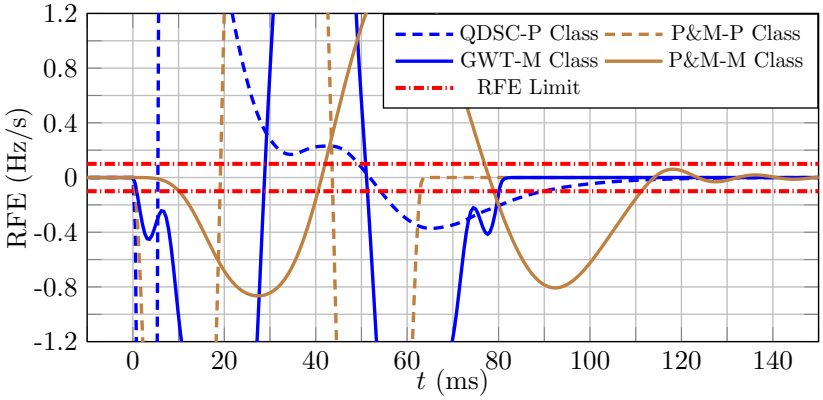

(c) RFE

Figure 3.22: Performance evaluation of different SEAs under Magnitude Step test of 0.1pu.

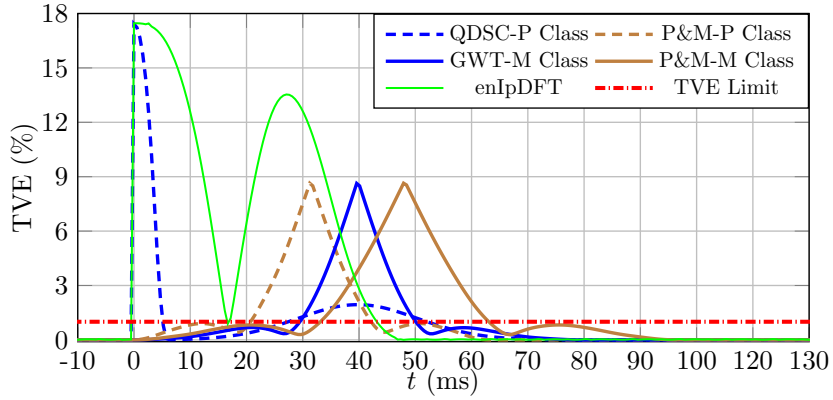

(a) TVE

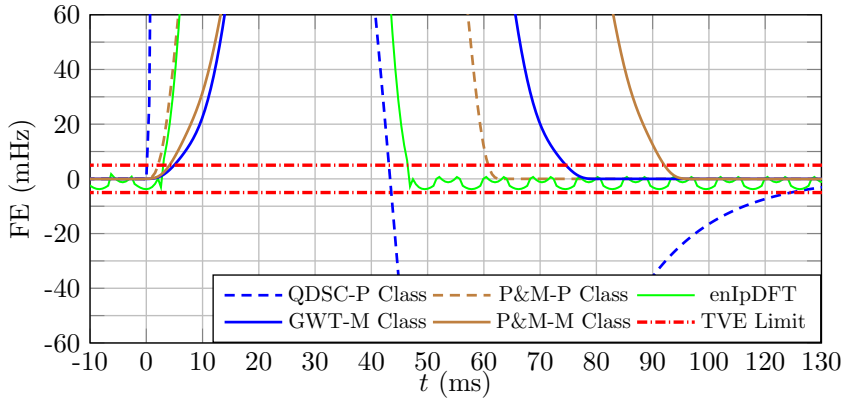

(b) FE

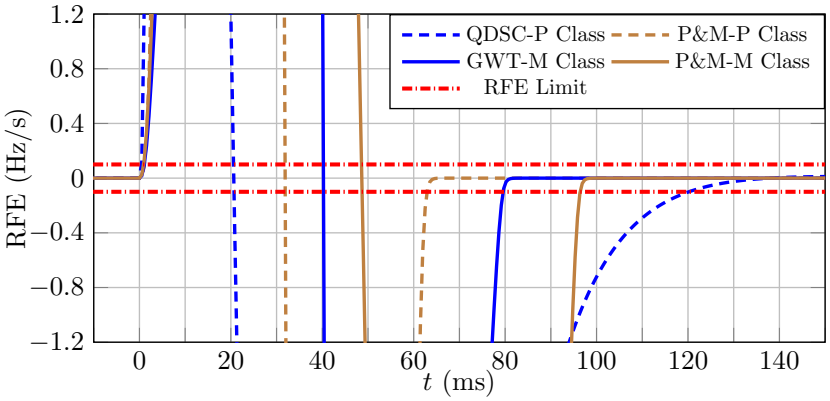

(c) REF

Figure 3.23: Performance evaluation of different SEAs under Phase Step test of $\pi/18$.

3.5.5.4 Adaptive SEA Selection Mechanism

Table 3.6: Best-Fit SEAs for Phasor Measurement under Different Test Scenarios and Operating Conditions

	C†	Phasor	Frequency	ROCOF
Abnormal Frequency	P	P&M-P	QDSC-P	
	M	GWT-M		
Harmonic Distortion	P	QDSC-P		
	M	GWT-M		
Out-of-Band Interference	M	P&M-M	GWT-M	
Phase Modulation	P	P&M-P	QDSC-P	
	M	GWT-M		
Amplitude Modulation	P	P&M-P		
	M	GWT-M		
Frequency Ramp	P	P&M-P	QDSC-P	
	M	GWT-M		
Magnitude Step	P	QDSC-P	enIpDFT	P&M-P
	M	GWT-M		
Phase Step	P	P&M-P	enIpDFT	P&M-P
	M	GWT-M		

†: PMU Class.

We have examined and analyzed the performance of various SEAs within the proposed smart sensor solution. The test results verified a fact that different SEAs perform differently under various test scenarios and simulated operating conditions. Our approach to synchrophasor measurement is, hence, adaptive in that only the best-fit SEAs are activated at any time instant, thereby ensuring high-fidelity measurements. The results are demonstrated in Table 3.6, offering a holistic view on the performance and advantage of each SEA with regards to different performance metrics of interest. The results presented in this table can be employed as a mechanism for adaptive SEA selection in response to a detected event. Meanwhile,

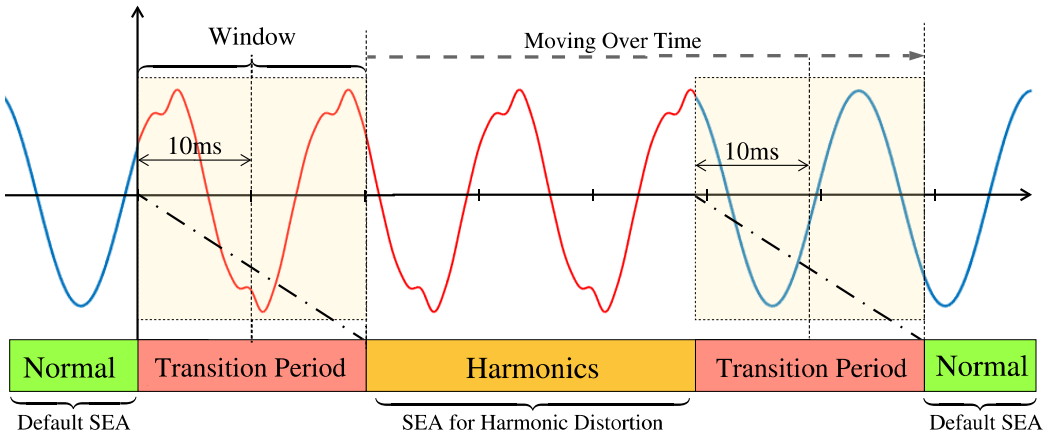

Figure 3.24: An example of the online event classification (Stage 2) jointly with the SEA selection (Stage 3) during a harmonic distortion event.

one can see in Table 3.6 that the proposed QDSC-P and GWT-M SEAs are selected in more than 70% (i.e., 33 out of 45) of scenarios, which verifies their effectiveness in improving the synchrophasor measurements. Moreover, the tests conducted in Section 3.5.3 verified that the proposed adaptive SEA selection mechanism can ensure the desired accuracy and speed requirements of different end-use applications that utilize the synchrophasor measurements. Note that the proposed adaptive mechanism is generic enough to accommodate other SEAs that are not investigated here but of interest to the user.

3.5.5.5 Demonstration of An Integrated Application

An example integration of the suggested SEA selection mechanism in conjunction with the event detection and classification modules is demonstrated in Fig. 3.24. With the occurrence of a simulated harmonic distortion event in the waveforms and following a transition period of maximum 20ms (as marked in red), the SEA selection mechanism selects the best-fit SEA to achieve the high-fidelity measurements under the detected event. When

the harmonic distortion event disappears and the corresponding waveforms return back to normal, it will take a maximum of 20ms to switch back to the SEA most suitable for measurement during normal operating conditions in the grid. Therefore, an awareness on the performance of the installed SEAs is crucial for the successful functioning of the proposed sensor technology. An investigation on the performance of different SEAs within a smart sensor was presented earlier in Section 3.5.5.1-3.

3.6 Conclusion

The chapter presented innovative data-driven analytics embedded in a smart sensor solution technology; the proposed solution transforms the existing centralized monitoring and control paradigms to distributed intelligence for online situational awareness in power grids. Furthermore, the proposed smart sensor is housed with an adaptive SEA selection mechanism, a framework that ensures high-fidelity synchrophasor measurements at all times. Various stages of the presented technology were numerically analyzed and verified: online feature extraction and pattern recognition, real-time low-latency event detection and classification, and adaptive measurements. Through extensive testing and analyses, it was concluded that (i) the proposed event detection and classification scheme using machine learning analytics could provide real-time, accurate, and informative guidelines on the ongoing operating conditions in power grids, thereby facilitating active and automatic control actions in response; (ii) different SEAs perform differently under different events and operating conditions in the grid. With the knowledge on the performance of different embedded P-Class and M-Class SEAs under different grid operating conditions, the best-fit SEA outputs would be selected in an automated manner for high-fidelity measurements.

Chapter 4: Smart Sensor Technology for High-Impedance Fault (HIF) Detection

4.1 Abstract

Accidents caused by faults on overhead power lines have been more frequently reported under extreme weather conditions and may strongly threaten the safety and stability of the power grids, e.g., massive wildfires caused by the electrical arcs or lines getting in touch with vegetation, relay miss-operations, etc. It has been widely recognized that the electric safety concerns engendered by overhead line faults have to be timely and properly addressed to minimize the subsequent risks and damages. However, the existing monitoring devices and protective relays can barely detect high impedance faults (HIFs) and are unable to warn the system operators until serious abnormalities or damages are observed. To further investigate this smart sensor concept in this specific high-level event detection application and meet the urgent and yet challenging demand of a fast and accurate detection of HIFs, a modified core detection engine is developed and implemented to detect HIF events in the distribution systems.

In this Chapter, the background information on and existing modeling methods for the HIF event are first presented in Section 4.2. Then, an improved HIF model and the work flow of the modified HIF event detection engine are introduced in Section 4.4 and Section 4.3. The detailed technology and configuration of the proposed HIF detection approach is presented in Section 4.5 and tested under a variety of simulated conditions in Section 4.6. The numerical results demonstrate its efficacy and superiority over the state-of-the-art advancements.

4.2 Background of High Impedance Fault

One safety-threatening disruption in power systems is recognized as High Impedance Faults (HIF), the detection of which has long remained a challenging concern in the electric industry. HIFs can cause "arcs" or "flash-over" from the wires, through the air, to the neighboring trees, other vegetation or equipment, where it can cause fires, injuries, or even fatalities [142]. A life-threatening example is the constant exposure and contact of a power line with a tree branch during high-wind conditions, which can threaten homes in residential neighborhoods and spark wildfires in rural areas. Such types of faults are commonly caused by undesired contacts with bare energized electrical conductive parts, the high-impedance nature of which significantly restricts the flow of fault current to a level hard to be detected by the overcurrent protective relays [143]. Also, the existing commercial microprocessor-based protective relays activate a tripping decision when the electrical measurements are observed well beyond the detection threshold; however, an unsatisfactory performance is observed in their detection logic when facing the HIF events. Electrical safety studies have shown that conventional protection schemes detected and cleared only 17.5% of staged HIFs [2, 3, 144]. Therefore, HIF detection and localization in electrical power systems yet remain a safety-threatening challenge for power system protection engineers, a fast and accurate solution to which is urgently needed to limit the safety risks, prevent power grid operation violations, and save human lives [145].

Many research works have been conducted in diagnosing HIFs, each with some advantages and disadvantages; reference [146] harnessed the high-frequency content in real vegetation fault signatures and proposed a

method for the detection of distinct and very small-current HIFs. In [147], an HIF detection approach for power distribution networks is suggested using fuzzy logic control that evaluates the 3rd and 5th harmonics in the electrical current signals. However, due to the different HIFs characteristics compounded by the existence of harmonics and noises in the power waveforms, their accuracy and speed performance may be compromised in real-world scenarios. A scheme to detect HIFs using the Time-Time (TT) transform that analyzes and determines the fault wave patterns is introduced in [148]; this scheme can handle low signal to noise ratio (SNR) in power waveforms through a threshold selection procedure using unscented transformation (UT). While it can be applied to microgrids with different ratings and structures, the detection threshold must be tailor-made and adjusted appropriately. Reference [149] presented a variable-importance-based feature selection method to identify HIFs from a large pool of signal signatures; this feature selection scheme utilizes the discrete Fourier transform (DFT) and Kalman Filter (KF) for harmonics coefficient estimation and HIF duration and magnitude measurement.

With the rapid advancements in Artificial Intelligence (AI), many researchers have implemented various HIF detection techniques through a variety of machine learning technologies. References [142, 150, 151] utilized waveform pattern analysis and Support Vector Machine (SVM) to classify and ultimately detect HIFs in power grids. In [3], semi-supervised learning and probabilistic learning are used for HIF detection and localization, revealing promising detection accuracy, but with a compromised response time of half a second. In [152], an HIF detection approach using empirical mode decomposition (EMD) combined with an artificial neural network (ANN) is proposed, where the HIF detection and classification are achieved

through predominant harmonic signatures caused by HIFs in the electrical signals. Discrete wavelet transform is applied in [153] to monitor the high-frequency components and Long Short Term Memory (LSTM) to detect HIFs, revealing detection accuracy of 90% under scenarios with clean (not noisy) measurements. An HIF detection approach using discrete wavelet transformations and Back Propagation Artificial Neural Network (BP-ANN) is introduced in [154] and tested using often-noisy real measurement data from a substation, where the detection accuracy is reported 76%. While the accurate and swift HIF detection is a yet to be solved challenge in the electric industry, the state-of-the-art literature has demonstrated that AI technologies offer a yet-untapped potential in detecting HIFs and improving electrical safety by enabling a timely warming notification to the system operator and activating trip signals if needed.

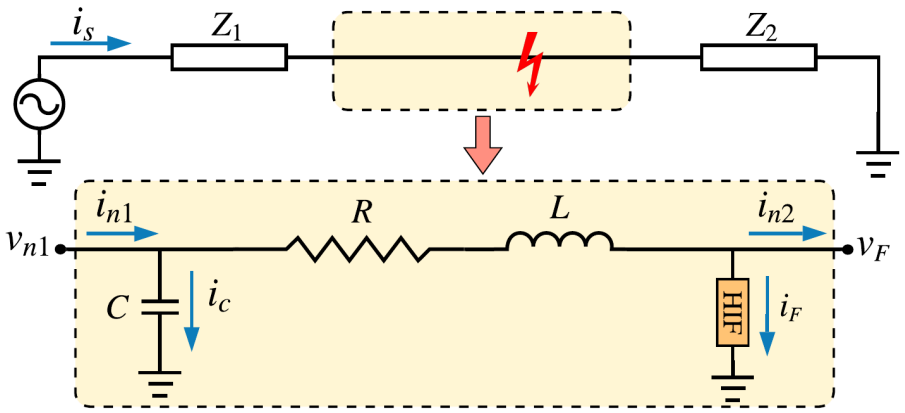

(a) A single-phase diagram for HIF modeling

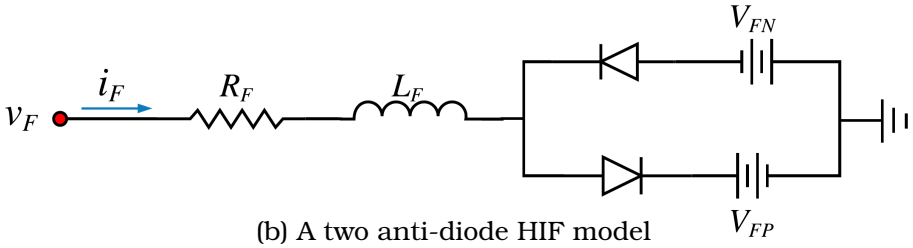

(b) A two anti-diode HIF model

Figure 4.1: A single-phase diagram for the HIF model in [2, 3]

A single-line diagram of an HIF event in a radial distribution system is illustrated in Fig. 4.1(a). The sending node is modeled by an ideal AC source; Z_1 and Z_2 are known impedance values and can be estimated according to the system topology and operating conditions; R, L and C stand for the per unit length resistance, inductance, and capacitance of the line. By applying Kirchhoff's voltage law to the dashed circle in Fig. 4.1(a), the following equation is derived:

$$v_{n1} = \delta \left(R(i_{n1} - i_c) + L\frac{\mathrm{d}(i_{n1} - i_c)}{\mathrm{d}t} \right) + v_F \tag{4.1}$$

where, v_{n1} and i_{n1} are the sending-terminal voltage and current; v_f stands for the voltage at the location of the fault; and δ is the fault distance from the sending-terminal. However, during an HIF event, v_F and δ are the values to be estimated. The current flow can be found through

$$i_{n1} = i_c + i_{n2} + i_F, \quad i_c = \delta\frac{\mathrm{d}v_{n1}}{\mathrm{d}t} \tag{4.2}$$

where, i_c, i_{n2}, and i_F are, respectively, the currents flowing through the shunt capacitor, received at the end-terminal, and observed at the HIF branch.

Under some HIF scenarios, arcs can be observed when the air gap between the power line conductor and the high impedance object is energized. Once the imposed voltage magnitude is higher than the voltage (breakdown voltage), there would be arc ignitions across the air gap. On the other hand, an arc extinguishes when the fault voltage is lower than the breakdown voltage. Therefore, the HIF current changes during each cycle, making its magnitude follow a non-linear characteristic [155]. Based on the above properties of an HIF event, an HIF model is developed and has been widely used in [2, 3, 142, 147, 149, 152], as shown in Fig. 4.1(b). The fault voltage

in this model can be written in the following format:

$$v_F = \begin{cases} R_F i_F + L_F \dfrac{\mathrm{d}i_F}{\mathrm{d}t} + V_{FP}, & i_F \geq 0 \\ R_F i_F + L_F \dfrac{\mathrm{d}i_F}{\mathrm{d}t} - V_{FN}, & i_F < 0 \end{cases} \tag{4.3}$$

where, R_F and L_F are the HIF's resistance and inductance in series; V_{FP} and V_{FN} are the positive and negative arc voltages during HIF events, which archives the non-linearity of HIFs. The simulated voltage and current waveforms are demonstrated in Fig. 4.2. It can be found that although there is almost no influence on the voltage waveform, the HIF event slightly distorts the current signal while the current magnitude has remained around the rated range; in other words, the HIF event cannot be detected easily by the conventional protective relays. One should note that, at the beginning of an HIF event, this HIF model can barely match the characteristics of the first period due to the build-up phenomenon [156]. However, following a few fundamental cycles, the HIF stabilizes and the fault parameters—R_F, L_F, V_{FP} and V_{FN}—are approximated as constant values. Therefore, the HIF current waveform and the related shoulder phenomenon can still be characterized using the model presented in Fig. 4.1(b).

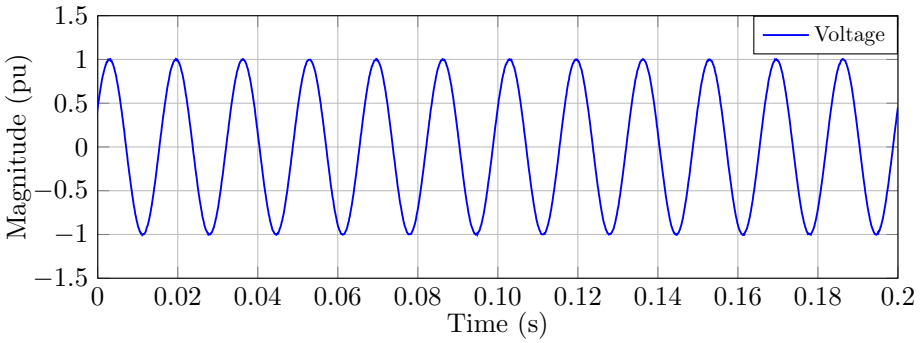

(a) HIF Voltage

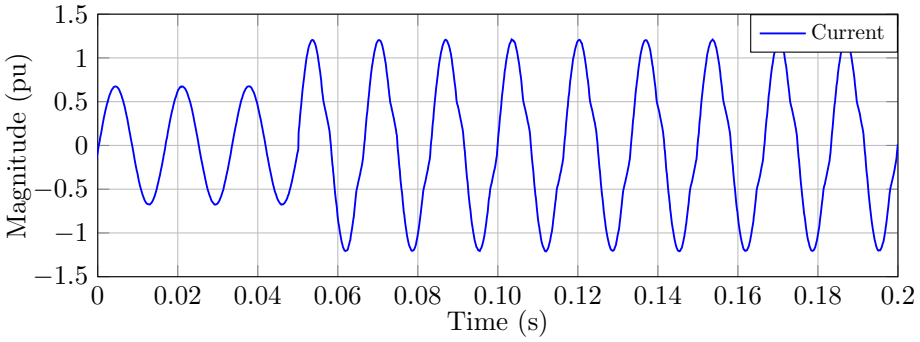

(b) HIF Current

Figure 4.2: Simulated voltage and current waveforms (with per unit values) captured at the sending-terminal based on [3].

Figure 4.3 illustrates a performance comparison of the STFT and WT. It can be observed, from the spectrum in Fig. 4.3c and 4.3d, that the HIF current waveform is featured with more harmonic components at larger than 5th orders, where the performance of the HIF detection method in [147] will be easily compromised by such harmonic pollution or noise interferences. Meanwhile, comparing the scalograms in Fig. 4.3e and 4.3f with the spectrograms from Fig. 4.3c and 4.3d, one can note that the results from STFT provide very detailed frequency information, and the scalograms obtained using Morlet WT from HIF-affected waveform reveal very obvious features compared to those from the harmonic-polluted waveforms; nevertheless, the accuracy in frequency measurements is compromised in WT. Therefore,

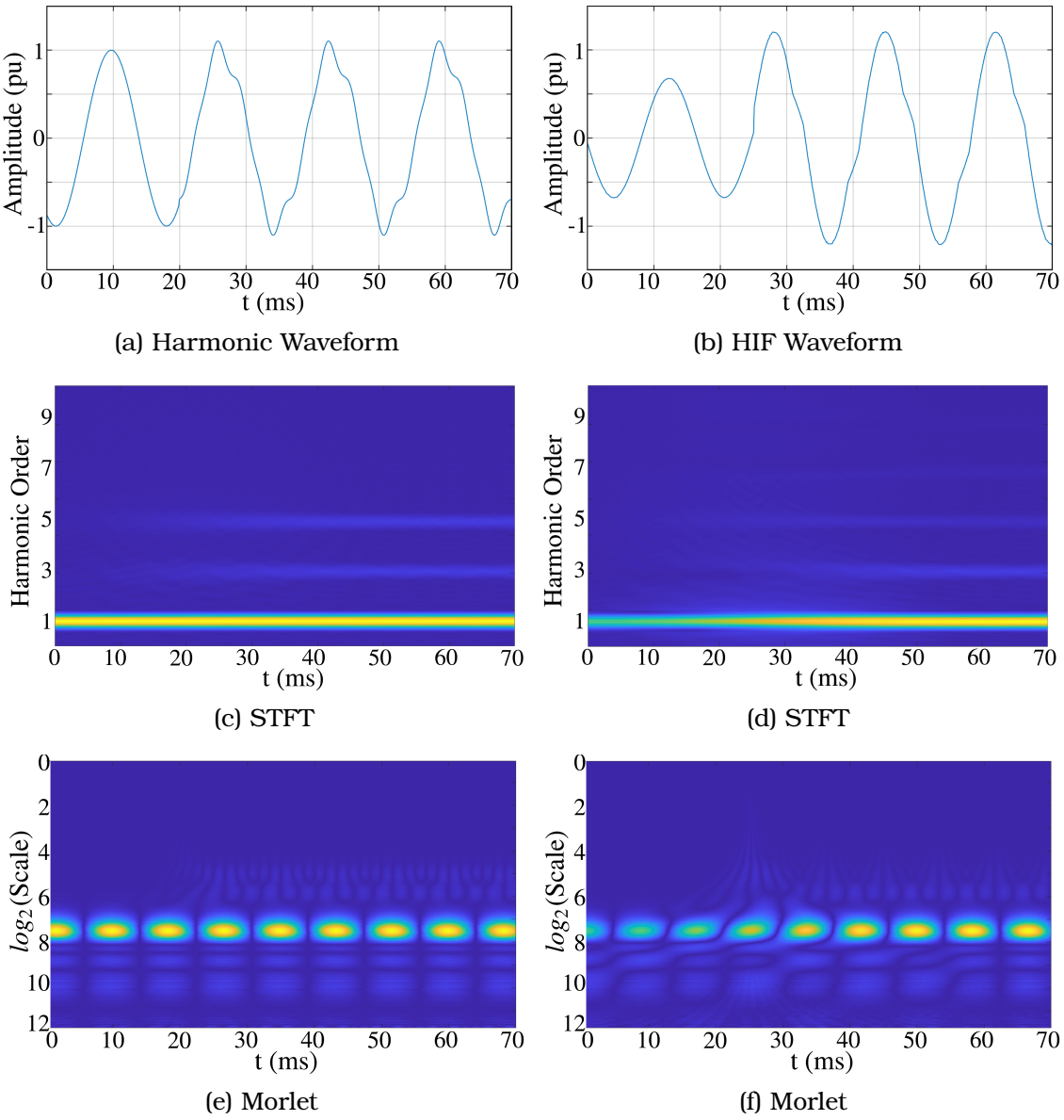

Figure 4.3: Comparison of the STFT vs. WT with: HIF-affected waveform and harmonic-injected waveform starting at t=20ms with harmonic orders h= 3 and 5 and magnitudes of 0.08pu and 0.08pu, respectively.

a combination of WT and STFT is generally much desired. However, this could highly increase the computational burden of the detection mechanism, and in particular, challenge the online applicability of the HIF detection schemes. In order to archive a low-computing complexity and yet accurate design, we select WT alone in this research project for power waveform

feature extraction and HIF detection.

4.3 Proposed HIF Detection Technology

With the Wide installation of Phasor Measurement Units (PMUs) in the power grid, micro-PMUs (μ-PMUs) in power distribution systems [157] and many other IEDs with PMU functionalities, HIF detection can be achieved through such devices with high-precision and high-resolution measurements; that is, the case presented in Fig. 4.1(a) can be easily solved as long as both sending and receiving terminals are equipped with such devices that can ensure the availability of high-precision high-resolution electrical measurements. However, a full observation is very hard to achieve in every segment of the power network due to the cost limitations [158] and only the power waveforms from the upstream (sending-end) terminal are usually measured. Therefore, it makes it very challenging for the HIF detection and classification scheme to operate as desired since the HIF current is viewed incremental by the upstream terminal, not large enough to violate the tripping thresholds in the protective relays, and are often mistakenly corresponded to the common load increments in the network.

As each single-phase current waveform captured from the upstream terminal in a radial power distribution system carries information of the downstream terminal, we mainly focus on detecting low-intensity HIFs which is one most challenging task in electric industry. The workflow of the proposed HIF detection technology is demonstrated in Fig. 4.4; it functionally consists of the following four modules:

1. ***Signal Acquisition:*** The proposed framework shares the same input waveforms of a typical PMU (or protective relay with PMU functionality) from the Analog to Digital (A2D) processing module. It avoids any

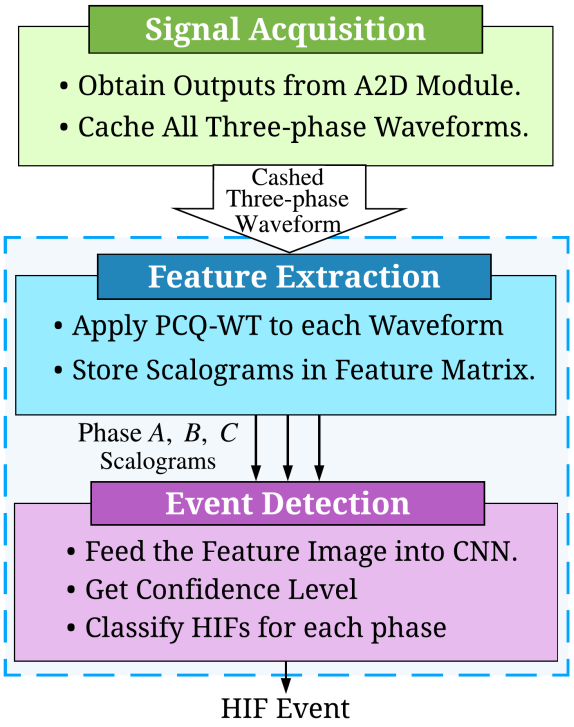

Figure 4.4: Series of integrated functions in the proposed HIF detection system.

additional A2D modules in the front-end, and makes the proposed architecture a economically-viable sensor solution. The waveform data is stored in the cache for the subsequent analytical processes.

2. ***Feature Extraction:*** This module applies pseudo-continuous quadrature wavelet transform (PCQ-WT) to the cached waveform data and generates scalograms. The scalograms are matrices that contain signal signatures corresponding to the HIF events in the power grid. The scalograms are then quantized to digital images in order to compress the data size.

3. ***Event Detection and Classification:*** The images obtained in the previous stage are fed into a compact CNN that, with a detection confidence, classifies whether there is an HIF event. Finally, the

detected event will be reported to the local protection device or the control center.

As one can see, the proposed HIF detection system only requires software-level modifications to the existing sensors (e.g., PMUs, protective relays, etc.), with no additional hardware investments. Here, we utilize a physics-guided machine learning technique, as the overall detection system only requires offline training. The training process is under the guidance of the pre-recorded and/or simulated HIF waveforms as the training dataset.

4.4 Improved HIF Modeling

The waveform assessment based on the HIF model presented in Fig. 4.1(b) is adequate to some extent; however, to enrich the proposed solution's knowledge on a variety of HIF waveforms, we propose a new and comprehensive HIF model shown in Fig. 4.5, where the fault resistance and inductance are assigned to the positive and negative branch. For simplicity, we name Z_{FP} and Z_{FN} as positive and negative arc impedances, respectively. One advantage of this proposed model is its flexibility to approximate different HIF conditions including those studied in [2, 3, 142, 147, 149, 152].

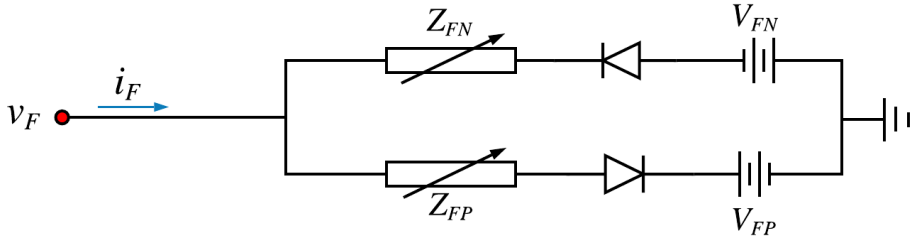

Figure 4.5: The proposed improved HIF model.

4.5 Feature Extraction and HIF Detection by CNNs

With the current waveforms carrying valuable information on the underlying phenomenon, one can evaluate the current waveform in each phase to examine the existence of HIFs. First, the current waveform can be generalized by

$$x(t) = A\cos(\omega t + \phi) \tag{4.4}$$

where, A, ω, and ϕ are the magnitude, frequency, and phase angle in each phase. Although HIF phenomena are hard to detect through current amplitudes, such events often cause waveform abnormalities and distortions. One should note that the orders, magnitudes, and phase angles corresponding to the HIF-caused harmonics would be totally different under different combinations of HIF parameters. Thus, detecting HIF through analyzing certain orders of harmonics will be extremely challenging; this is even further exacerbated by the existence of noise or other harmonics, altogether could compromise the performance of the HIF detection schemes. To deeply investigate the waveform features, we expand the sampled current by the Fourier series as follows:

$$x(t) = A_1\cos(\omega_1 t + \phi_1) + \underbrace{\sum_{h=2}^{H} A_h\cos(\omega_h t + \phi_h)}_{\text{Harmonic Components}} \tag{4.5}$$

where, h is the order of harmonics; H is the maximum order of harmonics limited by the sampling rate; A_h, ω_h, and ϕ_h are the h-th order harmonic component's instantaneous magnitude, frequency, and phase angle, respectively. Also, $h = 1$ stands for the fundamental frequency component. One

can see, in Fig. 4.2, that the fundamental magnitude is affected by both HIF and load variation events. Therefore, it is clear that the second term in (4.5) carries valuable information in assessing the HIF impacts, thus the main focus in the proposed data mining and pattern extraction process.

4.5.1 PCQ-WT Based Feature Extraction for HIF Events

Apply the proposed modified Gabor WT—(3.13) from Section 3.4.1—to each harmonic component in (4.5) and the Hubbard–Stratonovich transformation [137], the WT of (4.5) turns into

$$\begin{aligned} X(\omega_h|a,b) = &\frac{A_h}{2} e^{j\omega_h(\phi_h+b)} \cdot a\alpha_0\sqrt{\pi} e^{-\frac{\alpha_0^2}{4}(a\omega_h-\omega_c)^2} \\ &+ \underbrace{\frac{A_h}{2} e^{-j\omega_h(\phi_h+b)} \cdot a\alpha_0\sqrt{\pi} e^{-\frac{\alpha_0^2}{4}(a\omega_h+\omega_c)^2}}_{\approx 0}. \end{aligned} \tag{4.6}$$

It can be seen that the second term on the right side of (4.6) can be neglected as the exponent in the last exponential operation is a large negative. When $\omega_0 = \omega_c/a$, $X(\omega_h|a,b)$ reaches its maximum value, indicating that the dominant feature of the selected frequency is extracted. Accordingly, and based on (3.13), the length of the Gaussian window in Gabor wavelet also adapts different frequencies.

Applying the discrete form of the Gabor wavelet from (3.21) with different discrete scaling factors a_k and time shift b_k, we achieve the proposed PCQ-WT as follows,

$$\begin{aligned} X(\omega_k|a_k,b_k) &= \sum_{n=0}^{W-1} x[n]\Psi^*[\frac{T_s(n-b_k)}{a_k}] \\ &= \sum_{n=0}^{W-1} x[n] exp\left(-j\frac{\omega_c}{a_k}T_s(n-b_k) - \frac{T_s^2(n-b_k)^2}{a_k^2\alpha_0^2}\right). \end{aligned} \tag{4.7}$$

If the pseudo frequencies of interest and the Gabor wavelet bank are designed properly, a set of PCQ-WTs in form of a vector $\mathbf{X}_{\underline{\omega}}$ can be generated conveying waveform features in a certain frequency range. During both transient and steady state operating modes, WT time-frequency analysis is conducted along time, and a scalogram stream can be then achieved.

4.5.2 CNN Configuration for HIF Detection

With the PCQ-WT extracted features in form of scalograms available, the HIF detection problem is converted to a supervised scalograms classification problem. However, the classification of the high-dimensional 2-D scalograms is challenging. specifically, every frame of the obtained scalogram has hundreds by hundreds ($scales \times time$) pixels; it is very challenging to process such high dimensional data through the conventional pattern classification approaches. Here, we convert the PCQ-WT scalograms into 2-D images and propose a compact CNN architecture to classify the HIFs concealed in the scalograms by the PCQ-WT. The proposed CNN has a simple architecture for HIF detection, yet achieving a very fast processing time for online applications.

4.5.3 PCQ-WT and CNN Parameter Setting

The sampling rate Fs for the signal and the feature extraction is 7680Hz which provides 128 samples per nominal fundamental cycle. The observation window for the PCQ-WT is set to 308 samples (40ms). The time shift b for the modified Gabor daughter wavelets is 10ms (77 samples) for simplicity. The scaling factor a for the proposed PCQ-WT is chosen as 2^i, where i is sampled uniformly from 0 to 8. The central frequency $\omega_c = 1152$ and the pseudo frequency will roughly reach up to the 19th order of harmonics. All

Table 4.1: Parameter Specifications for Generating the Test Waveforms

System Setting			
V_{base} *	13.8kV	S_{base}	0.5 MW
Fs	7.68kHz	Line Length	2km
S_{Load}	0.5 - 1.5 pu	pf_{load}	0.8 - 1
HIF Model Setting			
Parameter	Range	Parameter	Range
Z_{FP}	0.02 pu - 1.5 pu	Z_{FN}	0.02 pu - 1.5 pu
pf_{FP}	0 - 1	pf_{FN}	0 - 1
V_{FP}	0.08 pu - 0.65 pu	V_{FN}	0.08 pu - 0.65 pu
Fault Location	1% - 99%		

* :A signal to noise ratio of 40dB is added to the AC voltage source.

the Gabor wavelets have 20ms duration. By this design, the computational complexity in computing the scalograms is reduced, while the pseudo frequency bandwidth coverage for feature extraction will not be compromised. The scalograms fed into the CNN are cropped from 10ms to 50ms (of the total 60ms WT output)—i.e., observation+ wavelet length— which has 40ms (308 samples) duration.

The proposed compact CNN configuration for scalogram classification is as follows: Input layer (256×308); Convolution (Conv.) layer (32×5×11); Max-pooling layer (3×3); Conv. layer(32×5×5); Max-pooling layer(3×3); Conv. layer(32×5×5); Full-connected (FC) layer(200×1); FC layer(3×1). Conventional images have homogeneous units on the horizontal and vertical axes, while the scalograms axes carry different information regarding the HIF events on either time or frequency. Therefore, a wide kernel in the first Conv. layer that can extract more information from the transitions along the time axis is used. The stride of the first layer is (2,3), and the remaining Conv.

layers use strides with a size of (1,1). Besides, batch normalization [159] is used in the last FC layer. In the last Conv. layer and the first FC layer, Dropout [139] is used to prevent over-fitting. All activation functions in the CNN are Rectified Linear Unit (ReLU). We choose cross-entropy as the loss function. Also, our proposed CNN is not that "deep" compared to the regular image classification CNNs; the suggested compact CNN architecture further reduces the computing complexity in HIF detection.

4.6 Case Study and Numerical Experiments

4.6.1 Test Scenarios Configuration

The parameter specifications used for generating the test waveforms are listed in Table. 3.1. We, in particular, focus on HIF event detection since conventional faults can typically be detected by existing protective devices. Three test scenarios (HIF event, load change event, and normal operation event) are simulated. For each HIF simulation, all parameters are *randomly* selected in the designated ranges. In each simulated waveform, only one event occurs at a random point in time. The waveform generation system is developed according to Fig. 4.1(a) and the improved HIF model in Fig. 4.5. Gaussian noises with SNR of 40dB are added to the AC voltage source to approximate the thermal and measurement noises in different conditions.

A total of 20,000 samples from the test waveforms are simulated for each event; therefore, a total of 60,000 samples (wavelet scalogram) are simulated in the MATLAB/Simulink environment. A total of 48,000 samples are randomly selected as the training dataset, 6,000 samples for validation, and 6,000 samples for testing datasets. For training the neural network and increasing the versatility of the CNN, the generated waveforms are manually

imposed by white Gaussian noise with 30dB SNR. We use Adam [160] as the optimizer, which has the initial learning rate of 1×10^{-4}, and weight decay of $1 \times 10^{-}5$. We trained the proposed CNN 120 epochs. The best validated model was recorded and tested.

4.6.2 Experimental Results and Analysis

4.6.2.1 Feature Extraction

The extracted features from an HIF and a load change events are demonstrated in Fig. 4.6, where the main energy concentration with high intensity is marked by red standing for the fundamental frequency component extracted from the waveforms. In Fig. 4.6(a), the HIF at $t = 20$ms increases the main energy concentration at $t = 30$ms, which matches the corresponding magnitude increase in Fig. 3.3(e). This phenomenon can also be observed in Fig. 4.6(b), as a load increase will indeed increase the magnitude of the current waveform. When evaluating high frequency areas in both scalograms, one can see that the higher frequency range (scale from 0 to 96) has less discontinuous patterns compared to the lower frequency range (scale from 96 to 192). However, the latter (96 to 192) is discontinuous with ripple shape carrying significant differences in Fig. 4.6(a) and Fig. 4.6(b).

For the HIF scalogram, the ripple pattern is formed at $t = 35$ms and becomes stable afterward; thus, one can see that it will take less than 20ms (PCQ-WT window length) to reveal the corresponding HIF patterns—some pyramid shape ripples appear in a group. When there is a load increase event, the load change feature takes 10ms to emerge (see the input waveform in Fig. 4.6(b)) and the impact remains consistently present. However, for scale from 96 to 192, there is no pyramid shape ripple found as those in Fig. 4.6(a). Also, only the intensity of the existing ripples slightly increases. One

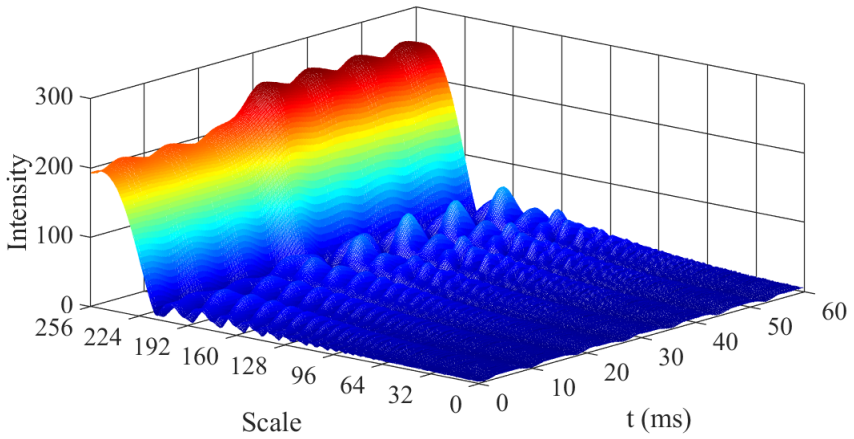

(a) HIF with SNR 30dB

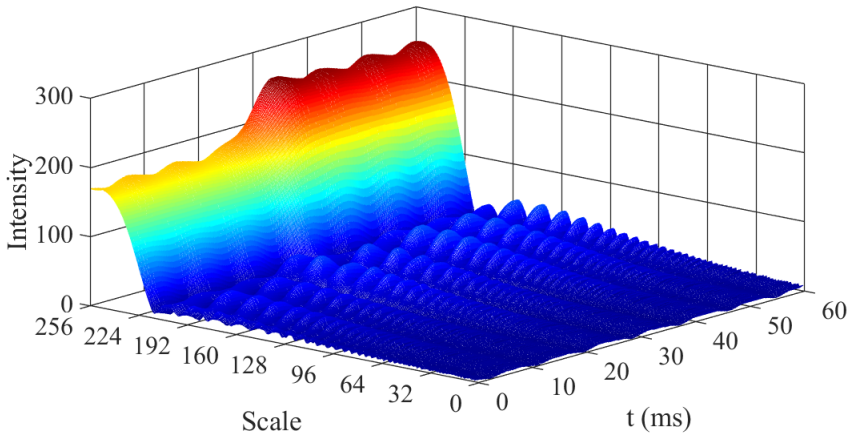

(b) Load Increase with SNR 30dB

Figure 4.6: Test waveform simulation results: (a) HIF event; (b) Load increase event; both simulated events start at t=20ms.

should notice that the patterns extracted from this simulated HIF event approximately covers the scale from 100 to 200, which roughly corresponds to the 12th to 5th order harmonics in the frequency span.

4.6.2.2 Event Detection

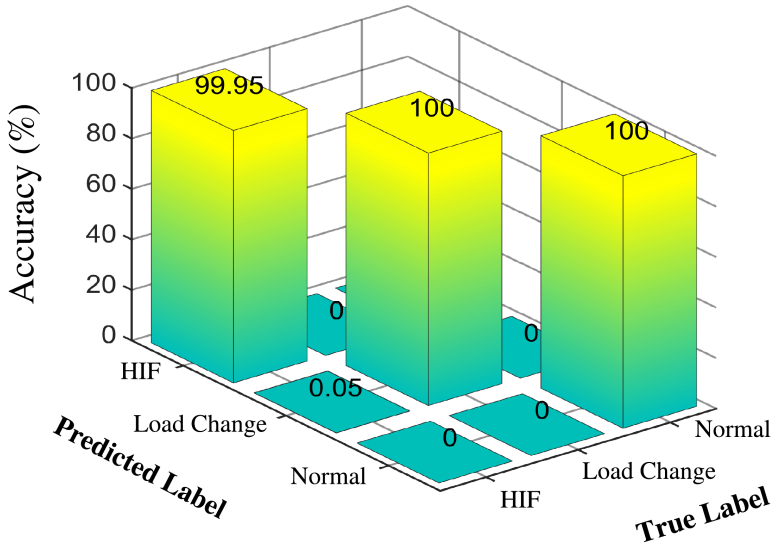

Figure 4.7: Test results of the proposed CNN framework for online HIF detection and classification

The HIF detection test results are summarized in the confusion matrix in Fig. 4.7, where the true label stands for the actual tested events, and the predicted label corresponds to the classification outcomes of the CNN module. The average accuracy of the proposed HIF event detection scheme is found 99.95 %. To further examine the online event detection and classification performance, we used a workstation with a stock eight-core AMD Ryzen 3800X CPU as the computational platform. We transfer the PCQ-WT and CNN modules into MATLAB 2020a to record the computational time on one single core of the CPU. The overall time for processing the PCQ-WT and CNN is recorded as 6.3±0.6ms, confirming a promising solution to be used

in real-time HIF detection applications.

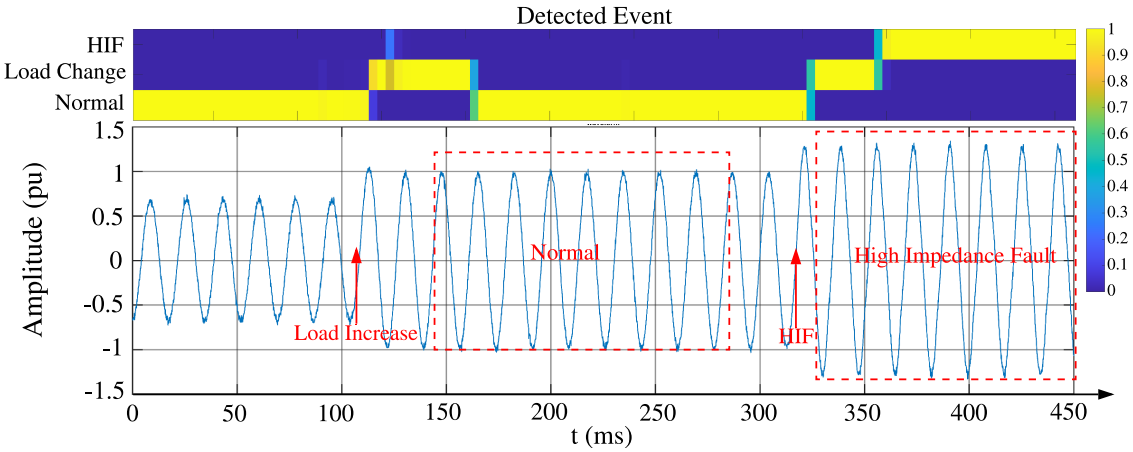

Figure 4.8: Online HIF detection on a simulated single-phase current waveform: detected result (top) and original waveform (bottom).

We also test the proposed framework on a recorded waveform of 0.45s duration, the result of which is shown in Fig. 4.8. The top heat-map is the event detection results over time, where the classification confidence rate is marked with the color bar. One should note that, during the *Normal* operating event, the confidence rate is very high and the classification result is accurate even though the waveform is polluted with 30dB Gaussian noise and the distortion is very obvious. Relatively lower confidence rates always exist during the transitions between two different events.

The *Load Change* event is detected accurately within 10ms and it takes another 40ms for the detection scheme to report a normal condition event. Meanwhile, at the moment of HIF occurrence, the CNN module classified the first two cycles of HIF-contained waveform (from $t = 325$ms to $t = 355$ms) mistakenly as the *load change* event. The reason lies in the fact that a *load change* event (Fig. 4.6(b)) reveals similar patterns at the very beginning when compared to the *HIF* event (Fig. 4.6(a)); therefore, it is very hard to make a correct detection and classification decision at the exact time when

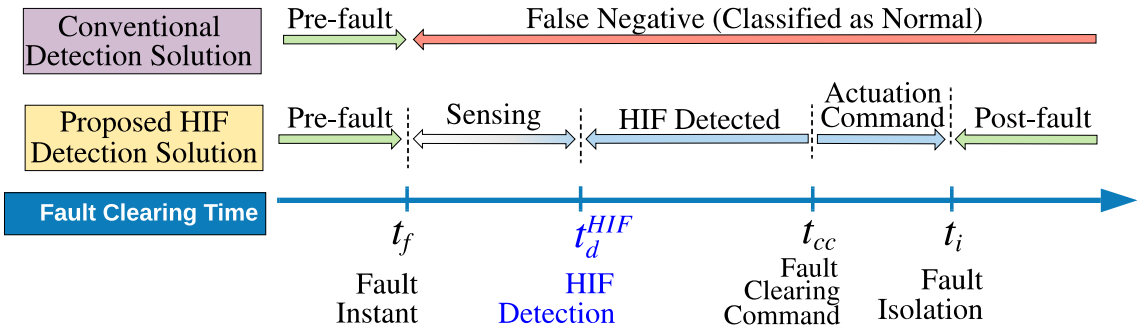

Figure 4.9: Comparison of the proposed approach with conventional protective relay during an HIF event.

the HIF event happens. However, when the waveform magnitude stabilizes, the CNN module shows a high confidence rate in classifying the HIF event correctly. Also, one can see that the maximum peak value of the current waveform affected by an HIF event is observed 1.25 pu which will barely trip the protective relays in the absence of the proposed HIF detection scheme.

A comparison between the proposed approach and the conventional protection relays in dealing with an HIF event is demonstrated in Figure 4.9. When the HIF event occurs, the conventional protective relay cannot sense this event due to the high impedance nature of the fault and the corresponding low current generated; thus, a normal operating condition is mistakenly reported and HIF would not be cleared timely. Consequently, undesired damages or disasters may be caused, human life and property would also be threatened. On the other side, however, the proposed scheme can detect the HIF event and after reaching a timing threshold, the relay trip actuation command is sent to isolate the HIF. One should notice that the proposed HIF detection engine can cooperate with the existing protective relays to provide HIF protection functionality.

In summary, the proposed solution provides satisfactory results in detecting low-intensity HIFs under noisy measurements and can distinguish

it with load change events. Moreover, the overall detection accuracy is desirable (99.98%) achieved at a promising detection speed of within 40ms (33ms delay plus 6.3±0.6ms processing time).

4.7 Conclusion

This chapter presented an effective scheme that leverages artificial intelligence advancements for detecting HIFs in power grids and improving electrical safety. The proposed solution functionally integrates a PCQ-WT feature extraction tool using a modified Gabor wavelet and a compact CNN-based event detection technique. Experiment results demonstrated that the proposed analytics successfully achieved an ultra-fast (within 40ms) and accurate (99.95% accuracy) HIF detection performance even under noisy measurements. Also, the proposed function could be embedded within the existing PMUs and/or other IEDs that are capable of capturing and processing the power waveforms.

Chapter 5: Smart Sensor Technology for Detection of Geomagnetically Induced Currents (GIC)

5.1 Abstract

Geomagnetically induced currents (GICs) in power grids are mainly caused by geomagnetic disturbances especially during solar storms. Such currents can potentially cause negative impacts on power grid equipment and even damage the power transformers resulting in a significant risk of blackouts. Therefore, monitoring GICs in power systems and developing solutions to mitigate their impacts before rising to a certain threatening level is urgently in need. Monitoring GICs is, however, quite a challenge and costly, as they usually appear in forms of DC components in the high voltage transmission lines, which are barely accessible through transformers. By examining the measured currents from the current transformers (CTs), we developed a solution to detect GICs in power transmission systems using the smart sensor concept in this chapter. Simulated results verify that the proposed approach can promisingly estimate GICs in power systems during a variety of grid operating conditions.

5.2 Introduction to GICs

Geomagnetic disturbances (GMDs) are mainly caused by solar storms, during which charged particles erupt from solar flares resulting in coronal mass ejections into space during the intensity peak of the sun's cycle. Consequently, geomagnetically induced currents (GICs) will appear in the conductor surface of the Earth. The flow of these currents into power transmission

lines can potentially cause "half-cycle saturation" of high-voltage bulk power transformers. This phenomenon can lead to relay miss-operations, voltage dips, elevated reactive power demand, transformer overheating, disruptive harmonics, aging or malfunction of the electric power devices, and even a total collapse of the grid in the worst scenarios [161–165].

Northern North America is particularly susceptible to problems resulting from GICs. On March 13, 1989, an exceptionally strong GMD caused major damages to electrical power equipment in Canada, Scandinavia, and the United States. Hydro-Quebec extra high voltage (EHV) transmission system experienced instability and tripping of lines carrying power to Montreal resulting in the total blackout of the Hydro-Quebec system [166, 167]. In the United States, a voltage fluctuation of up to 4 percent was recorded on the EHV systems in Pennsylvania, New Jersey, and Maryland. On September 19, 1989, a second solar storm damaged the step-up transformers at the Salem Unit 2 nuclear power plant [168].

Limiting the potential GICs-caused damages in power grids calls for developing advanced tools and mechanisms to monitor and detect GICs as they unfold and also solutions to mitigate the impacts before they rise to a certain threatening level. On one hand, the GMD phenomena may not always result in GICs in power systems. On the other hand, directly accessing GICs—which represents itself as a DC component in high voltage transmission lines—is costly and a challenge. Conventional techniques to monitoring high voltage transmission lines rely solely on the AC measurements through voltage transformers (VTs) and current transformers (CTs), simply neglecting the DC components flowing on transmission lines. Additionally, there are other sources of harmonics in power grids, generated by nonlinear loads or overloading transformers, that may flow in the grid [169]

and can interfere with those harmonics generated by GICs, particularly when GMD level is low. Such interference will make the GICs detection a challenge, as the measured waveforms from CTs or VTs capture all harmonic signals together with the fundamental component—50 Hz or 60 Hz.

Several studies have focused on modeling harmonic-embedded power flows and mitigation solutions when facing GICs in power systems [162, 170–172]. Different mitigation strategies should be taken depending on the severity of GICs impacts on the grid. However, research and development efforts on GICs impact detection mechanisms are found scarce. The proposed techniques in [173, 174] are centered on monitoring GICs mainly based on analyzing the distorted waveforms; however, none has considered the appearance of other grid harmonics and the conflicting interactions with those of GICs. Furthermore, thermal noise would be higher in the transformer secondary winding due to the accumulated heat during transformer saturation, which adds another layer of interference, making GICs detection harder than usual. Additionally, studies in [163] demonstrated that the excited harmonic current magnitudes of different orders vary when GICs intensity increases. The harmonic components generated by GICs behave in different ways and the existing detection mechanisms do not consider such complex interference.

Studies in [169] show the promising performance of transformer overloading detection by applying wavelet transforms. Machine learning mechanisms have been widely utilized in solving electric power system problems [11, 48, 175, 176] and are being frequently approached to revolutionize the solution techniques and emerging technologies in power grids. Inspired by the principle concepts of feature extraction and event detection based on waveform analysis, this chapter proposes a GIC detection solution in

high voltage transmission systems. Two major time-frequency analysis techniques, namely the wavelet transform (WT) and short-time Fourier transform (STFT), are applied and their performance are evaluated. We further propose a GIC detection algorithm centered on a hybrid WT and STFT combined with a machine learning approach, Convolutional Neural Networks (CNN). We demonstrate the promising performance of the suggested analytics in detecting the GIC impacts in power grids under a variety of grid operating conditions. The proposed framework: (i) is resistive to harmonic distortion and background noise, (ii) is capable of detecting low-intensity GICs, and (iii) can be algorithmically embedded within Phasor Measurement Units (PMUs) and other intelligent electronic devices (IEDs) currently in place for online monitoring.

5.3 GIC Impact Modeling

5.3.1 Transformer Half-cycle Saturation

The GMD phenomenon introduces an earth magnetic field change rate of usually below 1 Hz [162]. Typically, GICs can be determined by assessing the DC network power flow as:

$$\mathbf{I} = \mathbf{GV} \tag{5.1}$$

where **G** is the network bus admittance matrix, determined by taking into account the three-phase signals, the substation neutral buses, as well as the ground resistances. Utilizing the approach presented in [161], the GMD introduces voltages that can be approximated by

$$V = E_N L_N + E_E L_E \tag{5.2}$$

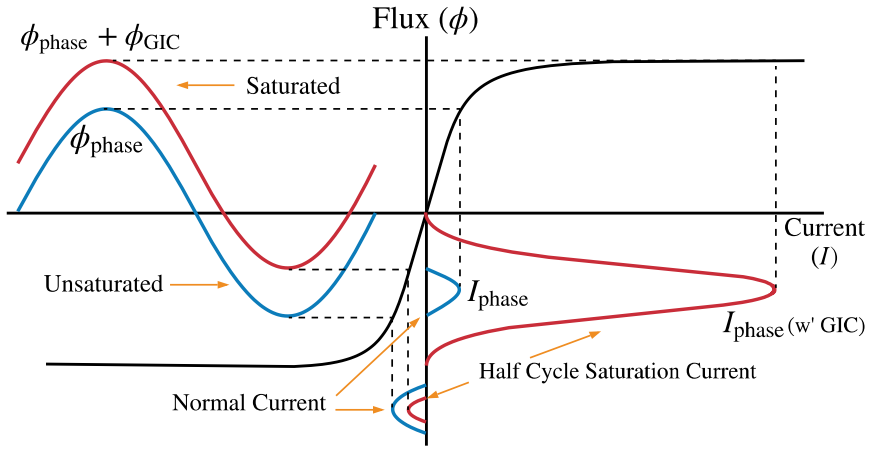

Figure 5.1: Half-cycle saturation of a single-phase transformer due to GICs.

where E_N and E_E are the Northward and Eastward electric field (V/km), respectively, and L_N and L_E are the Northward and Eastward distance, respectively.

In transmission systems, Y-Y configuration transformers are the most vulnerable to half-cycle saturation during a GMD event. As graphically demonstrated in Fig. 5.1, this is because the DC flux has the lowest reluctance path in such scenarios and a semi-saturation can occur [177]. However, GICs alone may not be able to cause a transformer half-cycle saturation as (i) GICs intensity may be low and (ii) the transformer load level may be small. According to [163], when a transformer is injected with different levels of GICs, the harmonic magnitude curves (in frequency domain) will differ significantly (see Fig. 5.2), thus the waveforms will change dramatically too. Such behaviours in the waveforms will make the GICs detection process extremely difficult, calling for a holistic mechanism and an accurate approach.

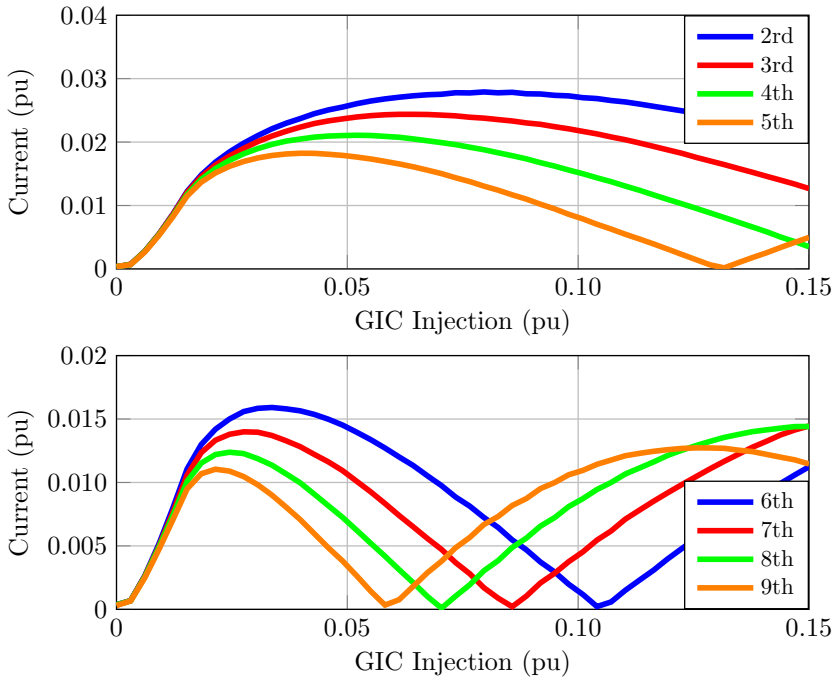

Figure 5.2: Excited harmonic current components in different levels of GICs.

5.3.2 GIC Waveform Modeling

As the current in the secondary winding of CTs can be captured and assuming a balance three-phase system, the power waveform in each phase can be represented using Equation (3.1) from Section 3.3.1). Although GICs cannot be measured directly, their impacts can be assessed on the DC saturation level of transformers as GICs generates a set of harmonic components only during the transformer half-cycle saturation. Thus, the waveform can be expanded by Fourier series as Equation (4.5), Section 4.5). Under a particular level of GICs, different values of A_h and f_h can be detected according to [163], resulting in a unique set of patterns. A certain combination of A_h for ω_h (for h = 2, 3, 4, ..., H) will possibly be resulted, even if some GICs-caused harmonics are influenced by those generated from other sources. The second term in (4.5) will still contain valuable

information on the GICs impacts and, thus, could be the main target for data fusion and pattern extraction.

As the feature extraction outcomes through WT are much more conspicuous than those of STFT, while compromising the accuracy in frequency measurements. Therefore, a joint hybrid application of WT and STFT is pursued in this research for waveform feature extraction and the corresponding analysis to archive the best detection result.

5.4 Feature Extraction and GIC Detection by CNNs

As single-phase CTs receive the current waveforms from the transmission lines, the GIC impacts can be evaluated through CTs located in different substations. In this Section, the assessment focuses on one CT modeled based on the considerations presented in Fig. 5.1 and Fig. 5.2. The approach is, however, generic enough to be applied to different models and number of CTs across the system. Moreover, the CNNs are able to generalize and adaptive to different CT parameters, as long as the waveforms obtained from a specific CT are included in the training data set.

As wavelet transformations can be considered a special type of convolution, it is possible to integrate the feature extraction phase of the proposed approach into the CNNs. Some literature suggested using wavelets to replace the kernels of the first layer in CNNs [178] [179] and advocate a better performance than that resulted from the conventional CNNs [180]. However, the waveforms in power systems are 1-D and very different from the 2-D natural images which are featured by edges or spots, etc.; additionally, wavelet analysis is a mature approach that can extract informative features from the power waveforms; we, therefore, choose a two-phase scheme (wavelets + CNN) in our proposed framework.

5.4.1 PCWT-based Feature Extraction during Transformer Half-Cycle Saturation

Based on the half-cycle saturation waveform in Fig. 5.1, which is a Gaussian-like curve, the Gaussian wavelet is a natural candidate for the mother wavelet. A Gaussian wavelet can be expressed as follows

$$g_n(x) = (-1)^n \frac{d^n}{dx^n} e^{-\frac{x^2}{2}}, \tag{5.3}$$

where n is the order of the Gaussian wavelet [181]. According to (3.5), the WT with Gaussian mother wavelet can be expressed as follows

$$X_g(\omega|a,b) = \frac{1}{\sqrt{C_{g_n}}} \int_{-\infty}^{\infty} x(t) g_n(\frac{t-b}{a}) dt, \tag{5.4}$$

and

$$C_{g_n} = 2\pi(n-1)!. \tag{5.5}$$

When conducting the N^{th} order Gaussian wavelet transform, (5.4) can be simplified by applying partial integration multiple times (see Appendix A.1 for more details), and (5.4) changes to

$$\begin{aligned} X_g(\omega|a,b) = & \underbrace{\frac{1}{\sqrt{C_{g_N}}} \sum_{n=0}^{N-1} \left[(-a^n \tfrac{d^n}{dt^n} x(t) \tfrac{d^{(N-n)}}{dt^{(N-n)}} g_0(\tfrac{t-b}{a}) \right]_{-\infty}^{+\infty}}_{\text{zero}} \\ & + \frac{1}{\sqrt{C_{g_N}}} \int_{-\infty}^{\infty} a^N \tfrac{d^N}{dt^N} x(t) g_0(\tfrac{t-b}{a}) dt. \end{aligned} \tag{5.6}$$

As $x(t)$ consists of sinusoidal waveforms only, for a given frequency ω_h with A_h and θ_h, (5.6) can be rewritten as

$$
\begin{aligned}
X_g(\omega_h|a,b) &= \frac{A_h a^N}{\sqrt{C_{g_N}}} \int_{-\infty}^{\infty} \frac{d^N}{dt^N} cos(\omega_h t + \theta_h) \cdot e^{\frac{-(t-b)^2}{2a^2}} dt \\
&= \frac{A_h a^N}{2\sqrt{C_{g_N}}} \int_{-\infty}^{\infty} \frac{d^N}{dt^N} [e^{j(\omega_h t+\theta_h)} + e^{-j(\omega_h t+\theta_h)}] e^{\frac{-(t-b)^2}{2a^2}} dt.
\end{aligned}
\tag{5.7}
$$

By applying the Hubbard-Stratonovich transformation [137]

$$
\sqrt{2\pi\alpha} \cdot e^{-\frac{\alpha}{2}x^2} = \int_{-\infty}^{\infty} e^{-\frac{y^2}{2\alpha^2} - jxy} dy, \tag{5.8}
$$

and using the rule of sign change when swapping integration limits, (5.7) can be simplified by substituting $y = t - b$,

$$
\begin{aligned}
X_g(\omega_h|a,b) = &= \frac{A_h (a\omega_h)^N}{\sqrt{C_{g_N}}} cos(\omega_h b + \theta_h + \frac{N\pi}{2}) \int_{-\infty}^{\infty} e^{-\frac{y^2}{2a^2} - j\omega_h y} dy \\
&= \frac{A_h (a\omega_h)^N}{\sqrt{(N-1)!/a}} cos(\omega_h b + \theta_h + \frac{N\pi}{2}) e^{-\frac{a}{2}w_h^2}
\end{aligned}
\tag{5.9}
$$

ω_h, A_h, θ_h are constants for one harmonic component, and N is also a constant when the order of the Gaussian wavelet is selected. Only b determines the moment when $|X_g(\omega_h|a,b)|$ reaches maximum; therefore, we let the value of *cos* function be one. In this way, only the value of a controls the attenuation of the selected frequency components. Figure 5.3a shows the features when a small value of a (less than four) is selected. One can see that the frequency coverage focuses on the high-frequency range, and amplification of these frequencies is low. When the value of a increases, the covered frequency range gets wider, and the amplification focuses on a certain range of the high frequency component. On the other hand, it has been proved that Fourier transform of a Gaussian waveform leads to another Gaussian curve in frequency domain. Similarly, when choosing a fixed value of a, the frequency coverage of a Gaussian wave is also a Gaussian-

like curve. These characteristics are very suitable for feature extraction corresponding to a transformer saturation event, because the saturation waveform contains a Gaussian-like curve. Daughter wavelets with proper values of a could detect saturation and eliminate the influence of high frequencies. In contrast, the frequency coverage and the gain of the Morlet wavelet transform (Fig. 5.3b) mainly focus on low frequencies when a is greater than three. Even though it is a unilateral Gaussian-like curve with different value of a, the highlighted frequencies are low and suitable for feature extraction on the fundamental component. Detailed derivation of the Morlet wavelet transform for a sinusoidal waveform is shown in Appendix A.2. Therefore, we choose the Gaussian wavelet to be used in PCWT for the application of interest. Finally, the PCWT for feature extraction for GICs detection can be easily obtained by applying (3.6) to (5.6). All the parameter settings will be introduced in Section 5.4.3.

5.4.2 GICs Detection by CNNs

The overall framework for the proposed detection mechanism is demonstrated in Fig. 5.4. First, PCWT with K number of a and STFT in L time instants are applied sequentially. Then, the scalogram and spectrogram will both be of $K \times L$ size and carry the valuable information on the intensity of GICs. The detection process could be converted as a supervised classification problem on the scalograms. However, the classification process for the 2-D scalograms is challenging due to their high dimensionality. Specifically, every frame of the obtained scalogram and spectrogram has hundreds by hundreds pixels; such high dimensional data is restrictive in most of the conventional pattern classification approaches. We cast the event detection (saturation caused by GICs) to an image classification problem based on

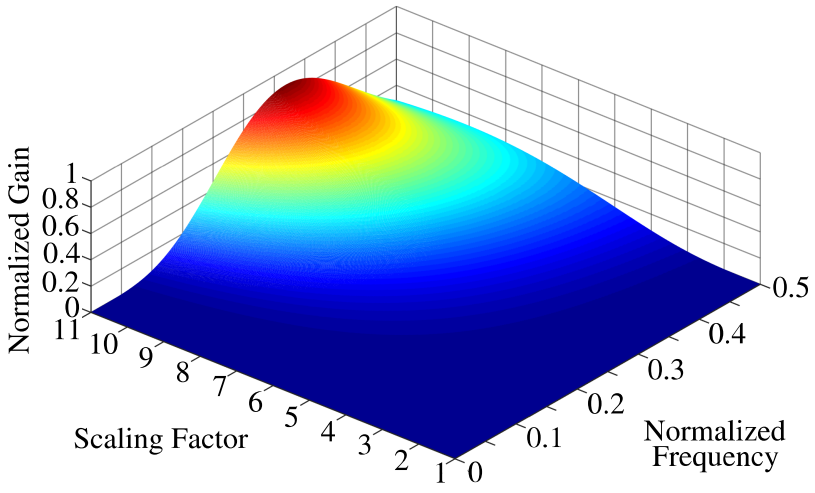

(a) Gaussian Wavelet

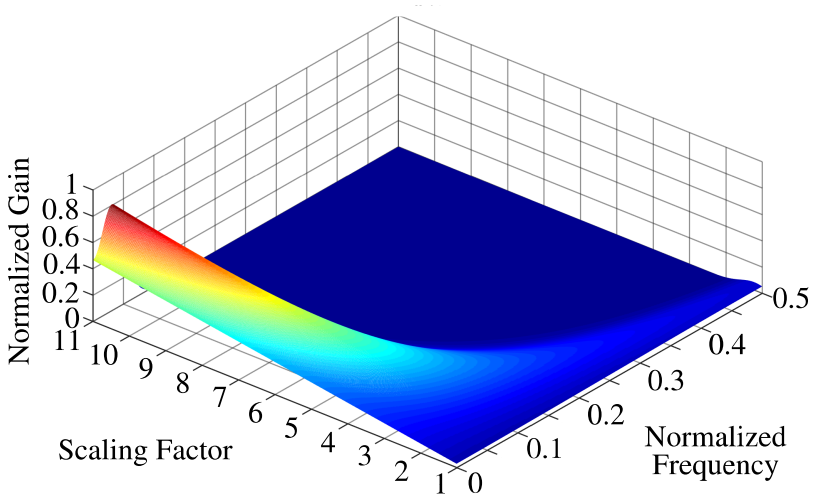

(b) Morlet Wavelet

Figure 5.3: Frequency coverage comparison of the Wavelet transform between Gaussian wavelet and Morlet (normalized frequency f_h is used).

the scalogram and spectrogram; we propose a CNN-based architecture to classify the images. The proposed CNN offers a simple architecture that ensures an accurate detection, yet fast and computationally effective. Our proposed CNN consists of five layers: three convolutional (Conv.) layers and two fully-connected (FC) layers; the specifications of the CNN will be introduced in Section 5.4.3. This framework can work as a standalone event

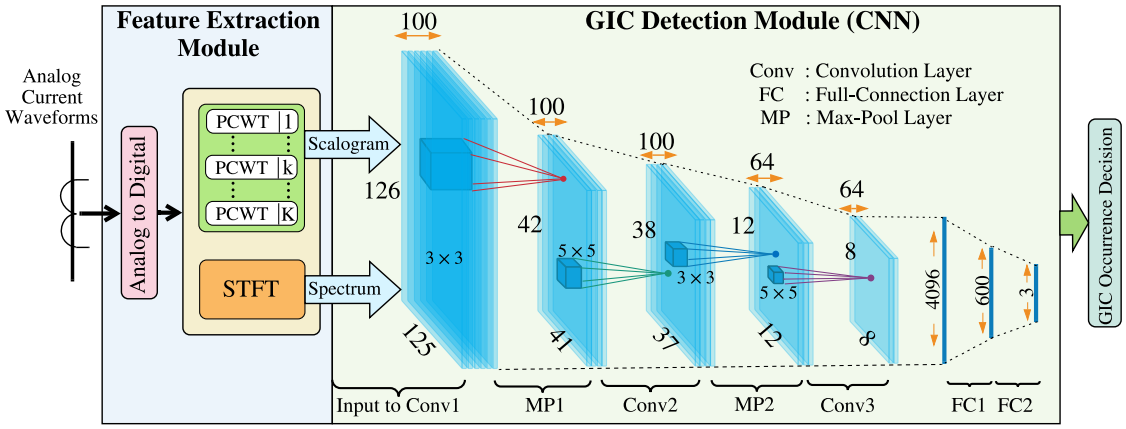

Figure 5.4: The general architecture of the proposed framework for GIC detection in power grids.

detector or classification tool in a PMU to detect the GICs.

5.4.3 PCWT and CNN Parameter Setting

The sampling frequency used in this chapter is $Fs = 9600$ Hz, which is sufficiently high to cover up to 50^{th} order of harmonics. The buffer size (observation window) for the PCWT and STFT are both set to 192 samples (20 ms). A Gaussian wavelet with order of 8 is employed. The time shifting b for all Gaussian daughter wavelets is set to be 10 ms (96 samples) for the sake of simplicity. The proposed scaling factor a for Gaussian wavelet is chosen as 2^i, where i is sampled among 256 uniform intervals in the range of $[-12, -4]$. The Gaussian mother wavelet has 20 ms duration, which is obtained by applying a unit length (1 s) Gaussian wavelet function into a 20 ms window. This transform is approximately equivalent to applying scaling factors from zero to eight with a mother wavelet of frequency 4,000 Hz. Such selection of parameters reduces the computational burden associated with the scalogram acquisition, while does not sacrifice the bandwidth coverage for feature extraction. The scalograms have a duration of 40 ms (385 samples).

The proposed CNN for scalogram classification is illustrated in Fig. 5.4 with the following architecture: Input layer (256×385) – Convolutional (Conv) layer (100×5×11) – Max-pooling layer (3×3) – Conv layer (100× 5×5) – Max-pooling layer (3×3) – Conv layer (64×5×5) – Full Connecting (FC) layer (600×1) – FC layer (3×1). A wide-shape kernel is chosen in the first convolutional layer aiming to extract more information of the scalogram and spectrogram along the time axis. The stride of the convolution operation in the first layer is (2×3), while that of the other convolutional layers is (1×1). Batch normalization [159] is used in each Conv and FC layers except the last FC layer. Dropout [139] is applied in the third Conv layer and the first FC layer to prevent over-fitting. Activation function used in the neural network is Rectified Linear Unit (ReLU). Finally, Cross-entropy is employed as the loss function.

5.5 Case Study and Experiments

5.5.1 Test Scenarios Configuration

Three test cases are chosen from [44] to generate harmonics, aiming to simulate interferences in real-life power grid operating conditions and to facilitate the performance evaluations: harmonic distortions, out-of-band interferences, and harmonics from nonlinear loads. The parameter specifications of the test power waveforms for CNN training are shown in Table. 5.1. Three transformer saturation scenarios (AC saturation, DC saturation, and non-saturation) are associated with four grid operating conditions (harmonic distortion, out-of-band interference, deployment of nonlinear loads, and normal operating condition). Therefore, 12 types of test waveforms are generated in total. All parameters are uniformly located in the

Table 5.1: Simulated Test Waveform Parameter Specification for GIC Experiment

Test Case	Saturation Type		
	AC	DC	NO
Saturation level	0.001pu-0.15pu	0.001pu-0.15pu	0
Harmonic Distortion	0.5 %-10 % THD; random choose up to 50^{th} order		
Out-of-Band	10Hz to 120Hz; level 0.01pu-0.1pu		
Nonlinear Load	1% to 20% of total load		
Normal	Waveform from normal operating condition		

Note: All generated signal has white Gaussian noise with same signal to noise ratio.

designated ranges. Each type of event occurs within a 20 ms simulation runtime window randomly and individually. The transformer saturation model for waveform generation is obtained according to Fig. 5.2. Each type of the test waveform includes 1,000 samples, and thus, a total of 12,000 samples (and wavelet scalogram and spectrogram) are simulated in the MATLAB environment, wherein 10,800 samples are used as the training dataset, 1,200 samples for validation, and 6,000 extra samples are generated for testing. All test waveforms are polluted by Gaussian noises at three levels of 20dB, 30dB, and 40dB to approximate the thermal and measurement noises in different conditions. For training the neural network, Adam [160] was employed as the optimizer, which has the initial learning rates of 1×10^{-3}, $\beta_1 = 0.9$, and $\beta_2 = 0.999$. The network was trained 120 epochs; in every 30 epochs, the learning rate decayed 1/10. The best validated model was recorded and tested.

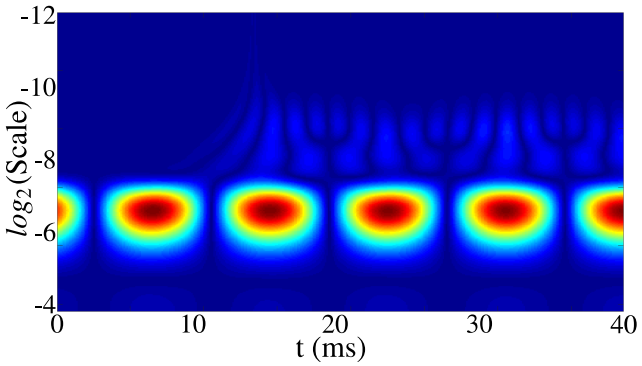

(a) Non-saturation with Harmonics in the grid

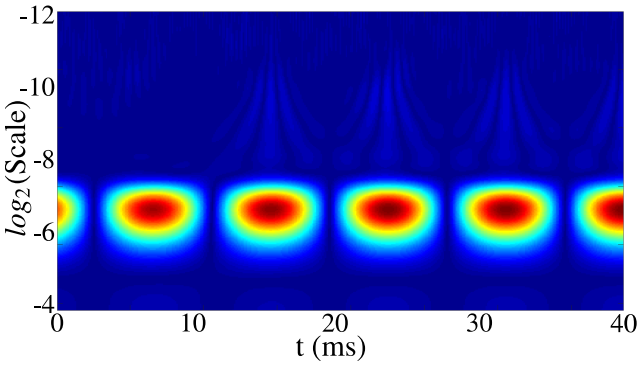

(b) AC saturation

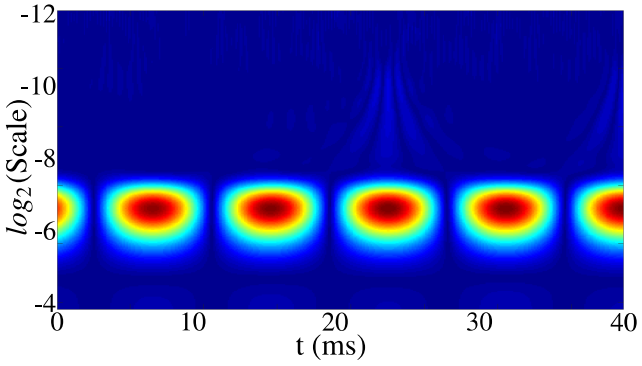

(c) DC saturation

Figure 5.5: Test waveform simulation results: (a) polluted with random harmonics; the AC (b) and DC (c) saturation level is 0.01 pu; all events start at t=10 ms.

5.5.2 Experimental Results and Analysis

Three patterns generated by PCWT for AC and DC saturation scenarios plus non-saturation condition are demonstrated in Fig. 5.5. One can see

that the scalograms generated by the proposed PCWT successfully reveal unique features in such scenarios: Fig. 5.5(b) shows consistent spikes indicating a full-cycle saturation. Fig. 5.5(c) shows one spike only that stands for a half-cycle saturation caused by GICs. In real-world operating conditions, the patterns in Fig. 5.5(a) can definitely affect the classification results during AC and DC saturation. The reason lies in the fact that the patterns in Fig. 5.5(a) would overlap those in Fig. 5.5(b)(c), if harmonics and saturation occur at the same time. Therefore, the performance of CNN needs to be verified in such circumstances, in which the patterns are overlapped.

To verify the accuracy of the proposed solution under different GIC levels, a quantized test was conducted. The accuracy obtained from using PCWT, as well as using STFT, are compared with the proposed hybrid approach. The classification accuracy is tested for five quantized GIC intensity intervals shown in Table 5.2. The highest accuracy in each scenario among the three tested approaches is highlighted. One can see that with same SNR, the detection accuracy increases as the GIC level intensifies. The proposed hybrid framework has the highest accuracy when SNR is low and the GIC intensity is weak. When SNR is high, the proposed PCWT could achieve a desirable accuracy.

In total, the proposed framework successfully achieves the best performance even under low-intensity GICs, high harmonics, and elevated noises. Moreover, the accuracy is still desirable if only using the proposed PCWT as the feature extraction tool. The framework works sufficiently fast, achieving the detection results within 30 ms (20 ms wavelet window plus 6.8 ± 2.7 ms the processing time); therefore, the framework can be applied for such online monitoring applications in power transmission systems.

Table 5.2: Accuracy Performance of the Test Results

	GIC (pu)	0-0.03	0.03-0.06	0.06-0.09	0.09-0.12	0.12-0.15	Overall
20dB	PCWT*	83.53%	90.66%	90.71%	90.54%	90.62%	88.97%
	STFT	81.30%	90.34%	90.26%	90.38%	90.26%	88.32%
	Hybrid**	83.62%	90.68%	90.72%	90.55%	90.74%	88.99%
30dB	PCWT*	88.75%	91.17%	91.15%	91.22%	86.87%	90.38%
	STFT	87.47%	90.89%	91.02%	90.95%	90.95%	90.02%
	Hybrid**	88.77%	91.24%	91.28%	91.26%	91.30%	90.52%
40dB	PCWT*	90.47%	91.49%	91.53%	91.54%	91.22%	90.95%
	STFT	89.30%	91.22%	91.18%	91.26%	91.12%	90.45%
	Hybrid**	90.54%	91.47%	91.39%	91.53%	91.34%	90.92%

*:Proposed PCWT only. **:Proposed PCWT + STFT

5.6 Discussion and Conclusion

This chapter aimed to effectively detect GICs in power transmission systems during the GMD events. Our proposed approach consists of a hybrid feature extraction using Gaussian PCWT and STFT, and a CNN-based event detection mechanism. Experiments demonstrated that the proposed analytics achieved high-accuracy detection of GICs under different grid operating conditions. This framework would be installed within PMUs and/or other IEDs that can capture the power grid waveforms. The future work can focus on (i) applying the proposed framework to a variety of transformer saturation models, (ii) investigating the potential use of CNN or other machine learning algorithms for GICs measurements, and (iii) integrating the wavelet transformation into CNNs and simplifying the two-phase framework into one, to further improve its performance in real-time.

Chapter 6: Smart Sensor Technology for Power Grid Topology Change Detection

6.1 Abstract

Power system topology changes, realized either through unpredictable disturbances (faults) or transmission line switching actions in day-to-day operations, manifests itself via a number of waveforms that can be captured at the measurement points (substations) in the power grid [182–189]. The waveforms acquired by the PMUs and/or other intelligent electronic devices (IEDs) will potentially carry specific features corresponding to the event, thereby reflecting the dynamics of a network topology change. This chapter proposes a novel wavelet transform algorithm and implements the event detection mechanism from the smart sensor framework for online power network topology change detection, enabling situational awareness spatially and temporally from one single PMU. Test signals representing different prevailing conditions in the grid with and without a topology change event are generated and applied to the IEEE 30-bus test system. The results verify the accurate performance of the proposed event detection and classification mechanism for online applications.

6.2 Feature Extraction for Topology Change

6.2.1 Theoretical Foundation

The power network topology change will affect the admittance matrix and consequently the magnitude and phase angles. This change will reveal certain features and peculiarities. Note that the admittance matrix is unique

for a given network topology. Therefore, as the waveform features change when the system transition from one to another configuration, the topology change event can be detected and classified. Here, the three-phase waveform in the transmission system are typically assumed to be balanced, thus, to simplify the feature extraction process, the $\alpha\beta$-frame waveform (3.3) from Clarke transformation in in Section 3.3.1 is used to model the input signals.

The proposed wavelet performs a multi-resolution correlation calculation as described by (3.6) in Section 3.3.2. The PCWT can generally provide the frequency information through feature extraction of the power waveforms. The research in this chapter is inspired by the characteristics of narrow-bandwidth wavelets. A pass-bandwidth around the central frequency is framed: if the pass-bandwidth is wider on the high-frequency range, the high-frequency components especially appearing during transients can be easily captured and even amplified; consequently, the spectrum will show high-energy concentration in that range. In contrast, the pass-bandwidth needs to be narrow in the low-frequency range especially around the fundamental frequency, so only the fundamental frequency features can be captured. The proposed wavelet has the following format:

$$\Psi(t) = \underbrace{\frac{1/a}{cosh(2\mu\pi\frac{F_c}{a}t)}}_{\substack{\text{Vanishing} \\ \text{Component}}} \cdot \underbrace{cos(2\pi\frac{F_c}{a}t)}_{\substack{\text{Periodic} \\ \text{Component}}} . \tag{6.1}$$

where μ is a positive pass-bandwidth index; the larger the value of μ, the wider the pass-bandwidth will be. Equation (6.1) is then converted into a discrete format as follows:

$$\Psi[n] = \frac{1}{a}\frac{cos(2\pi T_s\frac{F_c}{a}n)}{cosh(2\mu\pi T_s\frac{F_c}{a}n)} \tag{6.2}$$

Four spectrum of the proposed wavelet bank for PCWT are demonstrated in Fig. 6.1. A proper value of F_c should be selected satisfying the Nyquist sampling theory; this is seen in Fig. 6.1 (b)-(c), where f is close to $\pm 1/2$. If F_c is larger than a threshold, aliasing occurs which will interfere the extracted features within [-1/2, -1/4] and [1/4, 1/2] in Fig. 6.1(d). A proper value of F_C and μ are crucial for successful feature extraction.

The PCWT process is then formulated as follows:

$$\begin{aligned} X_{\omega_k|a_k,b_k} &= \frac{1}{a_k}\sum_{n=0}^{W-1} x_{\alpha\beta}[n]\Psi^*[\frac{nT_s - b_k}{a_k}] \\ &= \frac{1}{a_k}\sum_{n=0}^{W-1} \frac{|V_{\alpha\beta}[n]|e^{j(2\pi T_s f_0 n+\theta)}cos(2\pi T_s\frac{F_c}{a_k}n)}{cosh(2\mu\pi T_s\frac{F_c}{a_k}n)} \end{aligned} \tag{6.3}$$

$$\begin{aligned} X_{\omega_k|a_k,b_k=0} &= \frac{1}{a_k}\sum_{n=0}^{W-1} \frac{V_{\alpha\beta}[n]e^{j(2\pi T_s f_0 n+\theta)}[e^{j(2\pi T_s\frac{F_c}{a_k}n)} + e^{-j(2\pi T_s\frac{F_c}{a_k}n)}]}{2cosh(2\mu\pi T_s\frac{F_c}{a_k}n)} \\ &= \frac{1}{a_k}\sum_{n=0}^{W-1} \frac{V_{\alpha\beta}[n]e^{j(2\pi T_s(f_0+\frac{F_c}{a_k})n+\theta)}}{2cosh(2\mu\pi T_s\frac{F_c}{a_k}n)} + \frac{1}{a_k}\sum_{n=0}^{W-1} \frac{V_{\alpha\beta}[n]e^{j(2\pi T_s(f_0-\frac{F_c}{a_k})n+\theta)}}{2cosh(2\mu\pi T_s\frac{F_c}{a_k}n)} \end{aligned} \tag{6.4}$$

expanding (6.3) with all $b_k = 0$, it can be rewritten as in (6.4). Analytically, the window size W must have sufficient length, and thus, the first summation in (6.4) plays less of an impact on the energy "spectrum" than $|f_0 - \frac{F_c}{a}|$, since,

$$|f_0 + \frac{F_c}{a_k}| > |f_0 - \frac{F_c}{a_k}| \geq 0 \tag{6.5}$$

when $f_0 = F_c/a_k$, the PCWT will result in the highest correlation coefficients with respect to the targeted waveform.

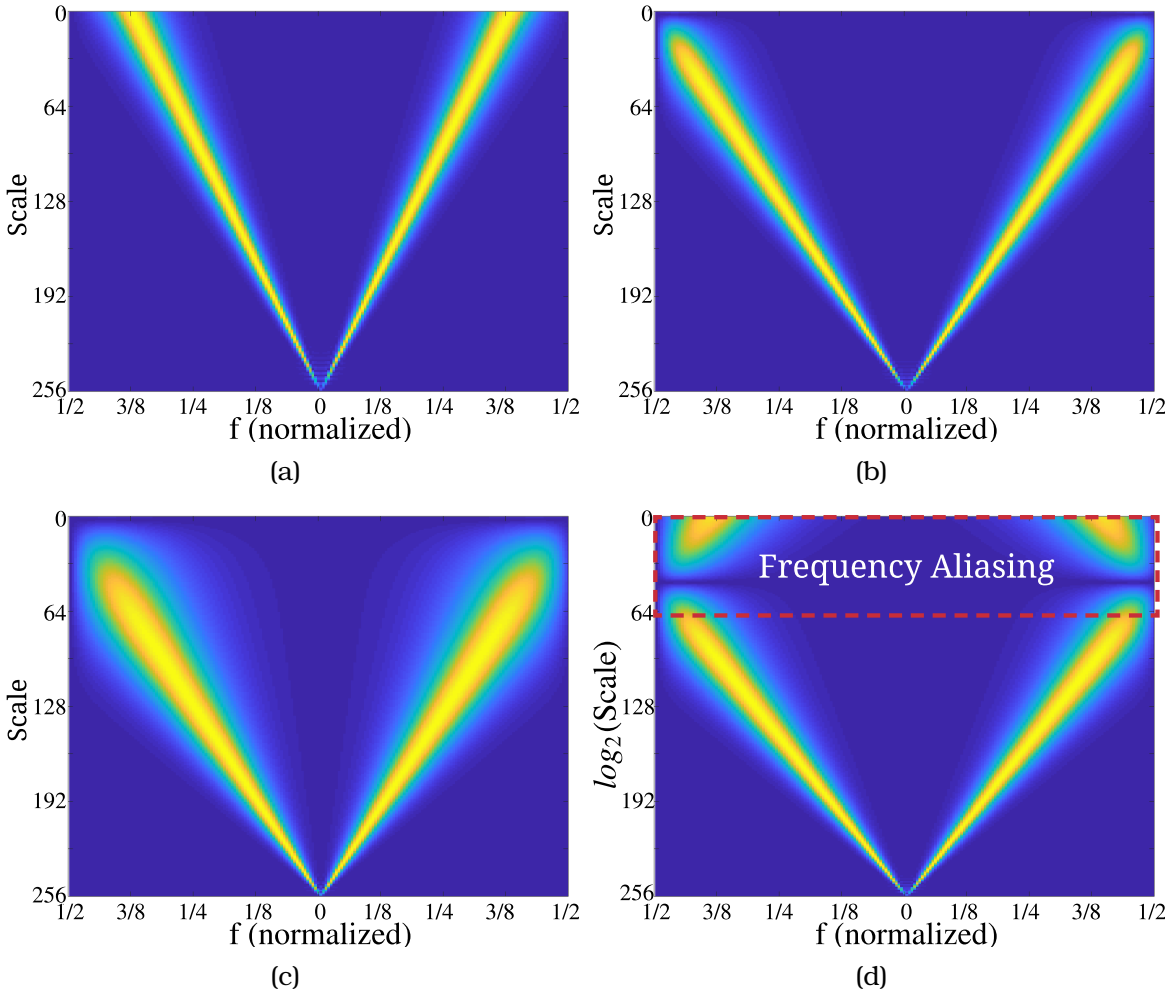

Figure 6.1: Spectrum of the proposed wavelets for online feature extraction; (a) $F_c = 0.375/Ts$, $\mu = 8$ (b) $F_c = 0.5/Ts$, $\mu = 8$ (c) $F_c = 0.5/Ts$, $\mu = 4$ (d) $Fc = 0.6/Ts$, $\mu = 4$.

6.2.2 Transformation of 1-D PCWT to the PCQ-WT

The time-domain $\alpha\beta$ components will be utilized to generate a complex-time signal as presented in (6.3) and (6.4). In order to ensure an effective feature extraction, the periodic component can be rewritten as a unit rotating phasor in (6.1), thus the proposed PCQ-WT is achieved as presented in (6.6).

$$\Psi[n] = \frac{1}{a_k} \frac{e^{j2\pi T_s(\frac{F_c}{a_k})n}}{cosh(2\mu\pi T_s \frac{F_c}{a_k} n)} \tag{6.6}$$

Therefore, equation (6.4) can be further simplified as in (6.7).

$$X_{\omega_k|a_k,b_k=0} = \frac{1}{a_k}\sum_{n=0}^{W-1}\frac{V_{\alpha\beta}[n]e^{j(2\pi T_s(f_0-\frac{F_c}{a_k})n+\theta)}}{cosh(2\mu\pi T_s\frac{F_c}{a_k}n)} \tag{6.7}$$

6.3 Numerical Case Studies

6.3.1 Critical Assumptions

This chapter proposed a novel wavelet transform to extract and classify unique features of the input power waveforms of a PMU and correlate them with topology change events. The sampling frequency in this chapter is $9600Hz$; therefore, the maximum central frequency of the proposed mother wavelet is $4800Hz$. Usually up to 50^{th} order of harmonics is considered in power system analysis; therefore, a frequency spectrum ranging from $1Hz$ to $3000Hz$—which is 0.75 times the theoretical maximum central frequency—is considered; hence, $F_c = 3000Hz$. To match the frequency spectrum, the scaling factor should ideally be [1, 3000]. However, simultaneous computation of 3000 PCWT is computationally-demanding. Therefore, conducting a down-sampling in the above frequency range is much preferred. The input signal has normally the most energy concentration in the low-frequency range, while high-frequency components will appear during transients. Hence, a dyadic scaling factor ranging $[1,256]$, i.e., $2^{[0,8]}$, is sufficient. A total of 256 samples of exponents are uniformly selected and the scaling factor set is formed.

6.3.2 Test System and Test Cases

In order to evaluate the wavelet performance, the frequency information and patterns extracted from the input waveforms are visualized and

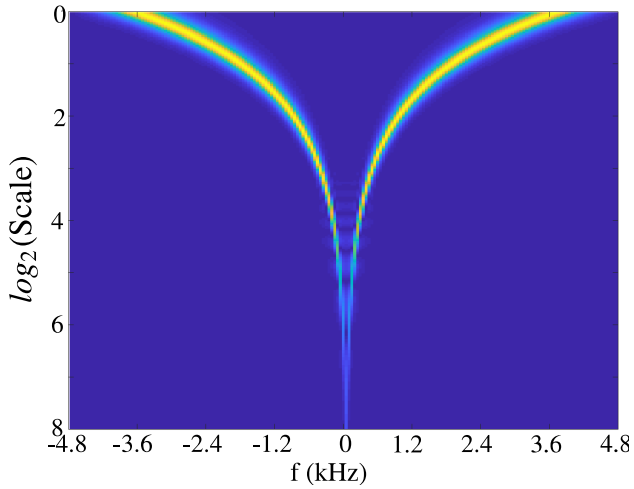

Figure 6.2: Spectrum of the proposed wavelet bank, where the scaling factor is plotted by log_2.

plotted in the time domain. The IEEE 30-bus test system (shown in Fig. 6.3) is selected as the test platform. The waveforms are generated from PSCAD/EMTDC using system configuration in [190] with simulation step-size of 6μs and then down-sampled to $9.6kHz$. The numerical evaluations are conducted on the following aspects: (i) waveform feature extraction during topology change in the system normal operating condition, and (ii) waveform feature extraction when a fault occurs following a topology change action. Measurements are acquired from the PMU located at Bus 6. The computation efficiency of the proposed wavelets is evaluated by measuring the time when the event occurs and that when a deformed pattern is detected. The following test cases are studied:

- *Test Case 1*: Transmission line (TL)2-4 and TL2-5 are switched-off, in two separate scenarios, when the system is in its normal operating condition.

- *Test Case 2*: A 3-phase fault occurred at $t = 30ms$, following a topology change by disconnecting TL2-4.

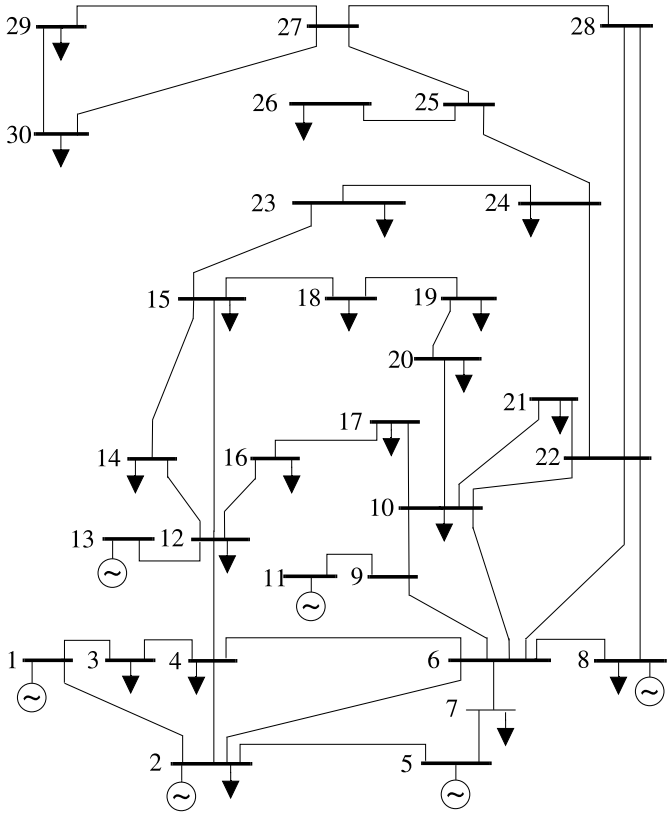

Figure 6.3: Single line diagram of IEEE 30 Bus system.

6.3.3 Results and Discussions

The frequency response of the PCWT wavelet bank, used for feature extraction in the experiments, is demonstrated in Fig. 6.2. In Fig. 6.4 (a)-(b), features reveal the maximum energy concentration on the fundamental frequency. The magnitude of this energy concentration remains almost constant during both topology change practices. However, when selecting smaller scaling factors (higher frequency range), the features can be obviously differentiated. In Fig. 6.4, one can observe a larger energy concentration on the high-frequency range in (a) than (b). Two energy peaks are observed in 4(a), one greater than the other. In Fig. 6.4(b), the extracted feature corresponding to the topology change action is still obvious. It takes 10ms to reveal the significant features in both scenarios.

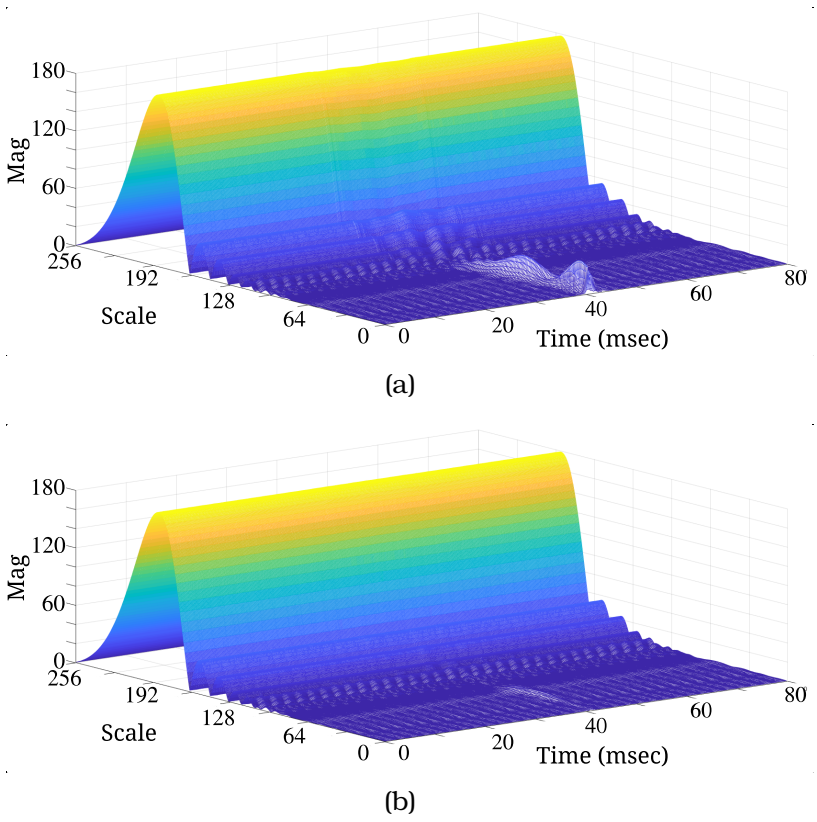

Figure 6.4: Simulation results in Test Case 1 where (a) TL2-4 is switched-off at $t = 30ms$, (b) TL2-5 is switched-off at $t = 30ms$.

The Test Case 2 results are demonstrated in Fig. 6.5. The energy spectrum shows the fault features almost instantaneously in both Fig. 6.5 (a), (b). While it may be hard to visually realize the differences in Fig. 6.5 (a) and (b), one can see in Fig. 6.5 (c) that, different features are captured when two different topologies are realized, when an exact same fault appears at the same time and location (Bus 15). Based on the experiments, one may expect the possibility that different topology changes, in certain conditions, may show *similar* signatures in the data. Furthermore, the developed pattern recognition mechanism offers a promising computational performance, making it suitable for online applications.

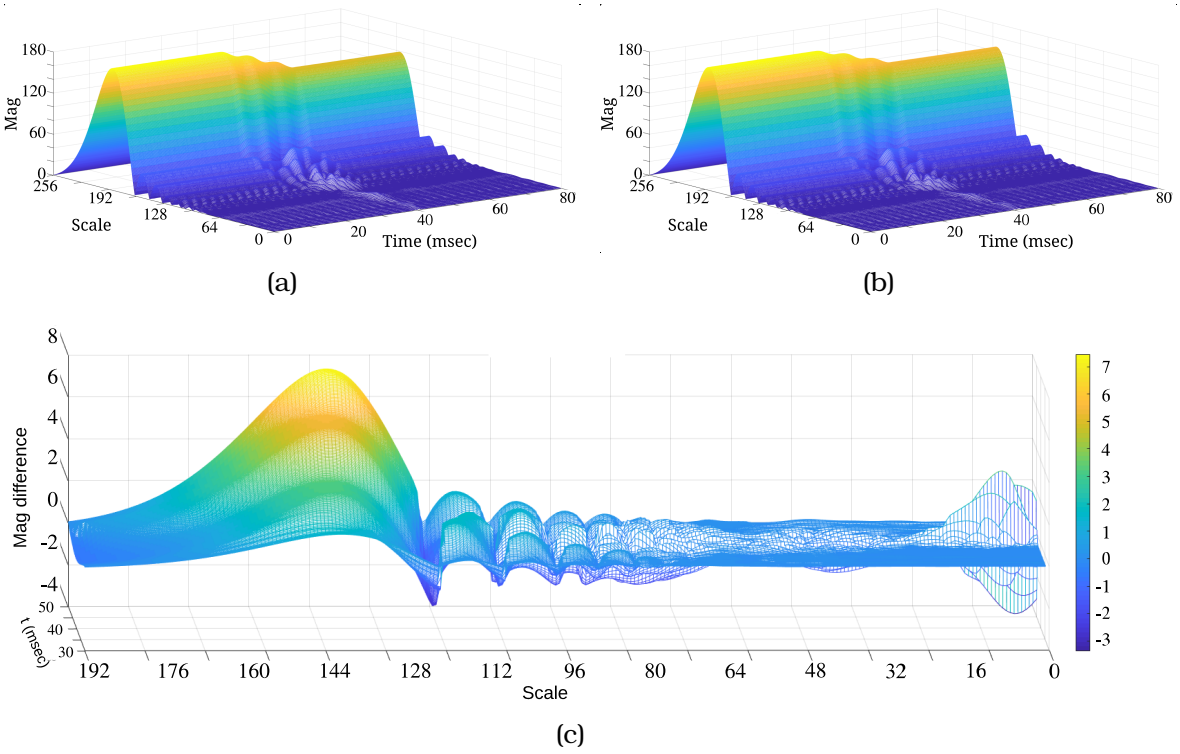

Figure 6.5: Simulation results in Test Case 2 where 3-phase fault happens at $t = 30ms$ at Bus 15 (a) during normal operation; (b) after TL 2-4 is switched-off; (c) feature difference.

6.4 Conclusion

This chapter introduced a novel multi-resolution wavelet transform, i.e., the PCQ-WT, for online topology change detection and classification in power systems. The proposed approach could successfully capture unique patterns and peculiarities associated with a network topology change, either through faults or transmission topology control practices or both. The waveform classification outcome can be leveraged within PMUs, and other IEDs with PMU functionality, to archive a fast and accurate topology change detection. The performance of the proposed algorithm, in terms of feature extraction accuracy and computation time efficiency, was verified under multiple test cases representing different operating conditions in an IEEE standard test system. Future work may include the performance evaluation of the proposed analytics for topology change detection in power grids under a wide range of uncertainties [191–201] and in presence of distributed energy resources [202, 202–211] and grid-support services [212–220].

Chapter 7: Dissertation Conclusion

7.1 Summary

Chapter 2 first introduced the concept of power grid resilience and then reviewed the existing literature on synchrophasor technology and power grid event detection. The literature review on event detection mechanisms included techniques through both conventional measurements and synchrophasor technology. Meanwhile, several SEAs were presented and their core principles were discussed.

In Chapter 3, details of the proposed smart sensor technology for distributed event detection and enhanced phasor measurement functionalities was introduced. The proposed smart sensor solution utilizes sampled waveform data through the existing A2D modules and extracts the signatures (features) within the electrical waveforms via an advanced PCQ-WT technique. A machine learning mechanism, i.e., the convolutional neural network, was developed and installed to detect and classify different events in the power system based on the extracted features. Meanwhile, the proposed smart sensor is housed with an adaptive SEA selection mechanism, that is expected to ensure high-fidelity synchrophasor measurements at all times. The performance of the proposed analytics was numerically evaluated under a variety of simulated events and power grid operating conditions. Numerical analyses demonstrated the superiority of the proposed framework in ensuring an online situational awareness in power grids with high-fidelity measurements at all times.

In Chapter 4, we explored the application of the proposed sensor technology on HIF detection. This chapter aimed at avoiding the damaging

consequences of HIFs thereby improving the electrical safety and validating this proposed technology in a specific high-level event detection application. In so doing, a modified core detection engine through a compact and efficient CNN structure was developed to process the extracted features from the current waveforms and detect the HIF events. Experiment results from a variety of simulated conditions demonstrated that the proposed analytics successfully achieved an ultra-fast and accurate HIF detection performance even under noisy measurements.

In Chapter 5, the impact modeling of GIC events is first introduced, and then an enhanced event detection engine combined with a hybrid time-frequency analysis through STFT and PCWT is developed for GIC detection in the power grid.

In Chapter 6, we explored the application of the proposed sensor technology in detecting the power grid topology change events. In so doing, a novel pseudo continuous quadrature wavelet transform was developed for the grid topology change detection. Detailed analysis and case studies were presented to demonstrate the feasibility of this new approach.

7.2 Contributions

With the widespread deployment of synchrophasor technology in modern power grids, system monitoring and control settings have been revolutionized into a new era with high-resolution measurements. To achieve an enhanced situational awareness in modern power grids, this dissertation presented an innovative next-generation smart sensor technology through a series of embedded data-driven analytics and the edge computing capabilities. The proposed sensor technology ensures a fast and accurate event detection and classification performance and high-fidelity synchrophasor measurements

under a variety of system operating conditions.

The dissertation contributions are as follows:

- The proposed framework transforms the existing centralized monitoring and control paradigms to distributed intelligence for online situational awareness in power grids.
- Enabling fusing the online measurements and grid monitoring in a distributed manner can greatly reduce the potential risks to communication failures, delays/latencies, and cyber-attacks.
- The proposed smart sensor solution can fully unlock the potential of edge computing capabilities in the intelligent electric devices installed in power grids.
- Three main stages of feature extraction, event detection and classification, and SEA selection are introduced to form the architecture of the next generation smart sensors.
- A wavelet approach for power waveform feature extraction is developed which provides satisfactory pattern recognition performance. Also, this WT is suitable to be applied on both single-phase and quadrature waveforms.
- An efficient CNN architecture is developed for high accuracy and low latency event detection and classification applications. The suggested CNN architecture can be extended for additional types of events if more labeled data samples are available in the waveform signature pool.
- New P-Class and M-Class synchrophasor estimation algorithms were proposed, a hybrid of which could ensure fast and high-fidelity synchrophasor measurements.

- The suggested data-driven solution technology with embedded analytics can be installed into the existing PMUs at no or very minimum costs and adjustments, thereby ensuring its interoperability with the existing setups in practice.

7.3 Suggestions for Future Research

Future research can be focused on investigating the event detection and assessing the severity of the detected event through CNNs or other machine learning algorithms. Also, one could approach integrating the feature extraction functionality within the machine learning technique to achieve an even more compact solution. The forecasting functionality can be added to the proposed framework to predict and quickly detect the long-lasting and slow dynamic events such as the Sub-Synchronous Resonance (SSR) phenomenon in wind turbines. When the proposed event detection and localization function is embedded into the PMUs, protective relays, and/or other IEDs, hardware-in-the-loop performance analysis can be conducted to verify and validate this concept in real-time operation conditions.

7.4 Publications

Under Review Journal Articles:

[1] **S. Wang** and P. Dehghanian, “On the Use of Artificial Intelligence for High Impedance Fault Detection and Electrical Safety,” *IEEE Transactions on Industry Applications*, 2020, (Under Review).

[2] **S. Wang**, P. Dehghanian, and L. Li, “Distributed Intelligence for Online Situational Awareness in Power Grids — Part I: Theory,” *IEEE Transactions on Power Systems*, 2020, (Under Review).

[3] **S. Wang**, P. Dehghanian, and L. Li, “Distributed Intelligence for Online Situational Awareness in Power Grids — Part II: Evaluations,” *IEEE Transactions on Power Systems*, 2020, (Under Review).

Published Journal Articles and Book Chapter:

[4] Y. Zhang, **S. Wang** and P. Dehghanian, “Big Data and Deep Learning Analytics for Robust PV Power Forecast in Smart Grids,” *Advanced Technologies for Solar Photovoltaics Energy Systems*, Springer Nature, Accept for Publication, in Press, 2020.

[5] T. Nguyen,**S. Wang**, M. Alhazmi, M. Nazemi, A. Estebsari, P. Dehghanian, "Electric Power Grid Resilience to Cyber Adversaries: State of the Art,” *IEEE Access*, vol. 8, pp. 87592-87608. [5]

[6] **S. Wang**, A. Etemadi, and M. Doroslovački, “Adaptive Cascaded Delayed Signal Cancellation PLL for Three-Phase Grid under Unbalanced and Distorted Condition,” *Electric Power Systems Research*, Volume 180, 2020, 106165, ISSN 0378-7796. [21]

[7] **S. Wang**, P. Dehghanian, and L. Li, "Power Grid Online Surveillance through PMU-Embedded Convolutional Neural Networks," *IEEE Transactions on Industry Applications*, vol. 56, no. 2, pp. 1146-1155, March-April 2020. [52]

[8] **S. Wang**, P. Dehghanian, L. Li, and B. Wang, "A Machine Learning Approach to Detection of Geomagnetically-Induced Currents in Power Grids," *IEEE Transactions on Industry Applications*, vol. 56, no. 2, pp. 1098-1106, March-April 2020. [50]

[9] B. Wang, P. Dehghanian, **S. Wang**, and M. Mitolo, Electrical Safety Considerations in Large-Scale Electric Vehicle Charging Stations," *IEEE Transactions on Industry Applications*, vol. 55, no. 6, pp. 6603-6612, Nov./Dec. 2019. [216]

[10] M. Alhazmi, P. Dehghanian, **S. Wang**, and B. Shinde, "Power Grid Optimal Topology Control Considering Correlations of System Uncertainties," *IEEE Transactions on Industry Applications*, vol. 55, no.6, pp. 5594-5604, Nov./Dec. 2019. [188]

[11] **S. Wang**, P. Dehghanian, M. Alhazmi, and M. Nazemi, "Advanced Control Solutions for Enhanced Resilience of Modern Power-Electronic-Interfaced Distribution Systems," *Journal of Modern Power Systems and Clean Energy*, vol. 7, no. 4, pp.716-730, July 2019. [46]

Conference Proceedings:

[13] M. Babakmehr, F. Harirchi, M. Nazir, **S. Wang**, P. Dehghanian, and J. Enslin, "Sparse Representation-based Classification of Geomagnetically Induced Currents," *Clemson University Power Systems Conference*, March 2020, Clemson SC, USA. [61]

[14] B. Shinde, **S. Wang**, P. Dehghanian, and M. Babakmehr, "Real-Time Detection of Critical Generators in Power Systems: A Deep Learning HCP Approach," *The 4th IEEE Texas Power and Energy Conference (TPEC)*, pp. 1-6, Feb. 2020, College Station, Texas, USA. [104]

[15] D. Wang, Y. Li, P. Dehghanian, **S. Wang**, "Power Grid Resilience to Electromagnetic (EMP) Disturbances: A Literature Review," *The 51st North American Power Symposium (NAPS)*, Oct. 2019, Wichita, Kansas, USA. [56]

[16] B. Wang, P. Dehghanian, D. Hu, **S. Wang**, and F. Wang, "Adaptive Operation Strategies for Electric Vehicle Charging Stations," *IEEE Industry Applications Society (IAS) Annual Meeting*, Sept.-Oct. 2019, Baltimore, Maryland, USA. [219]

[17] **S. Wang**, P. Dehghanian, L. Li, and B. Wang, "A Machine Learning Approach to Detection of Geomagnetically-Induced Currents in Power Grids," *IEEE Industry Applications Society (IAS) Annual Meeting*, Sept.-Oct. 2019, Baltimore, Maryland, USA. [48]

[18] **S. Wang**, L. Li, and P. Dehghanian, "Power Grid Online Surveillance through PMU-Embedded Convolutional Neural Networks," *IEEE Industry Applications Society (IAS) Annual Meeting*, Sept.-Oct. 2019, Baltimore, Maryland, USA. [49]

[19] M. Alhazmi, P. Dehghanian, **S. Wang**, and B. Shinde, "Power Grid Optimal Topology Control Considering Correlations of System Uncertainties," *IEEE/IAS 55th Industrial and Commercial Power Systems (I&CPS) Technical Conference*, May 2019, Calgary, Canada. [184]

[20] **S. Wang**, P. Dehghanian, B. Zhang, "A Data-Driven Algorithm for

Online Power Grid Topology Change Identification with PMUs," *IEEE Power and Energy Society (PES) General Meeting*, 4-8 August 2019, Atlanta, Georgia, USA. [47]

[21] **S. Wang**, P. Dehghanian, Y. Gu, "A Novel Multi-Resolution Wavelet Transform for Online Power Grid Waveform Classification," *The 1st IEEE International Conference on Smart Grid Synchronized Measurements and Analytics (SGSMA)*, 20-23 May 2019, College Station, Texas, USA. [51]

[22] **S. Wang**, P. Dehghanian, M. Alhazmi, J. Su, and B. Shinde, "Resilience-Assured Protective Control of DC/AC Inverters under Unbalanced and Fault Scenarios," *The 10th IEEE Power and Energy Society (PES) Conference on Innovative Smart Grid Technologies-North America (ISGT-NA)*, 18-21 Feb. 2019, Washington DC, USA. [66]

[23] M. H. Rezaeian Koochi, P. Dehghanian, S. Esmaeili, P. Dehghanian, and **S. Wang**, "A Synchrophasor-based Decision Tree Approach for Identification of Most Coherent Generating Units," *The 44th Annual Conference of the IEEE Industrial Electronics Society (IECON)*, Oct. 2018, Washington DC, USA. [11]

Bibliography

[1] ERC. Phasor measurement unit for monitoring power systems, *PHOENIX project*, European electrical power energy systems (EPES). https://phoenix-h2020.eu/phasor-measurement-unit\-for-monitoring-power-systems/. (last accessed: 07.22.2020).

[2] Leonardo Ulises Iurinic, A Ricardo Herrera-Orozco, Renato Goncalves Ferraz, and Arturo Suman Bretas. Distribution systems high-impedance fault location: A parameter estimation approach. *IEEE Transactions on Power Delivery*, 31(4):1806–1814, 2015.

[3] Qiushi Cui and Yang Weng. Enhance high impedance fault detection and location accuracy via *mu*-PMUs. *IEEE Transactions on Smart Grid*, 11(1):797–809, 2019.

[4] NERC, "2015 risk element: extreme physical events". http://www.nerc.com/pa/comp/Documents/2015%20Extreme%20Physical%20Events%20v1.08.pdf, Oct 15 2015.

[5] Tien Nguyen, Shiyuan Wang, Mohannad Alhazmi, Mostafa Nazemi, A Estebsari, and Payman Dehghanian. Electric power grid resilience to cyber adversaries: State of the art. *IEEE Access*, 8:87592–87608, 2020.

[6] Payman Dehghanian, Bei Zhang, Tatjana Dokic, and Mladen Kezunovic. Predictive risk analytics for weather-resilient operation of electric power systems. *IEEE Transactions on Sustainable Energy*, 10(1):3–15, 2019.

[7] Optimal allocation of PV generation and battery storage for enhanced resilience. *IEEE Transactions on Smart Grid*, 10(1):535–545, 2017.

[8] Payman Dehghanian. *Power System Topology Control for Enhanced Resilience of Smart Electricity Grids*. PhD thesis, Department of Electrical and Computer Engineering, Texas A&M University, College Station, Texas, USA, 2017.

[9] Gary Klein, Brian Moon, and Robert R Hoffman. Making sense of sensemaking 1: Alternative perspectives. *IEEE intelligent systems*, 21(4):70–73, 2006.

[10] J. A. de la O Serna. Synchrophasor measurement with polynomial phase-locked-loop Taylor–Fourier filters. *IEEE Transactions on Instrumentation and Measurement*, 64(2):328–337, Feb 2015.

[11] M. H. Rezaeian Koochi et al. A synchrophasor-based decision tree approach for identification of most coherent generating units. In *Annual Conference of the IEEE Industrial Electronics Society (IECON)*, pages 71–76, Oct 2018.

[12] T. Becejac, P. Dehghanian, and M. Kezunovic. Analysis of PMU algorithm errors during fault transients and out-of-step disturbances. In *IEEE PES Transmission & Distribution Conference and Exposition-Latin America*, pages 1–6, 2016.

[13] Tamara Becejac and Payman Dehghanian. PMU multilevel end-to-end testing to assess synchrophasor measurements during faults. *IEEE Power and Energy Technology Systems Journal*, 6(1):71–80, March 2019.

[14] Tamara Becejac, Payman Dehghanian, and Mladen Kezunovic. Impact of PMU errors on the synchrophasor-based fault location algorithms. In *48th North American Power Symposium (NAPS)*, pages 1–6, 2016.

[15] Mladen Kezunovic, Payman Dehghanian, and J Sztipanovits. An incremental system-of-systems integration modelling of cyber-physical electric power systems. In *Grid of the Future Symposium, CIGRE US National Committee*, pages 1–6. CIGRE, 2016.

[16] N. H. Abbasy and H. M. Ismail. A unified approach for the optimal PMU location for power system state estimation. *IEEE Transactions on Power Systems*, 24(2):806–813, May 2009.

[17] S. Chakrabarti, E. Kyriakides, and D. G. Eliades. Placement of synchronized measurements for power system observability. *IEEE Transactions on Power Delivery*, 24(1):12–19, Jan 2009.

[18] P Zhang, J Chen, and M Shao. Phasor measurement unit (pmu) implementation and applications. *Electr. Power Res. Inst. EPRI, Rep. Final 2007*, 2007.

[19] D. Macii, D. Petri, and A. Zorat. Accuracy analysis and enhancement of DFT-based synchrophasor estimators in off-nominal conditions. *IEEE Transactions on Instrumentation and Measurement*, 61(10):2653–2664, Oct 2012.

[20] Junqi Liu et al. Fundamental and harmonic synchrophasors estimation using modified Taylor-Kalman filter. In *IEEE International Workshop on Applied Measurements for Power Systems (AMPS)*, pages 1–6, 2012.

[21] Shiyuan Wang, Amir Etemadi, and Miloš Doroslovački. Adaptive cascaded delayed signal cancellation PLL for three-phase grid under

unbalanced and distorted condition. *Electric Power Systems Research*, 180:1–13, 2020.

[22] Vladimir V Terzija, Milenko B Djuric, and Branko D Kovacevic. Voltage phasor and local system frequency estimation using Newton type algorithm. *IEEE Transactions on Power Delivery*, 9(3):1368–1374, 1994.

[23] M. Chen et al. Positive sequence detector based on cascaded delayed quadrature signal cancellation. In *2015 IEEE Energy Conversion Congress and Exposition (ECCE)*, pages 1089–1094, Sept 2015.

[24] S. Golestan and J. M. Guerrero. Conventional synchronous reference frame phase-locked loop is an adaptive complex filter. *IEEE Transactions on Industrial Electronics*, 62(3):1679–1682, 2015.

[25] IEEE standard for synchrophasor measurements for power systems. *IEEE Std C37.118.1-2011 (Revision of IEEE Std C37.118-2005)*, pages 1–61, Dec 2011.

[26] Prashant Kansal and Anjan Bose. Bandwidth and latency requirements for smart transmission grid applications. *IEEE Transactions on Smart Grid*, 3(3):1344–1352, 2012.

[27] S. Mousavian, J. Valenzuela, and J. Wang. A probabilistic risk mitigation model for cyber-attacks to pmu networks. *IEEE Transactions on Power Systems*, 30(1):156–165, Jan 2015.

[28] Adrian Z Amanci and Francis P Dawson. Synchronization system with zero-crossing peak detection algorithm for power system applications. In *International Power Electronics Conference*, pages 2984–2991, 2010.

[29] S. Das and T. Sidhu. Robust algorithm to estimate fault synchrophasor from fault-transient synchrophasor in phasor data concentrator. *IET Generation, Transmission Distribution*, 9(2):124–132, 2015.

[30] Álvaro Ortega and Federico Milano. Comparison of different PLL implementations for frequency estimation and control. In *18th IEEE International Conference on Harmonics and Quality of Power*, pages 1–6, 2018.

[31] P. K. Dash, K. R. Krishnanand, and M. Padhee. Fast recursive Gauss-Newton adaptive filter for the estimation of power system frequency and harmonics in a noisy environment. *IET Generation, Transmission Distribution*, 5(12):1277–1289, December 2011.

[32] A. J. Roscoe, I. F. Abdulhadi, and G. M. Burt. P and M class phasor measurement unit algorithms using adaptive cascaded filters. *IEEE Trans. on Power Delivery*, 28(3):1447–1459, July 2013.

[33] P. Romano and M. Paolone. Enhanced interpolated-DFT for synchrophasor estimation in FPGAs: Theory, implementation, and validation of a pmu prototype. *IEEE Transactions on Instrumentation and Measurement*, 63(12):2824–2836, Dec 2014.

[34] L. Xie, Y. Chen, and P. R. Kumar. Dimensionality reduction of synchrophasor data for early event detection: Linearized analysis. *IEEE Transactions on Power Systems*, 29(6):2784–2794, Nov 2014.

[35] Yang Chen, Le Xie, and PR Kumar. Dimensionality reduction and early event detection using online synchrophasor data. In *2013 IEEE Power & Energy Society General Meeting*, pages 1–5. IEEE, 2013.

[36] Daniele Carta, Andrea Benigni, and Carlo Muscas. Model order reduction for pmu-based state estimation in distribution grids. *IEEE Systems Journal*, 12(3):2711–2720, 2017.

[37] Phani Harsha Gadde, Milan Biswal, Sukumar Brahma, and Huiping Cao. Efficient compression of pmu data in wams. *IEEE transactions on smart grid*, 7(5):2406–2413, 2016.

[38] Yinyin Ge, Alexander J Flueck, Dae-Kyeong Kim, Jong-Bo Ahn, Jae-Duck Lee, and Dae-Yun Kwon. Power system real-time event detection and associated data archival reduction based on synchrophasors. *IEEE Transactions on Smart Grid*, 6(4):2088–2097, 2015.

[39] Jesmin Khan, Sharif Bhuiyan, Gregory Murphy, and Johnathan Williams. Data denoising and compression for smart grid communication. *IEEE Transactions on Signal and Information Processing over Networks*, 2(2):200–214, 2016.

[40] G. Lee and Y. Shin. Multiscale pmu data compression based on wide-area event detection. In *2017 IEEE International Conference on Smart Grid Communications (SmartGridComm)*, pages 437–442, Oct 2017.

[41] M. He, V. Vittal, and J. Zhang. Online dynamic security assessment with missing pmu measurements: A data mining approach. *IEEE Transactions on Power Systems*, 28(2):1969–1977, May 2013.

[42] P. Gao, M. Wang, S. G. Ghiocel, J. H. Chow, B. Fardanesh, and G. Stefopoulos. Missing data recovery by exploiting low-dimensionality in power system synchrophasor measurements. *IEEE Transactions on Power Systems*, 31(2):1006–1013, March 2016.

[43] X. A. Liu, D. Laverty, and R. Best. Islanding detection based on probabilistic pca with missing values in pmu data. In *2014 IEEE PES General Meeting | Conference Exposition*, pages 1–6, July 2014.

[44] T. Becejac, P. Dehghanian, and M. Kezunovic. Probabilistic assessment of PMU integrity for planning of periodic maintenance and testing. In *IEEE International Conference on Probabilistic Methods Applied to Power Systems (PMAPS)*, pages 1–6, 2016.

[45] C. Qian and M. Kezunovic. A power waveform classification method for adaptive synchrophasor estimation. *IEEE Transactions on Instrumentation and Measurement*, 67(7):1646–1658, July 2018.

[46] Shiyuan Wang, Payman Dehghanian, Mohannad Alhazmi, and Mostafa Nazemi. Advanced control solutions for enhanced resilience of modern power-electronic-interfaced distribution systems. *Journal of Modern Power Systems and Clean Energy*, 7(4):716–730, 2019.

[47] S. Wang, P. Dehghanian, and B. Zhang. A data-driven algorithm for online power grid topology change identification with PMUs. In *IEEE Power Energy Society General Meeting (PESGM)*, pages 1–5, Aug 2019.

[48] S. Wang, P. Dehghanian, L. Li, and B. Wang. A machine learning approach to detection of geomagnetically induced currents in power grids. In *2019 IEEE Industry Applications Society Annual Meeting*, pages 1–7, Sep. 2019.

[49] Shiyuan Wang, Li Li, and Payman Dehghanian. Power grid online surveillance through PMU-embedded convolutional neural networks. In *IEEE Industry Applications Society (IAS) Annual Meeting*, pages 1–7, 2019.

[50] Shiyuan Wang, Payman Dehghanian, Li Li, and Bo Wang. A machine learning approach to detection of geomagnetically induced currents in power grids. *IEEE Transactions on Industry Applications*, 56(2):1098–1106, 2019.

[51] Shiyuan Wang, Payman Dehghanian, and Yingzhong Gu. A novel multi-resolution wavelet transform for online power grid waveform classification. In *2019 International Conference on Smart Grid Synchronized Measurements and Analytics (SGSMA)*, pages 1–8. IEEE, 2019.

[52] Shiyuan Wang, Payman Dehghanian, and Li Li. Power grid online surveillance through PMU-embedded convolutional neural networks. *IEEE Transactions on Industry Applications*, 56(2):1146–1155, 2019.

[53] G Cauley and M Lauby. High-impact low-frequency event risk to the north american bulk power system. *NERC, Atlanta, GA, USA, Tech. Rep*, 2010.

[54] Arun Veeramany, Stephen D Unwin, Garill A Coles, Jeffery E Dagle, David W Millard, Juan Yao, Cliff S Glantz, and Sri NG Gourisetti. Framework for modeling high-impact, low-frequency power grid events to support risk-informed decisions. *International journal of disaster risk reduction*, 18:125–137, 2016.

[55] Jinshun Su, Payman Dehghanian, Mostafa Nazemi, and Bo Wang. Distributed wind power resources for enhanced power grid resilience. In *The 51st North American Power Symposium (NAPS)*, pages 1–6, 2019.

[56] Dingwei Wang, Yifu Li, Payman Dehghanian, and Shiyuan Wang. Power grid resilience to electromagnetic (EMP) disturbances: A literature review. In *The 51st North American Power Symposium (NAPS)*, pages 1–6, 2019.

[57] Pooria Dehghanian, Semih Aslan, and Payman Dehghanian. Maintaining electric system safety through an enhanced network resilience. *IEEE Transactions on Industry Applications*, 54(5):4927–4937, 2018.

[58] M. Nazemi, M. Moeini-Aghtaie, M. Fotuhi-Firuzabad, and P. Dehghanian. Energy storage planning for enhanced resilience of power distribution networks against earthquakes. *IEEE Transactions on Sustainable Energy*, 11(2):795–806, April 2020.

[59] Pooria Dehghanian, S Aslan, and Payman Dehghanian. Quantifying power system resiliency improvement using network reconfiguration. In *IEEE 60th International Midwest Symposium on Circuits and Systems (MWSCAS)*, pages 1–5, 2017.

[60] Zijiang Yang, Payman Dehghanian, and Mostafa Nazemi. Enhancing seismic resilience of electric power distribution systems with mobile power sources. In *IEEE Industry Applications Society (IAS) Annual Meeting*, pages 1–7, 2019.

[61] Mohammad Babakmehr, Farnaz Harirchi, Moazzam Nazir, Shiyuan Wang, Payman Dehghanian, and Johan Enslin. Sparse representation-based classification of geomagnetically induced currents. In *Clemson University Power Systems Conference*, pages 1–6, 2020.

[62] Zijiang Yang, Mostafa Nazemi, Payman Dehghanian, and Masoud Barati. Toward resilient solar-integrated distribution grids: Harnessing the mobility of power sources. In *IEEE Power and Energy Society (PES) Transmission and Distribution (T&D) Conference and Exposition*, pages 1–5, 2020.

[63] Mostafa Nazemi and Payman Dehghanian. Seismic-resilient bulk power grids: Hazard characterization, modeling, and mitigation. *IEEE Transactions on Engineering Management*, 67(3):614–630, Aug. 2020.

[64] Zijiang Yang, Payman Dehghanian, and Mostafa Nazemi. Seismic-resilient electric power distribution systems: Harnessing the mobility of power sources. *IEEE Transactions on Industry Applications*, 56(3):2304–2313, May/June 2020.

[65] Mostafa Nazemi, Payman Dehghanian, Mohannad Alhazmi, and Fei Wang. Multivariate uncertainty characterization for resilience planning in electric power systems. In *IEEE/IAS 56th Industrial and Commercial Power Systems (I&CPS) Technical Conference*, pages 1–7, 2020.

[66] Shiyuan Wang, Payman Dehghanian, Mohannad Alhazmi, Jinshun Su, and Bhavesh Shinde. Resilience-assured protective control of DC/AC inverters under unbalanced and fault scenarios. In *The 10th IEEE Power and Energy Society (PES) Conference on Innovative Smart Grid Technologies-North America (ISGT-NA)*, pages 1–5, 2019.

[67] Mohammad Babakmehr, Farnaz Harirchi, Payman Dehghanian, and Johan Enslin. Artificial intelligence-based cyber-physical event classification for islanding detection in power inverters. *IEEE Journal of Emerging and Selected Topics in Power Electronics*, pages 1–11, 2020.

[68] Pouya Jamborsalamati, MJ Hossain, S Taghizadeh, A Sadu, G Konstantinou, M Manbachi, and Payman Dehghanian. Enhancing power grid resilience through an IEC61850-based ev-assisted load restoration. *IEEE Transactions on Industrial Informatics*, 16(3):1799–1810, March 2020.

[69] Amin Gholami, Farrokh Aminifar, and Mohammad Shahidehpour. Front lines against the darkness: Enhancing the resilience of the electricity grid through microgrid facilities. *IEEE Electrification Magazine*, 4(1):18–24, 2016.

[70] Alfred R Berkeley, Mike Wallace, and Constellation Coo. A framework for establishing critical infrastructure resilience goals. *Final Report and Recommendations by the Council, National Infrastructure Advisory Council*, 2010.

[71] EPRI. Electric power system resiliency: challenges and opportunities. `https://www.naseo.org/Data/Sites/1/resiliency-white-paper.pdf`, Feb 2016. 3002007376.

[72] Engineering, National Academies of Sciences, Medicine, et al. *Enhancing the resilience of the nation's electricity system*. National Academies Press, 2017.

[73] Z. Li, M. Shahidehpour, F. Aminifar, A. Alabdulwahab, and Y. Al-Turki. Networked microgrids for enhancing the power system resilience. *Proceedings of the IEEE*, 105(7):1289–1310, 2017.

[74] Zhaohong Bie, Yanling Lin, Gengfeng Li, and Furong Li. Battling the extreme: A study on the power system resilience. *Proceedings of the IEEE*, 105(7):1253–1266, 2017.

[75] H Mirsaeedi, A Fereidunian, S. M. Mohammadi-Hosseininejad, Payman Dehghanian, and Hamid Lesani. Long-term maintenance scheduling and budgeting in electricity distribution systems equipped with automatic switches. *IEEE Transactions on Industrial Informatics*, 14(5):1909–1919, 2018.

[76] M Asghari Gharakheili, Mahmud Fotuhi-Firuzabad, and Payman Dehghanian. A new multi-attribute support tool for identifying critical components in power transmission systems. *IEEE Systems Journal*, 12(1):316–327, 2018.

[77] F Pourahmadi, Mahmud Fotuhi-Firuzabad, and Payman Dehghanian. Application of game theory in reliability centered maintenance of electric power systems. *IEEE Transactions on Industry Applications*, 53(2):936–946, 2017.

[78] F Pourahmadi, Mahmud Fotuhi-Firuzabad, and Payman Dehghanian. Identification of critical generating units for maintenance: A game theory approach. *IET Generation, Transmission & Distribution*, 10(12):2942–2952, 2016.

[79] Hamed Sabouhi, Ali Abbaspour, Mahmud Fotuhi-Firuzabad, and Payman Dehghanian. Identifying critical components of combined cycle power plants for implementation of reliability centered maintenance. *IEEE CSEE Journal of Power and Energy Systems*, 2(2):87–97, 2016.

[80] Hamed Sabouhi, Ali Abbaspour, Mahmud Fotuhi-Firuzabad, and Payman Dehghanian. Reliability modeling and availability analysis of combined cycle power plants. *International Journal of Electrical Power and Energy Systems*, 79:108–119, 2016.

[81] Rahim Ghorani, Mahmud Fotuhi-Firuzabad, Payman Dehghanian, and Wenyuan Li. Identifying critical component for reliability centered maintenance management of deregulated power systems. *IET Generation, Transmission, and Distribution*, 9(9):828–837, 2015.

[82] Payman Dehghanian, Mahmud Fotuhi-Firuzabad, Farrokh Aminifar, and Roy Billinton. A comprehensive scheme for reliability centered maintenance implementation in power distribution systems- part II: Numerical analysis. *IEEE Transactions on Power Delivery*, 28(2):771–778, 2013.

[83] Payman Dehghanian, Mahmud Fotuhi-Firuzabad, Farrokh Aminifar, and Roy Billinton. A comprehensive scheme for reliability centered maintenance implementation in power distribution systems- part I: Methodology. *IEEE Transactions on Power Delivery*, 28(2):761–770, 2013.

[84] Payman Dehghanian, Yufan Guan, and Mladen Kezunovic. Real-time life-cycle assessment of high voltage circuit breakers for maintenance using online condition monitoring data. *IEEE Transactions on Industry Applications*, 55(2):1135–1146, 2019.

[85] Payman Dehghanian, Mladen Kezunovic, Gurunath Gurrala, and Yufan Guan. Security-based circuit breaker maintenance management. In *IEEE Power and Energy Society (PES) General Meeting*, pages 1–5, 2013.

[86] Yufan Guan, Mladen Kezunovic, Payman Dehghanian, and Gurunath Gurrala. Assessing circuit breaker life cycle using condition-based data. In *IEEE Power and Energy Society (PES) General Meeting*, pages 1–5, 2013.

[87] Payman Dehghanian and Mladen Kezunovic. Cost/benefit analysis for circuit breaker maintenance planning and scheduling. In *The 45th North American Power Symposium (NAPS)*, pages 1–6, 2013.

[88] Payman Dehghanian, Yufan Guan, and Mladen Kezunovic. Real-time life-cycle assessment of circuit breakers for maintenance using online condition monitoring data. In *IEEE/IAS 54th Industrial and Commercial Power Systems (I&CPS) Technical Conference*, pages 1–8, 2018.

[89] Payman Dehghanian, Tomo Popovic, and Mladen Kezunovic. Circuit breaker operational health assessment via condition monitoring data. In *The 46th North American Power Symposium*, pages 1–6, 2014.

[90] F. A. S. Borges, R. A. S. Fernandes, I. N. Silva, and C. B. S. Silva. Feature extraction and power quality disturbances classification using smart meters signals. *IEEE Transactions on Industrial Informatics*, 12(2):824–833, April 2016.

[91] M. S. Manikandan, S. R. Samantaray, and I. Kamwa. Detection and classification of power quality disturbances using sparse signal decomposition on hybrid dictionaries. *IEEE Transactions on Instrumentation and Measurement*, 64(1):27–38, Jan 2015.

[92] D. P. Mishra, S. R. Samantaray, and G. Joos. A combined wavelet and data-mining based intelligent protection scheme for microgrid. *IEEE Transactions on Smart Grid*, 7(5):2295–2304, Sept 2016.

[93] K. Thirumala, M. S. Prasad, T. Jain, and A. C. Umarikar. Tunable-q wavelet transform and dual multiclass svm for online automatic detection of power quality disturbances. *IEEE Transactions on Smart Grid*, 9(4):3018–3028, July 2018.

[94] M. J. Reddy and D. K. Mohanta. Adaptive-neuro-fuzzy inference system approach for transmission line fault classification and location incorporating effects of power swings. *IET Generation, Transmission Distribution*, 2(2):235–244, 2008.

[95] W. Wang, L. He, P. Markham, H. Qi, Y. Liu, Q. C. Cao, and L. M. Tolbert. Multiple event detection and recognition through sparse unmixing for high-resolution situational awareness in power grid. *IEEE Transactions on Smart Grid*, 5(4):1654–1664, 2014.

[96] MM Eissa, M Elshahat Masoud, and M Magdy Mohamed Elanwar. A novel back up wide area protection technique for power transmission grids using phasor measurement unit. *IEEE Transactions on Power Delivery*, 25(1):270–278, 2009.

[97] Ching-Shan Chen, Chih-Wen Liu, and Joe-Air Jiang. A new adaptive pmu based protection scheme for transposed/untransposed parallel transmission lines. *IEEE Transactions on Power Delivery*, 17(2):395–404, 2002.

[98] Joseph Euzebe Tate and Thomas J Overbye. Line outage detection using phasor angle measurements. *IEEE Transactions on Power Systems*, 23(4):1644–1652, 2008.

[99] Joseph Euzebe Tate and Thomas J Overbye. Double line outage detection using phasor angle measurements. In *2009 IEEE Power & Energy Society General Meeting*, pages 1–5. IEEE, 2009.

[100] Y. Ge, A. J. Flueck, D. Kim, J. Ahn, J. Lee, and D. Kwon. Power system real-time event detection and associated data archival reduction based on synchrophasors. *IEEE Transactions on Smart Grid*, 6(4):2088–2097, July 2015.

[101] S. Liu, Y. Zhao, Z. Lin, Y. Liu, Y. Ding, L. Yang, and S. Yi. Data-driven event detection of power systems based on unequal-interval reduction of pmu data and local outlier factor. *IEEE Transactions on Smart Grid*, 11(2):1630–1643, 2020.

[102] A. Öner and M. Göl. Fault location based on state estimation in pmu observable systems. In *2016 IEEE Power Energy Society Innovative Smart Grid Technologies Conference (ISGT)*, pages 1–5, Sep. 2016.

[103] X. Liang, S. A. Wallace, and D. Nguyen. Rule-based data-driven analytics for wide-area fault detection using synchrophasor data. *IEEE Transactions on Industry Applications*, 53(3):1789–1798, May 2017.

[104] Bhavesh Shinde, Shiyuan Wang, Payman Dehghanian, and Mohammad Babakmehr. Real-time detection of critical generators in power systems: A deep learning hcp approach. In *2020 IEEE Texas Power and Energy Conference (TPEC)*, pages 1–6. IEEE, 2020.

[105] S. Nanda and P. K. Dash. A gauss–newton adaline for dynamic phasor estimation of power signals and its fpga implementation. *IEEE Transactions on Instrumentation and Measurement*, 67(1):45–56, 2018.

[106] C. Chen. A phasor estimator for synchronization between power grid and distributed generation system. *IEEE Transactions on Industrial Electronics*, 60(8):3248–3255, 2013.

[107] C. Huang, X. Xie, and H. Jiang. Dynamic phasor estimation through dstkf under transient conditions. *IEEE Transactions on Instrumentation and Measurement*, 66(11):2929–2936, 2017.

[108] P. Banerjee and S. C. Srivastava. An effective dynamic current phasor estimator for synchrophasor measurements. *IEEE Transactions on Instrumentation and Measurement*, 64(3):625–637, 2015.

[109] D. Lee, S. Kang, and S. Nam. Modified dynamic phasor estimation algorithm for the transient signals of distributed generators. *IEEE Transactions on Smart Grid*, 4(1):419–424, 2013.

[110] J. A. de la O Serna and J. Rodríguez-Maldonado. Taylor–Kalman–Fourier filters for instantaneous oscillating phasor and harmonic estimates. *IEEE Transactions on Instrumentation and Measurement*, 61(4):941–951, April 2012.

[111] J. A. de la O Serna. Dynamic phasor estimates for power system oscillations. *IEEE Transactions on Instrumentation and Measurement*, 56(5):1648–1657, 2007.

[112] M. A. P. a. J. Platas-Garza and J. A. de la O Serna. Dynamic phasor and frequency estimates through maximally flat differentiators. *IEEE Transactions on Instrumentation and Measurement*, 59(7):1803–1811, 2010.

[113] D. Belega, D. Fontanelli, and D. Petri. Low-complexity least-squares dynamic synchrophasor estimation based on the discrete fourier transform. *IEEE Transactions on Instrumentation and Measurement*, 64(12):3284–3296, 2015.

[114] P. Tosato, D. Macii, M. Luiso, D. Brunelli, D. Gallo, and C. Landi. A tuned lightweight estimation algorithm for low-cost phasor measurement units. *IEEE Transactions on Instrumentation and Measurement*, 67(5):1047–1057, 2018.

[115] M. Radulović, Ž. Zečević, and B. Krstajić. Dynamic phasor estimation by symmetric taylor weighted least square filter. *IEEE Transactions on Power Delivery*, 35(2):828–836, 2020.

[116] J. A. de la O Serna and J. Rodriguez-Maldonado. Instantaneous oscillating phasor estimates with taylor^k-kalman filters. *IEEE Transactions on Power Systems*, 26(4):2336–2344, 2011.

[117] M. Bertocco, G. Frigo, C. Narduzzi, C. Muscas, and P. A. Pegoraro. Compressive sensing of a taylor-fourier multifrequency model for synchrophasor estimation. *IEEE Transactions on Instrumentation and Measurement*, 64(12):3274–3283, Dec 2015.

[118] Kaiming He, Georgia Gkioxari, Piotr Dollár, and Ross Girshick. Mask R-CNN. In *IEEE International Conference on Computer Vision*, pages 2980–2988, 2017.

[119] R. H. Park. Two-reaction theory of synchronous machines generalized method of analysis–Part I. *Transactions of the American Institute of Electrical Engineers*, 48(3):716–727, July 1929.

[120] Hossein Farzin, Mahmud Fotuhi-Firuzabad, and Moein Moeini-Aghtaie. Enhancing power system resilience through hierarchical outage management in multi-microgrids. *IEEE Transactions on Smart Grid*, 7(6):2869–2879, 2016.

[121] D. P. Mishra, S. R. Samantaray, and G. Joos. A combined wavelet and data-mining based intelligent protection scheme for microgrid. *IEEE Transactions on Smart Grid*, 7(5):2295–2304, Sept 2016.

[122] Yi-Ching Su, Kuo-Lung Lian, and Hsueh-Hsien Chang. Feature selection of non-intrusive load monitoring system using STFT and wavelet transform. In *IEEE International Conference on e-Business Engineering (ICEBE)*, pages 293–298, 2011.

[123] Sheng-Huoo Ni, Kuo-Feng Lo, Lutz Lehmann, and Yan-Hong Huang. Time–frequency analyses of pile-integrity testing using wavelet transform. *Computers and Geotechnics*, 35(4):600–607, 2008.

[124] Christopher Torrence and Gilbert P Compo. A practical guide to wavelet analysis. *American Meteorological Society*, 79(1):61–78, 1998.

[125] Paul S Addison. *The illustrated wavelet transform handbook: introductory theory and applications in science, engineering, medicine and finance*. CRC press, 2017.

[126] Mallat Stephane. *A wavelet tour of signal processing*. Elsevier, 1999.

[127] S. Mallat and W. L. Hwang. Singularity detection and processing with wavelets. *IEEE Transactions on Information Theory*, 38(2):617–643, March 1992.

[128] Ian Goodfellow, Yoshua Bengio, and Aaron Courville. *Deep Learning*. MIT Press, 2016. `http://www.deeplearningbook.org`.

[129] Alex Krizhevsky, Ilya Sutskever, and Geoffrey E Hinton. Imagenet classification with deep convolutional neural networks. In *Advances in Neural Information Processing Systems*, pages 1097–1105, 2012.

[130] Karen Simonyan and Andrew Zisserman. Very deep convolutional networks for large-scale image recognition. *arXiv preprint*, (arXiv:1409.1556), 2014.

[131] Leon A Gatys, Alexander S Ecker, and Matthias Bethge. Image style transfer using convolutional neural networks. In *Proceedings of the IEEE Conference on Computer Vision and Pattern Recognition*, pages 2414–2423, 2016.

[132] Yoshua Bengio, Aaron Courville, and Pascal Vincent. Representation learning: A review and new perspectives. *IEEE Transactions on Pattern Analysis and Machine Intelligence*, 35(8):1798–1828, 2013.

[133] John S Bridle. Probabilistic interpretation of feedforward classification network outputs, with relationships to statistical pattern recognition. In *Neurocomputing*, pages 227–236. Springer, 1990.

[134] Zhengyou Zhang, M. Lyons, M. Schuster, and S. Akamatsu. Comparison between geometry-based and Gabor-wavelets-based facial expression recognition using multi-layer perceptron. In *Proceedings Third IEEE International Conference on Automatic Face and Gesture Recognition*, pages 454–459, April 1998.

[135] B. S. Manjunath and W. Y. Ma. Texture features for browsing and retrieval of image data. *IEEE Transactions on Pattern Analysis and Machine Intelligence*, 18(8):837–842, Aug 1996.

[136] J. V. B. Soares et al. Retinal vessel segmentation using the 2-D Gabor wavelet and supervised classification. *IEEE Transactions on Medical Imaging*, 25(9):1214–1222, Sept 2006.

[137] John Hubbard. Calculation of partition functions. *Physical Review Letters*, 3(2):77, 1959.

[138] J. A. de la O Serna. Dynamic phasor estimates for power system oscillations. *IEEE Transactions on Instrumentation and Measurement*, 56(5):1648–1657, Oct 2007.

[139] Nitish Srivastava, Geoffrey Hinton, Alex Krizhevsky, Ilya Sutskever, and Ruslan Salakhutdinov. Dropout: a simple way to prevent neural networks from overfitting. *The Journal of Machine Learning Research*, 15(1):1929–1958, 2014.

[140] A. Bhandari, H. Yin, Y. Liu, W. Yao, and L. Zhan. Real-time signal-to-noise ratio estimation by universal grid analyzer. In *2019 International Conference on Smart Grid Synchronized Measurements and Analytics (SGSMA)*, pages 1–6, 2019.

[141] P. Castello, J. Liu, C. Muscas, P. A. Pegoraro, F. Ponci, and A. Monti. A fast and accurate pmu algorithm for P+M class measurement of synchrophasor and frequency. *IEEE Transactions on Instrumentation and Measurement*, 63(12):2837–2845, Dec 2014.

[142] Muhammad Sarwar, Faisal Mehmood, Muhammad Abid, Abdul Qayyum Khan, Sufi Tabassum Gul, and Adil Sarwar Khan. High impedance fault detection and isolation in power distribution networks using support vector machines. *Journal of King Saud University-Engineering Sciences*, 2019.

[143] C. G. Wester. High impedance fault detection on distribution systems. In *1998 Rural Electric Power Conference Presented at 42nd Annual Conference*, pages c5–1, 1998.

[144] J Tengdin, R Westfall, et al. High impedance fault detection technology report of psrc working group d15, 1994.

[145] S Maximov, V Torres, HF Ruiz, and JL Guardado. Analytical model for high impedance fault analysis in transmission lines. *Mathematical Problems in Engineering*, 2014, 2014.

[146] D. P. S. Gomes, C. Ozansoy, and A. Ulhaq. High-sensitivity vegetation high-impedance fault detection based on signal's high-frequency contents. *IEEE Transactions on Power Delivery*, 33(3):1398–1407, 2018.

[147] A. P. Kujur and T. Biswal. Detection of high impedance fault in distribution system considering distributed generation. In *2017 International Conference on Innovative Mechanisms for Industry Applications (ICIMIA)*, pages 406–410, 2017.

[148] O.A. Gashteroodkhani, M. Majidi, M.S. Fadali, M. Etezadi-Amoli, and E. Maali-Amiri. A protection scheme for microgrids using time-time matrix z-score vector. *International Journal of Electrical Power & Energy Systems*, 110:400 – 410, 2019.

[149] Q. Cui, K. El-Arroudi, and Y. Weng. A feature selection method for high impedance fault detection. *IEEE Transactions on Power Delivery*, 34(3):1203–1215, 2019.

[150] S. Bhongade and S. Golhani. HIF detection using wavelet transform, travelling wave and support vector machine. In *2016 Int. Conf. on Electrical Power and Energy Systems (ICEPES)*, pages 151–156, 2016.

[151] K. Moloi, J. A. Jordaan, and Y. Hamam. High impedance fault detection technique based on discrete wavelet transform and support vector machine in power distribution networks. In *2017 IEEE AFRICON*, pages 9–14, 2017.

[152] H. Lala and S. Karmakar. Detection and experimental validation of high impedance arc fault in distribution system using empirical mode decomposition. *IEEE Systems Journal*, pages 1–12, 2020.

[153] K. V. Shihabudheen, B. Kunju, I. Ahammed, A. Guruvarurappan, J. Jose, D. Keerthana, and P. B. Revathi. Detection of high impedance fault using machine learning techniques. In *TENCON 2019 - 2019 IEEE Region 10 Conference (TENCON)*, pages 2117–2122, 2019.

[154] Ming-Ta Yang, Jhy-Cherng Gu, Jin-Lung Guan, and Chau-Yuan Cheng. Detection of high impedance faults in distribution system. In *2005 IEEE/PES Transmission Distribution Conference Exposition: Asia and Pacific*, pages 1–5, 2005.

[155] Amin Ghaderi, Herbert L Ginn III, and Hossein Ali Mohammadpour. High impedance fault detection: A review. *Electric Power Systems Research*, 143:376–388, 2017.

[156] Wellinsílvio Costa dos Santos, Benemar Alencar de Souza, Núbia Silva Dantas Brito, Flávio Bezerra Costa, and Marcelo Renato Cerqueira Paes. High impedance faults: From field tests to modeling. *Journal of Control, Automation and Electrical Systems*, 24(6):885–896, 2013.

[157] A. von Meier, E. Stewart, A. McEachern, M. Andersen, and L. Mehrmanesh. Precision micro-synchrophasors for distribution systems: A summary of applications. *IEEE Transactions on Smart Grid*, 8(6):2926–2936, 2017.

[158] Reynaldo F Nuqui and Arun G Phadke. Phasor measurement unit placement techniques for complete and incomplete observability. *IEEE Transactions on Power Delivery*, 20(4):2381–2388, 2005.

[159] Sergey Ioffe and Christian Szegedy. Batch normalization: Accelerating deep network training by reducing internal covariate shift. *arXiv preprint arXiv:1502.03167*, 2015.

[160] Diederik P Kingma and Jimmy Ba. Adam: A method for stochastic optimization. *arXiv preprint arXiv:1412.6980*, 2014.

[161] D. H. Boteler and R. J. Pirjola. Modelling geomagnetically induced currents produced by realistic and uniform electric fields. *IEEE Transactions on Power Delivery*, 13(4):1303–1308, Oct 1998.

[162] T. J. Overbye, T. R. Hutchins, K. Shetye, J. Weber, and S. Dahman. Integration of geomagnetic disturbance modeling into the power flow: A methodology for large-scale system studies. In *2012 North American Power Symposium (NAPS)*, pages 1–7, Sep. 2012.

[163] R. A. Walling. Potential impacts of harmonics on bulk system integrity during geomagnetic disturbances. In *2013 IEEE Power Energy Society General Meeting*, pages 1–5, July 2013.

[164] V. D. Albertson, J. M. Thorson, R. E. Clayton, and S. C. Tripathy. Solar-induced-currents in power systems: Cause and effects. *IEEE Transactions on Power Apparatus and Systems*, PAS-92(2):471–477, March 1973.

[165] Xuzhu Dong, Yilu Liu, and J. G. Kappenman. Comparative analysis of exciting current harmonics and reactive power consumption from gic saturated transformers. In *2001 IEEE Power Engineering Society Winter Meeting. Conference Proceedings (Cat. No.01CH37194)*, volume 1, pages 318–322 vol.1, Jan 2001.

[166] A. Pulkkinen, S. Lindahl, A. Viljanen, and R. Pirjola. Geomagnetic storm of 29–31 october 2003: Geomagnetically induced currents

and their relation to problems in the swedish high-voltage power transmission system. *Space Weather*, 3(8):1–19, Aug 2005.

[167] S. Guillon, P. Toner, L. Gibson, and D. Boteler. A colorful blackout: The havoc caused by auroral electrojet generated magnetic field variations in 1989. *IEEE Power and Energy Magazine*, 14(6):59–71, Nov 2016.

[168] John Kappenman. *Geomagnetic storms and their impacts on the US power grid*. Citeseer, 2010.

[169] R. P. Medeiros and F. B. Costa. A wavelet-based transformer differential protection with differential current transformer saturation and cross-country fault detection. *IEEE Transactions on Power Delivery*, 33(2):789–799, April 2018.

[170] A. H. Etemadi and A. Rezaei-Zare. Optimal placement of gic blocking devices for geomagnetic disturbance mitigation. *IEEE Transactions on Power Systems*, 29(6):2753–2762, Nov 2014.

[171] H. Zhu and T. J. Overbye. Blocking device placement for mitigating the effects of geomagnetically induced currents. *IEEE Transactions on Power Systems*, 30(4):2081–2089, July 2015.

[172] M. Kazerooni, H. Zhu, and T. J. Overbye. Mitigation of geomagnetically induced currents using corrective line switching. *IEEE Transactions on Power Systems*, 33(3):2563–2571, May 2018.

[173] P. Ripka, K. Draxler, and R. Styblikova. Measurement of dc currents in the power grid by current transformer. *IEEE Transactions on Magnetics*, 49(1):73–76, Jan 2013.

[174] Liu Lian-guang, Zhang Hao, Liu Chun-ming, Guo Jian-hui, and Guo Qing-xiong. Technology of detecting gic in power grids & its monitoring device. In *2005 IEEE/PES Transmission & Distribution Conference & Exposition: Asia and Pacific*, pages 1–5. IEEE, 2005.

[175] Cynthia Rudin, David Waltz, Roger N Anderson, Albert Boulanger, Ansaf Salleb-Aouissi, Maggie Chow, Haimonti Dutta, Philip N Gross, Bert Huang, Steve Ierome, et al. Machine learning for the new york city power grid. *IEEE transactions on pattern analysis and machine intelligence*, 34(2):328–345, 2012.

[176] Shu Fan, Luonan Chen, and Wei-Jen Lee. Machine learning based switching model for electricity load forecasting. *Energy Conversion and Management*, 49(6):1331–1344, 2008.

[177] North American Electric Reliability Corporation. Effects of geomagnetic disturbances on the bulk power system. 2012.

[178] Thomas Wiatowski, Philipp Grohs, and Helmut Bölcskei. Energy propagation in deep convolutional neural networks. *IEEE Transactions on Information Theory*, 64(7):4819–4842, 2017.

[179] Thomas Wiatowski and Helmut Bölcskei. A mathematical theory of deep convolutional neural networks for feature extraction. *IEEE Transactions on Information Theory*, 64(3):1845–1866, 2017.

[180] Edouard Oyallon, Eugene Belilovsky, and Sergey Zagoruyko. Scaling the scattering transform: Deep hybrid networks. In *Proceedings of the IEEE international conference on computer vision*, pages 5618–5627, 2017.

[181] G Ososkov and A Shitov. Gaussian wavelet features and their applications for analysis of discretized signals. *Computer physics communications*, 126(1-2):149–157, 2000.

[182] Payman Dehghanian and Mladen Kezunovic. Probabilistic decision making for the bulk power system optimal topology control. *IEEE Transactions on Smart Grid*, 7(4):2071–2081, 2016.

[183] Payman Dehghanian, Yaping Wang, Gurunath Gurrala, Erick Moreno-Centeno, and Payman Kezunovic. Flexible implementation of power system corrective topology control. *Electric Power System Research*, 128:79–89, 2015.

[184] Mohannad Alhazmi, Payman Dehghanian, Shiyuan Wang, and Bhavesh Shinde. Power grid optimal topology control considering correlations of system uncertainties. In *IEEE/IAS 55th Industrial and Commercial Power Systems (I&CPS) Technical Conference*, pages 1–7, 2019.

[185] Mladen Kezunovic, Tomo Popovic, Gurunath Gurrala, Payman Dehghanian, Ahad Esmaeilian, and Mohammad Tasdighi. Reliable implementation of robust adaptive topology control. In *The 47th Hawaii International Conference on System Science (HICSS)*, pages 1–10, 2014.

[186] Payman Dehghanian and Mladen Kezunovic. Impact assessment of power system topology control on system reliability. In *IEEE Conference on Intelligent Systems Applications to Power Systems (ISAP)*, pages 1–6, 2015.

[187] Payman Dehghanian and Mladen Kezunovic. Probabilistic impact of transmission line switching on power system operating states. In *IEEE Power and Energy Society (PES) Transmission and Distribution (T&D) Conference and Exposition*, pages 1–6, 2016.

[188] Mohannad Alhazmi, Payman Dehghanian, Shiyuan Wang, and Bhavesh Shinde. Power grid optimal topology control considering correlations of system uncertainties. *IEEE Transactions on Industry Applications*, 55(6):5594–5604, November/December 2019.

[189] Mostafa Nazemi, Payman Dehghanian, and Miguel Lejeune. A mixed-integer distributionally robust chance-constrained model for optimal topology control in power grids with uncertain renewables. In *13th IEEE Power and Energy Society (PES) PowerTech Conference*, pages 1–6, 2019.

[190] PSCAD IEEE 30 Bus System, Manitoba.HVDC Reserach Center, May 2018.

[191] Bei Zhang, Payman Dehghanian, and Mladen Kezunovic. Simulation of weather impacts on the wholesale electricity market. In *10th International Conference on Deregulated Electricity Market Issues in South Eastern Europe (DEMSEE)*, pages 1–6, 2015.

[192] T Dokic, Payman Dehghanian, P-C Chen, Mladen Kezunovic, Z Medina-Cetina, J Stojanovic, and Z Obradovic. Risk assessment of a transmission line insulation breakdown due to lightning and severe weather. In *The 49th Hawaii International Conference on System Science (HICSS)*, pages 1–8, 2016.

[193] Bei Zhang, Payman Dehghanian, and Mladen Kezunovic. Spatial-temporal solar power forecast through gaussian conditional random fields. In *IEEE Power and Energy Society (PES) General Meeting*, pages 1–5, 2016.

[194] Farzaneh Pourahmadi and Payman Dehghanian. A game-theoretic loss allocation approach in power distribution systems with high penetration of distributed generations. *Mathematics*, 6(9):1–14, 2018.

[195] Farzaneh Pourahmadi, S. H. Hosseini, Payman Dehghanian, Ekundayo Shittu, and Mahmud Fotuhi-Firuzabad. Uncertainty cost of stochastic producers: Metrics and impacts on power grid operational flexibility. *IEEE Transactions on Engineering Management*, pages 1–12, 2020.

[196] M Zareian Jahromi, Mohsen Tajdinian, J Zhao, Payman Dehghanian, M Allahbakhshi, and AR Seifi. An enhanced sensitivity-based decentralized framework for real-time transient stability assessment in bulk power grids with renewable energy resources. *IET Generation, Transmission, and Distribution Systems*, 14(4):665–674, February 2020.

[197] Moein Moeini-Aghtaie, Payman Dehghanian, Mahmud Fotuhi-Firuzabad, and Ali Abbaspour. Multi-agent genetic algorithm: An online probabilistic view on economic dispatch of energy hubs constrained by wind availability. *IEEE Transactions on Sustainable Energy*, 5(2):699–708, 2014.

[198] Payman Dehghanian, Seyed Hamid Hosseini, Moein Moeini-Aghtaie, and Saman Arabali. Optimal siting of dg units in power systems from a probabilistic multi-objective optimization perspective. *International Journal of Electrical Power and Energy Systems*, 51:14–26, 2013.

[199] Farzaneh Pourahmadi, Hooman Heidarabadi, Seyed Hamid Hosseini, and Payman Dehghanian. Dynamic uncertainty set characterization for bulk power grid flexibility assessment. *IEEE Systems Journal*, 14(1):718–728, March 2020.

[200] R Azizpanah-Abarghooee, Payman Dehghanian, and V Terzija. A practical multi-area bi-objective environmental economic dispatch equipped with a hybrid gradient search method and improved jaya algorithm. *IET Generation, Transmission & Distribution*, 10(14):3580–3596, 2016.

[201] Miguel Lejeune and Payman Dehghanian. Optimal power flow models with probabilistic guarantees: A boolean approach. *IEEE Transactions on Power Systems*, pages 1–4, July 2020.

[202] Fei Wang, B Xiang, K Li, X Ge, H Lu, J Lai, and Payman Dehghanian. Smart households' aggregated capacity forecasting for load aggregators under incentive-based demand response programs. *IEEE Transactions on Industry Applications*, 56(2):1086–1097, March/April 2020.

[203] Jingang Lai, Xiaoqing Lu, Fei Wang, Payman Dehghanian, and Ruoli Tang. Broadcast gossip algorithms for distributed peer-to-peer control in AC microgrids. *IEEE Transactions on Industry Applications*, 55(3):2241–2251, May/June 2019.

[204] Fei Wang, B Xiang, K Li, J Lai, and Payman Dehghanian. Day-ahead forecast of aggregated loads for smart households under incentive-based demand response programs. In *IEEE Industry Applications Society (IAS) Annual Meeting*, pages 1–10, 2019.

[205] S Dehghan-Dehnavi, Mahmud Fotuhi-Firuzabad, Moein Moeini-Aghtaie, Payman Dehghanian, and Fei Wang. Estimating participation abilities of industrial customers in demand response programs: A two-level decision-making tree analysis. In *IEEE/IAS 56th Industrial and Commercial Power Systems (I&CPS) Technical Conference*, pages 1–7, 2020.

[206] Mohammad Khoshjahan, Payman Dehghanian, Moein Moeini-Aghtaie, and Mahmud Fotuhi-Firuzabad. Harnessing ramp capability of spinning reserve services for enhanced power system flexibility. *IEEE Transactions on Industry Applications*, 55(6):7103–7112, November/December 2019.

[207] M Zareian Jahromi, Mohsen Tajdinian, J Zhao, Payman Dehghanian, M Allahbakhshi, and AR Seifi. An enhanced sensitivity-based decentralized framework for real-time transient stability assessment in bulk power grids with renewable energy resources. *IET Generation, Transmission, and Distribution Systems*, 14(4):665–674, February 2020.

[208] M Tajdinian, M Allahbakhshi, A. R. Bagheri, H Samet, Payman Dehghanian, and O. P. Malik. An enhanced sub-cycle statistical algorithm for inrush and fault currents classification in differential protection schemes. *International Journal of Electrical Power and Energy Systems*, 119:1–17, July 2020.

[209] Z Li, K Li, Fei Wang, Z Mi, and Payman Dehghanian. An auto-encoder neural network approach to monthly electricity consumption forecasting using hourly data. In *IEEE/IAS 56th Industrial and Commercial Power Systems (I&CPS) Technical Conference*, pages 1–7, 2020.

[210] Z Li, Z Xuan, K Li, Fei Wang, Z Mi, Payman Dehghanian, W Li, and Mahmud Fotuhi-Firuzabad. Monthly electricity consumption forecasting based on two-stage forecasting step reduction strategy and auto-encoder neural network. *IEEE Transactions on Industry Applications*, pages 1–11, 2020.

[211] Mohammad Khoshjahan, Moein Moeini-Aghtaie, Mahmud Fotuhi-Firuzabad, Payman Dehghanian, and Hesam Mazaheri. Advanced bidding strategy for participation of energy storage systems in joint energy and flexible ramping product market. *IET Generation, Transmission, and Distribution*, pages 1–11, 2020.

[212] M. A. Saffari, M. S. Misaghian, M. Kia, A. Heidari, D. Zhang, Payman Dehghanian, and Jamshid Aghaei. Stochastic robust optimization for smart grid considering various arbitrage opportunities. *Electric Power Systems Research*, 174:1–14, September 2019.

[213] Moein Moeini-Aghtaie, Ali Abbaspour, Mahmud Fotuhi-Firuzabad, and Payman Dehghanian. Optimized probabilistic phev demand management in the context of energy hubs. *IEEE Transactions on Power Delivery*, 30(2):996–1006, 2015.

[214] Moein Moeini-Aghtaie, Ali Abbaspour, Mahmud Fotuhi-Firuzabad, and Payman Dehghanian. Phev's centralized/decentralized charging

control mechanisms: Requirements and impacts. In *The 45th North American Power Symposium (NAPS)*, pages 1–6, 2013.

[215] Mohammad Saeed Misaghian, Mohammadali Saffari, Mohsen Kia, Alireza Heidari, Payman Dehghanian, and Bo Wang. Electric vehicles contributions to voltage improvement and loss reduction in microgrids. In *North American Power Symposium (NAPS)*, pages 1–6, 2018.

[216] Bo Wang, Payman Dehghanian, Shiyuan Wang, and Massimo Mitolo. Electrical safety considerations in large electric vehicle charging stations. *IEEE Transactions on Industry Applications*, 55(6):6603–6612, November/December 2019.

[217] Bo Wang, Payman Dehghanian, and Dongbo Zhao. Chance-constrained energy management system for power grids with high proliferation of renewables and electric vehicles. *IEEE Transactions on Smart Grid*, 11(3):2324–2336, May 2020.

[218] Bo Wang, Dongbo Zhao, Payman Dehghanian, Y Tian, and T Hong. Aggregated electric vehicle load modeling in large-scale electric power systems. *IEEE Transactions on Industry Applications*, pages 1–14, 2020.

[219] Bo Wang, Payman Dehghanian, Dan Hu, and Shiyuan Wang. Adaptive operation strategies for electric vehicle charging stations. In *IEEE Industry Applications Society (IAS) Annual Meeting*, pages 1–7, 2019.

[220] Bo Wang, J. A. Camacho, G. M. Pulliam, A. H. Etemadi, and Payman Dehghanian. New reward and penalty scheme for electric distribution utilities employing load-based reliability indices. *IET Generation, Transmission & Distribution*, 12(15):3647–3654, 2018.

Appendix A: Appendix

A.1 Derivations of the Gaussian Wavelet Transform

Using the definition presented in (5.3)

$$\int_{-\infty}^{\infty} g_1(x)dx = -g_0(x), \quad \int_{-\infty}^{\infty} g_n(x)dx = -g_{n-1}(x) \tag{A.1}$$

$$\int_{-\infty}^{\infty} g_n(\tfrac{t-b}{a})d(\tfrac{t-b}{a}) = \frac{1}{a}\int_{-\infty}^{\infty} g_n(\tfrac{t-b}{a})dt = -g_{n-1}(\tfrac{t-b}{a}) \tag{A.2}$$

The first and second step partial integration of (5.4) is

$$\begin{aligned} X_g(w|a,b)\cdot\sqrt{C_{g_n}} &= -\left[ax(t)g_{n-1}(\tfrac{t-b}{a})\right]_{-\infty}^{+\infty} + \int_{-\infty}^{\infty}\tfrac{d}{dt}x(t)ag_{n-1}(\tfrac{t-b}{a})dt \\ &= -\left[ax(t)g_{n-1}(\tfrac{t-b}{a})\right]_{-\infty}^{+\infty} - \left[a^2\tfrac{d}{dt}x(t)g_{n-2}(\tfrac{t-b}{a})\right]_{-\infty}^{+\infty} \\ &+ \int_{-\infty}^{\infty} a^3\tfrac{d^2}{dt^2}x(t)g_{n-3}(\tfrac{t-b}{a})dt \\ &= \ldots \\ &= \sum_{n=0}^{N-1}\left[(-a^n\tfrac{d^n}{dt^n}x(t)\tfrac{d^{(N-n)}}{dt^{(N-n)}}g_0(\tfrac{t-b}{a})\right]_{-\infty}^{+\infty} \\ &+ \int_{-\infty}^{\infty} a^N\tfrac{d^N}{dt^N}x(t)g_0(\tfrac{t-b}{a})dt. \end{aligned} \tag{A.3}$$

By continuously applying the partial integration, (5.6) can be obtained. We know $g_n(\pm\infty) = 0$ and $\frac{d^n}{dt^n}x(t)$ is finite for any value of n; therefore, the summation in the first part in (5.6) would be zero.

A.2 Derivations of the Morlet Wavelet Transform

$$
\begin{aligned}
X_m(w|a,b) &= \int_{-\infty}^{\infty} x(t) \frac{1}{\sqrt{\pi F_B}} \cos\left(\omega_c(\tfrac{t-b}{a})\right) e^{-\frac{(t-b)^2}{a^2 F_B}} dt \\
&= \int_{-\infty}^{\infty} A_h \cos(\omega_h t + \theta_h) \frac{1}{\sqrt{\pi F_B}} \cos\left(\omega_c(\tfrac{t-b}{a})\right) e^{-\frac{(t-b)^2}{a^2 F_B}} dt
\end{aligned}
\tag{A.4}
$$

where $x = (t-b)/a$, F_B is a constant value representing the decay factor, and ω_c is the center frequency. Using the Euler's equation and (5.8), we can obtain

$$
\begin{aligned}
X_m(w|a,b) &= \frac{aA_h}{\sqrt{\pi F_B}} \int_{-\infty}^{\infty} \cos(a\omega_h x - \omega_h b + \theta_h) \cos(\omega_c x) e^{-\frac{x^2}{F_B}} dx \\
&= \frac{aA_h}{2} \cos(a\omega_h + \theta_h)(e^{-\frac{F_B}{4}(a\omega_h+\omega_c)^2} + e^{-\frac{F_B}{4}(a\omega_h-\omega_c)^2})
\end{aligned}
\tag{A.5}
$$